

Two Ions Coupled to an Optical Cavity:
from an Enhanced Quantum Computer Interface
towards Distributed Quantum Computing

Dissertation

zu Erlangung des Doktorgrades an der
Fakultät für Mathematik, Informatik und Physik
der Leopold-Franzens-Universität Innsbruck

vorgelegt von

Lic. Bernardo Casabone

durchgeführt am Institut für Experimentalphysik
unter der Leitung von

Univ.-Prof. Dr. Rainer Blatt

Innsbruck, April 2015

Zusammenfassung

Verteiltes Quantenrechnen stellt eine Möglichkeit zur Verbesserung der Rechenleistung von Quantencomputern dar, erfordert jedoch Verschränkung zwischen den einzelnen Bestandteilen des Quantennetzwerks. In unserer Forschungsgruppe wurden zwei Alternativen der Verknüpfung ionenbasierter Quantencomputer mit Hilfe von optischen Resonatoren demonstriert: Verschränkung von einem Ion mit einem Photon und die Abbildung des Quantenzustands eines Ions auf den eines einzelnen Photons.

In dieser Arbeit erweitern wir einerseits die erste Methode und verschränken zwei Ionen, die sich innerhalb desselben optischen Resonators befinden. Die Verschränkung wird effizient erzeugt und ist angekündigt. Außerdem müssen die beiden Ionen sich nicht im selben Resonator befinden, sodass unser Ergebnis einen Baustein für die effiziente Erzeugung von Verschränkung entfernter ionenbasierter Quantencomputer darstellt.

Im zweiten Teil der Arbeit wird diskutiert, wie kollektive Effekte verwendet werden können, um die Leistung einer resonatorbasierten Quantenschnittstelle zu verbessern. Wir zeigen, dass bei der Verwendung eines sogenannten superradianten Zustands die Kopplungsstärke zwischen den beiden Ionen und dem Resonator im Vergleich mit einem einzelnen Ion effektiv gesteigert wird. Komplementär dazu wird gezeigt, dass ein Zustand der zwei Ionen erzeugt werden kann, der eine stark reduzierte Kopplungsstärke an den Resonator aufweist, das ist, ein subradianter Zustand. Abschließend wird die gesteigerte Kopplungsstärke des superradianten Zustands verwendet, um eine verbesserte Version des Protokolls zur Zustandsabbildung zu demonstrieren.

Aus dem verwendeten experimentellen Aufbau und einem zweiten Aufbau, der sich in der Konstruktionsphase befindet, wird in naher Zukunft ein Quantennetzwerk aufgebaut werden. Das in der vorliegenden Arbeit beschriebene Protokoll zur Verschränkung zweier Ionen wird verwendet werden, um Ionen in den zwei räumlich getrennten Aufbauten zu verschränken. In diesem Experiment müssen die Photonen, die von den Ionen erzeugt werden ununterscheidbar sein. Diese Voraussetzung kann erfüllt werden, indem die Form der photonischen Wellenpakete mit Hilfe kollektiver Effekte kontrolliert wird.

Abstract

Distributed quantum computing, an approach to scale up the computational power of quantum computers, requires entanglement between nodes of a quantum network. In our research group, two building blocks of schemes to entangle two ion-based quantum computers using cavity-based quantum interfaces have recently been demonstrated: ion-photon entanglement and ion-photon state mapping.

In this thesis work, we extend the first building block in order to entangle two ions located in the same optical cavity. The entanglement generated by this protocol is efficient and heralded, and as it does not rely on the fact that ions interact with the same cavity, our results are a stepping stone towards the efficient generation of entanglement of remote ion-based quantum computers.

In the second part of this thesis, we discuss how collective effects can be used to improve the performance of a cavity-based quantum interface. We show that by using two ions in the so-called superradiant state, the coupling strength between the two ions and the optical cavity is effectively increased compared to the single-ion case. As a complementary result, the creation of a state of two ions that exhibits a reduced coupling strength to the optical cavity, i.e., a subradiant state, is shown. Finally, we demonstrate a direct application of the increased coupling strength that the superradiant state exhibits by showing an enhanced version of the ion-photon state mapping process.

By using the current setup and a second one that is being assembled, we intend to build a quantum network. The heralded ion-ion entanglement protocol presented in this thesis work will be used to entangle ions located in both setups, an experiment that requires photons generated in both apparatuses to be indistinguishable. Collective effects then can be used to modify the waveform of photons exiting the cavity in order to effect the desired photon indistinguishability.

Contents

1	Introduction	1
2	A $^{40}\text{Ca}^+$ ion coupled to a high-finesse optical cavity	5
2.1	The $^{40}\text{Ca}^+$ ion as a qubit	5
2.2	The optical cavity as an interface between $^{40}\text{Ca}^+$ ions and photons	7
3	Cavity-mediated Raman transitions	11
3.1	Three-level system coupled to a single-mode cavity	11
3.2	Twelve-level system coupled to two cavity modes	15
4	The experimental setup	21
4.1	Ion trap	21
4.2	The optical cavity	23
4.3	Laser system	25
4.3.1	The improved 729 nm optical path	26
4.3.2	The addressing 729 nm beam	29
4.4	Detection and analysis of the polarization state of cavity photons	31
4.5	Further improvements	33
5	A toolbox for quantum computing	37
5.1	Doppler-Cooling and state reinitialization	37
5.2	State manipulation	38
5.2.1	Preparing the state of the ions	39
5.3	Sideband cooling	39
5.4	Ions' state detection using a PMT	41
5.5	Ions' state detection using a CCD camera	47
5.6	Comparing the CCD and the PMT ions' state detection methods	50
5.7	Testing the alignment of addressing and global 729 nm beams	51
5.8	Mølmer-Sørensen gate	52
5.9	AC-Stark shift gate	56
6	Tunable coupling of two ions to an optical cavity	59
6.1	Setting and probing the coupling	59
6.2	Results	62
6.3	Experimental considerations	62
6.4	Conclusions	64

7	Entanglement of two ions in an optical cavity	67
7.1	Introduction	67
7.2	Description of the protocol	68
7.3	State fidelity via parity flops	69
7.4	Implementation of the protocol and results	70
7.5	Experimental considerations of the protocol	74
7.6	Conclusions	76
8	Sub- and superradiance with two ions and an optical cavity	77
8.1	Introduction	77
8.1.1	Two emitters in free space	78
8.1.2	Two emitters in an optical cavity	79
8.2	Description of the experiment	82
8.2.1	Expected variation of the temporal shape of generated photon in our setup	84
8.3	Results	84
8.4	Two-ion crystal as a single photon source	88
8.5	Conclusions	89
9	Enhanced ion-photon state mapping	91
9.1	Introduction	91
9.2	Ion-crystal transducer using the Fock state basis	92
9.3	Ion-crystal transducer using the polarization state basis	93
9.4	Implementation of the ion-crystal transducer in our setup	94
9.5	Result of the implementation of the ion-crystal transducer	96
9.6	Towards the enhanced reading process of a quantum memory	101
9.7	Conclusions	103
10	Summary and Outlook	105

1 Introduction

Scalability is a requirement for the successful implementation of a universal quantum computer, that is, there must be a feasible route to increase the computing power of the device so that it can solve classically intractable problems [1]. A universal quantum computer, however, does not need to be a single, scalable device. A possible approach to scalability is so-called distributed quantum computing [2–4], in which the idea is to interconnect many small and well-controlled quantum computers. There, information, which is transported by quantum information carriers, is exchanged between quantum computers through quantum channels. In this context, a quantum interface mediates the interaction between each quantum computer and the carrier of quantum information.

Many physical implementations of quantum computers have been proposed and studied, and some of them have been implemented as proofs of principle. The most promising of these implementations are based on ultracold quantum gases [5, 6], trapped ions [7–9], superconducting qubits [10] and photons [11].

In order to transmit the quantum information, photons and optical fibers are ideal candidates as quantum information carriers and quantum channels: photons can be guided from one quantum computer to another using optical fibers; additionally, photons interact weakly with the channel, thus minimizing losses of quantum information due to decoherence.

For the implementation of a quantum interface between the quantum computers and the quantum information carriers, that is, the emitters and the photons, two different approaches can be identified: the probabilistic and the deterministic approach. In the probabilistic approach, high numerical aperture lenses with collection efficiencies typically in the order $1 - 10\%$ are used to collect and direct photons to and from the emitters [12–14]. In the second case, the deterministic approach makes use of optical cavities which enhance the interaction between the emitter and the photons [15]. Such a scheme is called deterministic as an emitter in a cavity can absorb and emit a photon with an efficiency that can be increased up to one [16, 17].

In order to interconnect quantum computers, schemes using one [2, 18] and two photons [19, 20] have been proposed. Here, we focus on two of these schemes. In the first one, the information from one emitter is directly transferred to the remote emitter [2]. This protocol has been already used to generate remote entanglement between two atoms, each of which is located inside one optical cavity [21]. In the second scheme, two photons are generated, each of which is entangled with one emitter. Interference and subsequent detection of these photons leads to entanglement between the emitters. This protocol has already been used to generate entanglement between two remote ions [14, 22, 23], two remote atoms [24], an atom and a Bose-Einstein condensate [25] and two remote ensembles of atoms [26, 27].

The work presented in this thesis has been performed in the research group of Prof. Rainer Blatt, in the Institut für Experimentalphysik, at the University of Innsbruck. The group has been working on the topic of quantum computing using ions for the last 20 years. Ion-based systems have proved to be ideal candidates for a quantum computers as a high-fidelity toolbox for the initialization, manipulation and readout of a qubit defined in the electronic states of the ions has been already developed [28].

As a doctoral student in the group, Dr. Carlos Russo built a deterministic, cavity-based interface for an ion-based quantum computer [29]. This interface has recently been used to demonstrate the building blocks for the generation of remote entanglement following the two schemes introduced previously. These building blocks are ion-photon entanglement [30] and ion-photon state mapping [31]; in the first case, an ion was entangled with a single photon, while in the second, information encoded in an ion was mapped onto a photon.

In the first part of this thesis, ion-photon entanglement [30] is extended to generate heralded entanglement of two ions in an optical cavity. Entanglement of two Rydberg atoms inside an optical cavity has been reported in the pioneering experiment by Prof. Serge Haroche and colleagues [32, 33]. The entanglement reported in Refs. [32, 33], however, is based on the unitary evolution of the atom–cavity interaction. In our experiment, the detection of two indistinguishable photons, which are entangled with the ions, leads to generation of ion-ion entanglement. As the protocol does not rely on the fact that the ions are located in the same trap or are interacting with the same cavity, this result represents a stepping stone towards the generation of entanglement of remote ions, each interacting with its own cavity.

One key aspect of a cavity-based quantum interface is the strength of the coupling between the ion and the mode of the cavity. The ion-photon state-mapping process is studied in Ref. [31], in which it is shown that the efficiency of the process cannot be increased without affecting the fidelity, and vice versa. This apparent balance between fidelity and efficiency originates from the sensitivity of the protocol to the strength of the coupling. If higher efficiencies and fidelities are required, the natural approach would be the use of a better optical cavity, i.e., a cavity that offers a stronger coupling. This approach is technologically demanding, as it requires cavities that have a small mode volume [34]. An approach that relaxes this technological requirement is the use of a crystal of ions in a so-called superradiant state as a resource.

A superradiant state is a particular state of matter that exhibits an enhanced coupling strength to a given mode of an electromagnetic field. In an ion-cavity system, the coupling rate between the cavity and N ions in the first state of the superradiant cascade described by Dicke [35] is increased to $g\sqrt{N}$, where g is the single-ion coupling rate [36]. As the coupling is effectively increased, the performance of a quantum interface that uses a superradiant state as a resource is expected to be enhanced.

The second part of this thesis is focused on the investigation of subradiance and superradiance and its direct application to enhance the performance of a cavity-based quantum interface.

Superradiance has been the focus of several works using large ensembles of particles, and effects such as changes in radiation rates [37], a phase transition [38, 39] and narrow-linewidth lasing [40] have been observed. Both subradiance and superradiance of two emitters have been observed using two trapped ions in free space [41]. In this thesis work, we create subradiant and superradiant states of two ions in an optical cavity. Then, we encode quantum information in the two-ion superradiant state and transfer the information onto a single photon. By comparing the efficiency and fidelity of such a process with the efficiency and fidelity of single-ion state transfer, we demonstrate that the performance of the cavity-based quantum interface is enhanced.

This dissertation is structured as follows: In Chapter 2, we introduce the $^{40}\text{Ca}^+$ ion as a resource to store and manipulate quantum information. We also discuss the parameter regime for a successful implementation of a cavity-based quantum interface, as well as possible coupling schemes between the cavity and the ions. In Chapter 3, we introduce Raman transitions, a concept that is relevant for understanding the experiments presented later. In Chapter 4, the experimental apparatus is described. In Chapter 5, we summarize the “quantum optics toolbox” used to work with the $^{40}\text{Ca}^+$ ion. In Chapter 6, we describe the technique that allows us to control the individual coupling of two ions to the optical cavity. In Chapter 7, we show our results regarding the entanglement of two ions mediated by the optical cavity. In Chapter 8, we show the creation of sub- and superradiant states of two ions in the optical cavity. In Chapter 9, we demonstrate that the superradiant state enhances the fidelity and efficiency of a process that transfers information onto a single photon. Finally, Chapter 10 summarizes the results presented in this thesis and provides an outlook to future experiments.

2 A $^{40}\text{Ca}^+$ ion coupled to a high-finesse optical cavity

In this chapter, we first introduce the heart of the research of our research group, the $^{40}\text{Ca}^+$ ion. We discuss how the $^{40}\text{Ca}^+$ ions can be used as quantum bits: we introduce the basic techniques for loading and cooling the ions, and for manipulating and reading out their electronic and motional state. A further description of these techniques, which have been developed in the course of the last decade, can be found in Ref. [28].

Next, we introduce the cavity-based quantum interface between ions and photons constructed in the group. The interface was assembled by Carlos Russo in 2006 [29] and has been serving as a basis for the novel research toward quantum networking that has been carried out since then [17, 30, 31, 42–46]. We discuss the parameter regime for a successful implementation of a coherent interface and possible ion–cavity coupling schemes. Finally, we introduce the cavity-mediated Raman transition, which allows us to reach the regime of parameters for a coherent interface. Raman transitions are then discussed in detail in Chapter 3.

2.1 The $^{40}\text{Ca}^+$ ion as a qubit

For the experiments presented in this thesis, we have used $^{40}\text{Ca}^+$ ions. These atoms offer their most relevant transitions at wavelengths in the visible spectrum, and there, laser radiation sources are commercially available at relative low cost. Additionally, the relatively large atomic mass leads to large Lamb-Dicke factors (Section 5.8), facilitating the coupling between the electronic and motional degrees of freedom. These advantages, plus the fact that $^{40}\text{Ca}^+$ ions provide ground and long-lived excited states to store quantum information, make $^{40}\text{Ca}^+$ ions promising candidates with which to process quantum information [28, 47, 48].

The relevant electronic levels of the $^{40}\text{Ca}^+$ ion are shown in Fig. 1. The system comprises one ground-state manifold $4^2S_{1/2}$, two short-lived excited-state manifolds $4^2P_{1/2}$ and $4^2P_{3/2}$ and two metastable-state manifolds $3^2D_{3/2}$ and $3^2D_{5/2}$.

In order to confine $^{40}\text{Ca}^+$ ions, we heat neutral calcium atoms using an oven, and direct the flying atoms towards the trap. The atoms are ionized via a two-photon process [49] and then confined by the pseudopotential generated by the linear Paul trap (Section 4.1 and Ref. [50]). After the ions are trapped, they are cooled using the Doppler effect employing a red-detuned laser on the $4^2S_{1/2} \leftrightarrow 4^2P_{1/2}$ transition, together with a repump field (Section 5.1 and Refs. [51, 52]). Once ions are cooled to temperatures near the Doppler limit, their motion can be further cooled to the ground state by means of sideband cooling techniques (Section 5.3 and Refs. [53]).

In order to use $^{40}\text{Ca}^+$ ions for the purpose of quantum information, one needs to identify two suitable levels in which to store and manipulate the single unit of quantum information, a qubit. Currently, two different schemes are used to store quantum information in trapped ions and in $^{40}\text{Ca}^+$ in particular; the optical and the radiofrequency qubits. In the first scheme, a state from the ground-state manifold $4^2S_{1/2}$ and one from the metastable-state manifolds $3^2D_{3/2}$ or $3^2D_{5/2}$

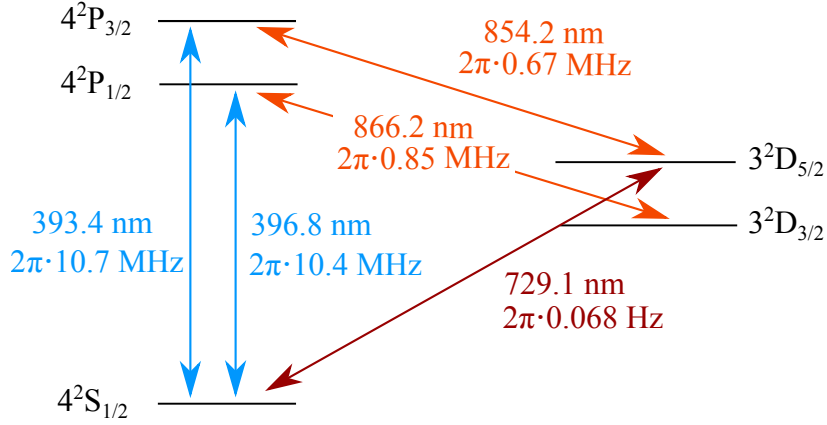


Figure 1: Relevant electronic levels of $^{40}\text{Ca}^+$ ion. Wavelength and half-linewidths, which represent the decay rates, of the transitions are taken from [55–57]. The system comprises one ground-state manifold $4^2S_{1/2}$, two short-lived excited-state manifolds $4^2P_{1/2}$ and $4^2P_{3/2}$ and two metastable-state manifolds $3^2D_{3/2}$ and $3^2D_{5/2}$.

provide the two-level system. In the second scheme, two Zeeman sublevels of the ground-state manifold $4^2S_{1/2}$ provide the two-level system [54].

In Ref. [28], the different aspects of the optical and radiofrequency qubits are studied in detail. In summary, the radiofrequency qubit has the advantage that it can be manipulated by microwave fields, whereas the optical qubit requires laser light. For this purpose, the generation of microwaves is less technologically demanding than the generation of optical frequencies, especially considering that the manipulation of the optical qubit requires a laser linewidth on the order of one hertz. Radio frequencies, however, offer small Lamb-Dicke factors compared to optical frequencies, and therefore a weaker coupling between the electronic and the motional degree of freedom of the ions. Such a coupling is however required for the implementation of key quantum information protocols, such as the CNOT gate [58, 59] or the Mølmer–Sørensen gate [60, 61].

In order to perform the experiments presented in this thesis, we use the optical qubit. In particular, superpositions between a state from the $4^2S_{1/2}$ manifold and one state from the $3^2D_{5/2}$ manifold are used to store quantum information. Multi- and single-qubit operations are implemented with an ultra-stable 729 nm laser which is available in our laboratory (Ref. [62] and Section 4.3.1). When the laser field is applied at the atomic transition frequency, the ions' state populations oscillate at a rate given by the Rabi frequency (Section 5.2). Controlling the phase and duration of the light pulse allows us to implement arbitrary single-qubit rotations in the state space defined by the Bloch sphere. Mølmer–Sørensen gate operations are performed by bichromatic 729 nm laser light pulses (Section 5.8).

To read out the state of the ions, that is, to determine whether the $4^2S_{1/2}$ manifold or the $4^2P_{3/2}$ manifold is populated, the electron shelving technique is used [28, 53, 63]. During a detection interval, a laser at 397 nm illuminates the ions, exciting the $4^2S_{1/2} \leftrightarrow 4^2P_{1/2}$ transition.

A laser at 866 nm repumps ions that decay to the $3^2D_{3/2}$ manifold. If the $4^2S_{1/2}$ manifold is populated, the ions scatter photons at 397 nm which are detected with a photomultiplier tube (PMT) or imaged on a charge-coupled device (CCD camera). If the state $3^2D_{5/2}$ is populated, the laser at 397 nm does not couple the ions' electronic state and therefore photons are not generated. Detection with the PMT allows us to extract how many ions are in the state $4^2S_{1/2}$ and state $3^2D_{5/2}$ (see Section 5.4), whereas detection with the CCD camera allows us to detect the individual state of each ion (see Section 5.5).

2.2 The optical cavity as an interface between $^{40}\text{Ca}^+$ ions and photons

In the previous section, we have introduced the $^{40}\text{Ca}^+$ ion as medium in which to store and manipulate quantum information. In order to set up or build a network comprising more than one ion-based quantum computer, the quantum computers should share information. Due to their weak interaction with free-space or fiber-based optical channels, photons are ideal candidates to carry information between ions located in different traps. In the photons, the information can be encoded in several ways, for example, the polarization degree of freedom, in a time-bin basis, or using the photon-number state [64].

As discussed in Chapter 1, the probabilistic ion-photon interface makes use of high-numerical aperture lenses to collect and direct photons to and from ions [12]. Here, we use an approach, which is in principle deterministic, in which an optical cavity is used as a coherent interface between ions and photons.

Consider a two-level atom interacting with a cavity, the frequency of which is resonant with the energy difference between the two atomic levels. The dynamics of the system are governed by the coupling strength g between the atom and the cavity, and by the dissipative coupling rate γ and κ , that is, the respective decay rates of the atom and the cavity field to the environment. In order to use the cavity as a coherent interface between the ion and a photon, a system that satisfies $\kappa \gg g^2/\kappa \gg \gamma$ is sufficient [65]. In this regime—the so-called “one-dimensional atom” in the bad cavity limit [66]—the cavity decay κ sets the fastest rate, while g^2/κ dominates over the dissipative coupling γ . The first part of the inequality implies that a cavity photon leaves the cavity before it is reabsorbed by the atom, while the second part implies that a photon is generated by the atom before the atom dissipates the energy to the environment.

We note that a system that satisfies $g \gg \{\kappa, \gamma\}$ —the so-called strong coupling regime—is beyond the requirements for a coherent interface. During a coherent process for the generation of a single photon in such an interface, the photon will be reabsorbed and reemitted by the atom several times before it leaves the cavity. The strong coupling regime, however, would allow the investigation of novel effects in an ion-cavity system, such as the vacuum Rabi splitting [67], photon blockade [68], gates between photons and ions [69, 70] or cavity cooling [71].

In the experiments presented in this thesis, a qubit is encoded in a superposition between one state from the $4^2S_{1/2}$ manifold and one state from the $3^2D_{5/2}$ manifold. In order to transfer

the qubit state onto a photon state, the cavity can be built such that it is resonant with the energy difference between the $4^2S_{1/2}$ and $3^2D_{5/2}$ states. Such a configuration is discussed in Ref. [72] and was realized more than a decade ago in our research group [73, 74]. The coupling rate g of the cavity to a specific transition depends on the overlap between the moment of the transition and the moment of the cavity field. The quadrupole moment of the field inside the optical cavity is relatively small compared to the dipole moment; therefore, the coupling to the quadrupole $4^2S_{1/2} \leftrightarrow 3^2D_{5/2}$ transition is expected to be weak. For example, for the parameters of the setup presented in Ref. [72], the coupling is calculated to be $g \approx 2\pi \cdot 100$ Hz. The value is relatively high compared to the slow decay $\gamma \approx 2\pi \cdot 0.068$ Hz, but it is small compared to the cavity's fast decay $\kappa \approx 20$ kHz. For such a setup, the coupling of the cavity to the ion has been measured to be $g \approx 2\pi \cdot 134$ Hz in Ref. [73] and $g \approx 2\pi \cdot 120$ Hz in Ref. [75].

Although the parameters of this system fulfill the “one-dimensional atom” inequality in the bad cavity limit, the use of a cavity that couples states from the $4^2S_{1/2}$ and $3^2D_{5/2}$ manifolds presents two disadvantages. We first note that the photon generation rate of $1/g \approx 1$ ms should be compared with the time window in which the coherence between $4^2S_{1/2}$ and $3^2D_{5/2}$ is preserved, which in our setup is between $150 - 450$ μ s depending on the particular choice of the states, and it is mainly limited by magnetic field fluctuations [76]. Therefore, without precise magnetic field stabilization, coherence will be lost before a photon is generated in the cavity. Second, the repetition rate of experiments in such a setup will be strongly limited by the single-photon generation rate of one per millisecond.

To increase the single-photon generation rate, that is, to increase the coupling strength, the cavity can be tuned such that it interacts with an atomic dipole transition. Here, there are two possible choices: $4^2S_{1/2} \leftrightarrow 3^2P_{3/2}$ or $3^2P_{3/2} \leftrightarrow 3^2D_{5/2}$. The first transition corresponds to a wavelength of 393 nm, which lies in the ultra-violet regime. At such a small wavelength, it becomes extremely challenging to produce low-loss mirror coatings to build an in-vacuum high-finesse cavity which does not degrade with time. Such a cavity has been utilized in experiments presented in Refs. [77, 78], in which a finesse of 3,000 was reported. However, degradation was not discussed on these works.

A cavity that couples the $4^2P_{3/2}$ and $3^2D_{5/2}$ states then becomes favorable, as the transition corresponds to a wavelength of 854 nm. For the infrared regime, low-loss coating mirrors are routinely produced. Building a cavity satisfying $\kappa \gg g^2\kappa \gg \gamma = 2\pi \cdot 11.07$ MHz, where γ is now the decay rate of $4^2P_{3/2}$ to the both $4^2S_{1/2}$ and $3^2D_{5/2}$ (see Fig. 1), is extremely technologically demanding. For example, a high ion-cavity coupling rate, on the order of $5 - 20$ MHz, can be achieved by building a fiber-based optical cavity with a length in the order of hundreds of micrometers [34, 79, 80]. In such a case, the challenge is associated with the integration of such a small cavity together with an ion trap. However, in order to reach $\kappa \gg g^2\kappa \gg \gamma$ the decay rate from $4^2P_{3/2}$ can be effectively decreased by means of cavity-mediated Raman transitions.

consider a three-level system, with ground states $|S\rangle$ and $|D\rangle$ and a short-lived state $|P\rangle$

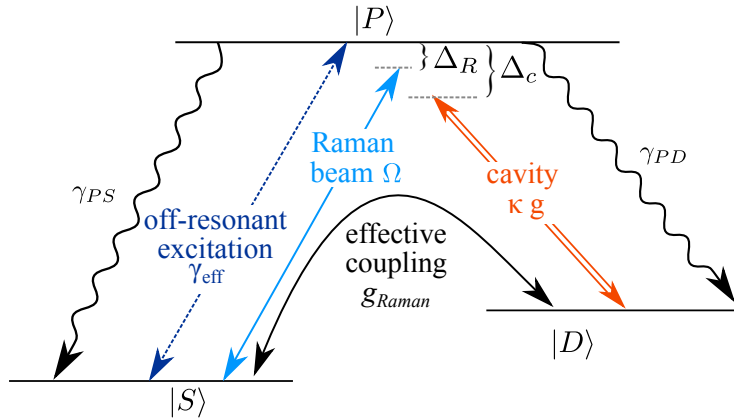


Figure 2: Schematic representation of a cavity-mediated Raman transition. A Raman laser field with Rabi frequency Ω drives the $|S\rangle \leftrightarrow |D\rangle$ transition and a cavity with field decay κ and coupling constant g couples to $|P\rangle \leftrightarrow |D\rangle$ transition. When both fields are equally detuned from the transition’s frequency, that is, $\Delta_c = \Delta_R$, the three-level system $|S\rangle$ - $|P\rangle$ - $|D\rangle$ can be mapped onto an effective two-level system $|S\rangle$ - $|D\rangle$, with an effective coupling rate g_{Raman} and an effective decay rate γ_{eff} . Here, γ_{eff} is the effective rate at which $|P\rangle$ is off-resonantly excited and subsequently decays back either to $|S\rangle$ or $|D\rangle$.

with γ_{PS} and γ_{PD} the decay rates from $|P\rangle$ to $|S\rangle$ and to $|D\rangle$. In a cavity-mediated Raman process, a Raman laser field with Rabi frequency Ω drives the $|S\rangle \leftrightarrow |D\rangle$ transition and a cavity with field decay κ and coupling constant g couples to $|P\rangle \leftrightarrow |D\rangle$ transition (see Fig. 2). Assume that both cavity and driving field are detuned by Δ_c and Δ_R respectively from the transition’s frequency. In the case that $\Delta_R = \Delta_c = \Delta$ with $\Delta \gg \{g, \kappa, \Omega\}$, the states $|S\rangle$ and $|D\rangle$ are effectively coupled, while the state $|P\rangle$ can be adiabatically eliminated [81–83]. Therefore, the three-level system $|S\rangle$ - $|P\rangle$ - $|D\rangle$ can be mapped onto an effective two-level system $|S\rangle$ - $|D\rangle$, with an effective coupling rate g_{Raman} and an effective rate γ_{eff} . Now, γ_{eff} is the rate at which $|P\rangle$ is off-resonantly excited and subsequently decays either to $|S\rangle$ or $|D\rangle$ by emitting a photon in free space (see Fig. 2). In a cavity-mediated Raman process, the “one-dimensional-atom” inequality in the bad cavity limit thus corresponds to $\kappa \gg g_{\text{Raman}}^2/\kappa \gg \gamma_{\text{eff}}$.

During the course of his doctoral thesis work, Carlos Russo has assembled an ion trap integrated with an optical cavity, with a finesse measured to be 77,000(1,000) at 854 nm and 70,000(1,000) at 866 nm [29]. With such a setup, it has been possible to reach typical effective parameters $g_{\text{Raman}} \approx 2\pi \cdot 20$ kHz and $\gamma_{\text{eff}} \approx 2\pi \cdot 10$ kHz [45], which are set by the Rabi frequency of the Raman beam and the fixed parameter $\kappa = 2\pi \cdot 50$ kHz.

Despite not being in the limit of the “one-dimensional-atom” regime, the setup has proved to be successful: The implementation of cavity-mediated Raman spectroscopy using the cavity at 866 nm and the Raman laser at 397 nm has been shown [42]. Using such a Raman scheme, the generation of single photons [17] and a quantum to classical transition in a single-ion laser [43] have been demonstrated. Later on, Raman spectroscopy using the cavity at 854 nm and the

Raman laser at 393 nm has been performed [44]. Using the cavity at 854 nm, entanglement between an ion and a photon [30] and the mapping of the state of an ion onto a photon [31] have been demonstrated. In the course of this thesis work, entanglement between two ions mediated by the optical cavity [45] and the creation of sub- and superradiant state of two ions [46] have been shown; and finally, also during this thesis work, it has been demonstrated that collective effects can be used to enhance the performance of a quantum interface [46].

In Chapter 3 of this thesis, we will explore the cavity-mediated Raman transition in details, for which a three-level system will be first considered. Next, we will identify the available Raman processes when considering all the Zeeman sublevels of the $4^2S_{1/2}$, $3^2P_{3/2}$ and $3^2D_{5/2}$ manifolds. Finally, for each of these transitions, we will derive the expression for the effective rates g_{Raman} and γ_{eff} .

3 Cavity-mediated Raman transitions

Raman transitions are an important tool of atomic physics that enable coherent population transfer between two ground states. In a ion-cavity system, Raman transitions enable the coherent generation of single photons in an optical resonator, even in the absence of the strong coupling regime [17, 84]. In order to perform the experiments presented in this thesis, we use cavity-mediated Raman transitions, in which a Raman drive laser and an optical cavity field in the vacuum state couple two stable states to a common intermediate level. When both the Raman laser and the optical cavity are detuned from the intermediate state by the same amount, the three-level system can be mapped onto an effective two-level system with an effective Raman coupling between the two stable levels.

In this chapter, we first consider a three-level system, which is then mapped onto an effective two-level system by means of a single-mode optical cavity and a Raman laser. We derive the expression for the Raman coupling rate and introduce the rate of the incoherent process in which the Raman beam off-resonantly excites population to the intermediate level. Next, we consider the specific case of a $^{40}\text{Ca}^+$ ion and introduce an additional mode of the optical cavity and a magnetic field which splits the manifolds of the $^{40}\text{Ca}^+$ electronic's structure. In this way, eighteen different Raman processes can be identified. Furthermore, we show that each transition can be individually addressed by tuning the frequency and the polarization of the driving field. Finally, we derive expressions for the Raman coupling rate of each transition and we show that the polarization of generated photons can be controlled.

Cavity-mediated Raman transitions are used extensively in this thesis. In experiments presented in Chapter 7, we use two Raman transitions in order to generate photons that are entangled in polarization with the state of each of two ions. In Chapter 8, the tunable nature of the coupling of a two-ion crystal to the cavity is demonstrated by measuring the temporal shape of photons generated by means of a Raman transition. Finally, in Chapter 9 we use two Raman transitions to transfer quantum information from a two-ion crystal to a single photon.

3.1 Three-level system coupled to a single-mode cavity

Consider a three-level system interacting with a single mode of an optical cavity and with a Raman laser. The three levels are labeled as $|S\rangle$, $|P\rangle$ and $|D\rangle$. The name of the levels are chosen in order to facilitate the application of this method to the $^{40}\text{Ca}^+$ ion that will be discussed in the next section. In this case, $|S\rangle$ and $|D\rangle$ are ground states and $|P\rangle$ is an excited state with decay rates γ_{PS} and γ_{PD} to the states $|S\rangle$ and $|D\rangle$, respectively. The cavity couples the states $|P\rangle$ and $|D\rangle$ and the Raman beam couples the states $|S\rangle$ and $|P\rangle$ (see Fig. 2).

The Hamiltonian H describing a three-level atom interacting with a quantized field of an optical cavity and with a Raman laser contains three contributions:

$$H = H_0 + H_{e-c} + H_{e-l}.$$

Energy of the system

H_0 corresponds to the bare eigenenergies of the system, that is, the energy of the emitter plus the energy of the cavity field, and it is given by

$$H_0 = \sum_{K \in \{S, P, D\}} E_K \hat{\sigma}_K + \hbar \omega_c \hat{N}$$

where $\hat{\sigma}_K \equiv |K\rangle\langle K|$ is the operator that projects the atomic state to the state $|K\rangle$, $\hat{N} \equiv \hat{a}^\dagger \hat{a}$ is the photon number operator of the cavity mode, a^\dagger and a are the photon creation and annihilation operators, E_K is the energy of the bare atomic level $|K\rangle$, and ω_c is the cavity frequency.

Atom-cavity interaction

H_{e-c} corresponds to the Jaynes-Cummings Hamiltonian [85], which describes the interaction between the emitter and the quantized field of the cavity field, and it is given by

$$H_{e-c} \equiv H_{J.C} = \hbar g_{PD} (\hat{\sigma}_{DP} \hat{a}^\dagger) + \hbar g_{PD} (\hat{\sigma}_{DP} \hat{a}), \quad (3.1)$$

where g_{PD} is the coupling strength between the emitter and the cavity field, $\hat{\sigma}_{PD} \equiv |D\rangle\langle P|$ is the lowering operator from $|P\rangle$ to $|D\rangle$ and $\hat{\sigma}_{DP} \equiv |P\rangle\langle D|$ is the raising operator from $|D\rangle$ to $|P\rangle$. The first term describes the emission process of a photon into the cavity field, a process that lowers the emitter from $|P\rangle$ to $|D\rangle$, while the second term describes the reverse process. Note that a rotating wave approximation has been performed in order to ignore the fast oscillating term at a frequency $\omega_c + (E_D - E_P)/\hbar$ [86].

In the dipole approximation, and assuming that the emitter is well-localized within the resonator's standing wave, the maximum atom-cavity coupling strength g_{PD} is given by the scalar product of the atomic dipole moment $\vec{\mu}_{PD}$ and the electric field \vec{E} at the cavity antinode:

$$\hbar g_{PD} = \vec{\mu}_{PD} \cdot \vec{E}_{PD} = \hbar \sqrt{\frac{3c\gamma_{PD}\lambda}{L\omega_0^2\pi^2}}. \quad (3.2)$$

where λ is the wavelength of the $|P\rangle \leftrightarrow |D\rangle$ transition, L is the length of the resonator and ω_0 is the waist of the cavity mode, assuming a TEM_{00} mode.

Atom-laser interaction

H_{e-l} describes the interaction between the emitter and the Raman laser using a semiclassical approach, and it is given by

$$H_{e-l} = \frac{\hbar\Omega}{2} (\hat{\sigma}_{SP} e^{i\omega_l t} + \hat{\sigma}_{PS} e^{-i\omega_l t}) \quad (3.3)$$

where $\hat{\sigma}_{SP} \equiv |P\rangle\langle S|$ is the raising operator from $|S\rangle$ to $|P\rangle$, $\hat{\sigma}_{PS} \equiv |S\rangle\langle P|$ is the lowering operator from $|P\rangle$ to $|S\rangle$ and ω_l is the frequency of the Raman laser. The first term of H_{e-l}

describes the absorption process of a photon from the Raman field, a process that raises the emitter from $|S\rangle$ to $|P\rangle$, while the second terms describe the reverse process.

The coupling strength between the Raman beam and the atom is given by the Rabi frequency Ω , which is calculated as the scalar product of $\vec{\mu}_{SP}$ and the electric field of the Raman beam \vec{E}_{SP} :

$$\hbar\Omega = \vec{\mu}_{SP} \cdot \vec{E}_{SP}. \quad (3.4)$$

Interaction picture: Removing the time dependency

The time dependence of H_{e-1} can be removed by moving to the interaction picture [86] via a unitary transformation \hat{U} . The operator \hat{U} maps the state of the system $|\psi\rangle$ to a state $|\psi'\rangle = \hat{U}|\psi\rangle$, and the Hamiltonian H transforms into $\mathcal{H} = \hat{U}H\hat{U}^\dagger - i\hbar\hat{U}\frac{d\hat{U}^\dagger}{dt}$ [86]. For the system under consideration, a suitable transformation is given by $\hat{U} = e^{i\hat{\sigma}_S\omega_l t}$. Additionally, the zero reference energy of the system is redefined to $|P\rangle$ by subtracting E_P from the energy of all states. In the interaction picture, the Hamiltonian of the system is given by

$$\begin{aligned} \mathcal{H}_0 &= \hbar\Delta_l\hat{\sigma}_s + (E_D - E_P)\hat{\sigma}_D + \hbar\omega_c\hat{N} \\ \mathcal{H}_{\text{int}} &= \mathcal{H}_{e-c} + \mathcal{H}_{e-1} = \frac{\hbar\Omega}{2}\sigma_{SP} + \hbar g(\hat{\sigma}_{PD}a^\dagger) + \text{h.c.}, \end{aligned} \quad (3.5)$$

where $\Delta_l = (E_S - E_P)/\hbar - \omega_l$ is the detuning of the laser from the $|S\rangle \leftrightarrow |P\rangle$ transition (see Fig. 2).

In a frame that rotates at the laser frequency ω_l , the Hamiltonian \mathcal{H}_{int} describes coherent population transfer between

$$|S\rangle|n\rangle \leftrightarrow |P\rangle|n\rangle \quad \text{and} \quad |P\rangle|n\rangle \leftrightarrow |D\rangle|n+1\rangle, \quad (3.6)$$

where n is the cavity photon number in the Fock state basis, $\hat{N}|n\rangle = n|n\rangle$.

In the case that the decay rates γ_{PS} and γ_{PD} are the slowest rate of the system, that is, $\{\gamma_{PS}, \gamma_{PD}\} \ll \{\Omega, g_{PD}, \Delta_l\}$, for times $t \ll 1/\text{Max} \in \{\gamma_{PS}, \gamma_{PD}\}$, the system will evolve coherently according Eq. 3.6 until the emitter decay to $|S\rangle$ or $|P\rangle$. In the case that either γ_{PS} or γ_{PD} is the dominant rate, the Hamiltonian description is not sufficient as it includes neither the atomic nor the cavity decay. In such a case, for a complete description of the system, a master equation formalism is necessary. However, in the next section we will see that the effects of γ_{PS} or γ_{PD} can be effectively decreased by minimized the excitation to $|P\rangle$.

Effective two-level system: Raman resonance condition

In order to minimize the role of the atomic decay from $|P\rangle$, the cavity can be detuned by $\Delta_c = \omega_c - (E_P - E_D)/\hbar$ from the $|P\rangle \leftrightarrow |D\rangle$ transition (see Fig. 2). When the detunings $\Delta_{c,l}$ are set such that $\Delta_{l,c} \gg \{g_{PD}, \Omega, \gamma_{PS}, \gamma_{PD}\}$, the state $|P\rangle$ can be adiabatically eliminated [81–83]

by a second unitary transformation [82, 83]. The calculation is carried out in Ref. [29], and here we summarize the results. The second unitary transformation corresponds to $\hat{U} = e^{\hat{S}}$, with

$$\hat{S} = \frac{\Omega}{2\Delta_l}(\hat{\sigma}_{SP} - \hat{\sigma}_{PS}) + \frac{g}{\Delta_c}(\hat{a}^\dagger \hat{\sigma}_{DP} - \hat{a} \hat{\sigma}_{PD}).$$

By applying the transformation and expanding $H' = \hat{U}\mathcal{H}\hat{U}^\dagger$ in a power series of $1/\Delta_l$ and $1/\Delta_c$, and keeping the first order of the expansion, one obtains $H' = H'_0 + H'_{\text{Raman}} + H'_{\text{AC}}$, where

$$\begin{aligned} H'_0 &= \mathcal{H} = \hbar\Delta_l \hat{\sigma}_S + (E_D - E_P)\hat{\sigma}_D + \hbar\omega_c \hat{N}, \\ H'_{\text{Raman}} &= \frac{\hbar g_{PD}\Omega}{4} \left(\frac{1}{\Delta_l} + \frac{1}{\Delta_c} \right) (\hat{a}^\dagger \hat{\sigma}_{SD} + \hat{a} \hat{\sigma}_{DS}), \end{aligned}$$

and H'_{AC} describes an energy shift of the $|S\rangle$ and $|P\rangle$ states due to the drive laser and the cavity fields [76]. As discussed in Ref. [76], this energy shift had played an important role for the ion-photon state mapping protocol [31].

Such a transformation results in a Raman coupling between the states $|S\rangle$ and $|D\rangle$ described by the lowering atomic operator $\hat{\sigma}_{SD} = |D\rangle\langle S|$ present in H'_{Raman} [29]. When the Raman resonance condition is met, that is,

$$\Delta_c = \Delta_l = \Delta \quad (3.7)$$

the Raman coupling is given by

$$g = \frac{\Omega g_{PD}}{2\Delta}. \quad (3.8)$$

The Hamiltonian H' describes the coherent population transfer between the states

$$|S\rangle |n\rangle \leftrightarrow |D\rangle |n+1\rangle, \quad (3.9)$$

while $|P\rangle$ is decoupled from the process. In the case that the emitter is prepared in $|S\rangle$ in an empty cavity, driving the Raman process for a time $1/2g$ results in the emitter in $|D\rangle$ and a cavity photon [17, 84, 87].

Although the population of $|P\rangle$ is suppressed by the Raman transition, it is not zero, due to off-resonant excitation. Subsequently, the emitter decays back to either $|S\rangle$ or $|D\rangle$, and the coherent process is interrupted. For the parameter regime $\Delta_{c,l} \gg \{\Omega, g_{PD}, \gamma\}$ where $\gamma = \gamma_{PD} + \gamma_{PS}$, following the derivation of Ref. [29], the rate γ_{eff} of off-resonant excitation to $|P\rangle$ can be approximated by

$$\gamma_{\text{eff}} = \gamma \left(\frac{\Omega}{2\Delta} \right)^2. \quad (3.10)$$

Given the Raman process, we now estimate how much off-resonant excitation influences the coherent transfer described in Eq. 3.9 by calculating the ratio

$$\frac{g}{\gamma_{\text{eff}}} = \frac{g_{PD}\Delta}{\gamma\Omega}. \quad (3.11)$$

During the course of the experiments described in this thesis, we use ranges of parameters that lead to a ratio $g/\gamma_{\text{eff}} \approx 1 - 5$. In the case that the cavity is used without a Raman laser, the ratio $g_{PD}/\gamma \approx 0.1$. The Raman transition thus increases this ratio by more than ten times. One should be aware that the ratio g/γ_{eff} can be increased indefinitely by increasing Δ or by decreasing Ω . However, by doing so, the value of g is simultaneously decreased (Eq. 3.8). In a realistic experimental environment, the minimum affordable value for the rate g is determined by the atomic coherence times, the linewidth of the Raman laser and detector dark counts.

In summary, the Raman process introduced in this section allows us to effectively increase the ratio g/γ_{eff} between a coherent process and an incoherent one. In this way, our setup can reach the ‘‘one-dimensional-atom’’ regime in the bad cavity limit, a requirement for a coherent cavity-based quantum interface (Section 2.2 and Ref. [66]). In the next section, we will consider the $^{40}\text{Ca}^+$ ion introduced in Chapter 2, and we will see that introducing a magnetic field allows us to identify eighteen different Raman transitions.

3.2 Twelve-level system coupled to two cavity modes

Consider the $^{40}\text{Ca}^+$ ion and its level structure shown in Fig 1. The states are labeled by the quantum numbers $n^{2S+1}L_J$, with the principal quantum number n , the spin multiplicity $2S + 1$, the quantum number for the orbital angular momentum L and the quantum number for the total angular momentum J . The nuclear spin of the isotope of the $^{40}\text{Ca}^+$ ion is zero.

The degeneracy in the total angular momentum is lifted by an applied magnetic field \vec{B} . We choose the conventional quantization axis parallel to the magnetic field axis. Each manifold with quantum number J is split into $2J + 1$ Zeeman sublevels m_J , with energy shift

$$\Delta E_{J,m_J} = \hbar m_J g_J \mu_B B, \quad (3.12)$$

where μ_B is the Bohr magneton and g_J is the Landé factor of the $n^{2S+1}L_J$ manifold.

We now identify the states $|S\rangle$, $|P\rangle$ and $|D\rangle$ introduced in the previous section with the Zeeman sublevels of the $^{40}\text{Ca}^+$ ion:

$$\begin{aligned} |S_i\rangle &\equiv |4^2S_{1/2}, m_J = i\rangle & i \in \{+1/2, -1/2\} \\ |P_j\rangle &\equiv |4^2P_{3/2}, m_J = j\rangle & j \in \{+3/2, +1/2, -1/2, -3/2\} \\ |D_k\rangle &\equiv |3^2D_{5/2}, m_J = k\rangle & k \in \{+5/2, +3/2, +1/2, -1/2, -3/2, -5/2\}, \end{aligned}$$

where $4^2S_{1/2}$, $3^2D_{5/2}$ and $4^2P_{3/2}$ are the three $^{40}\text{Ca}^+$ manifolds shown in Fig. 1. $|S_i\rangle$ are ground states, $|P_j\rangle$ are short-lived excited states with decay rate $\gamma_{PS} = 2\pi \cdot 10.7$ MHz and $\gamma_{PD} = 2\pi \cdot 0.675$ MHz and $|D_k\rangle$ are long-lived excited states with decay rate $2\pi \cdot 0.068$ Hz. For these manifolds, the Landé factors are given by $g_{S_{1/2}} = 2$, $g_{P_{3/2}} = 4/3$ and $g_{D_{5/2}} = 6/5$.

The cavity is tuned such that its field interacts with one of the atomic dipole transition $|P_j\rangle \leftrightarrow |D_k\rangle$ at 854 nm with $|j - k| = |\delta m_J^{PD}| \leq 1$, where m_J^{PD} is the change of the total

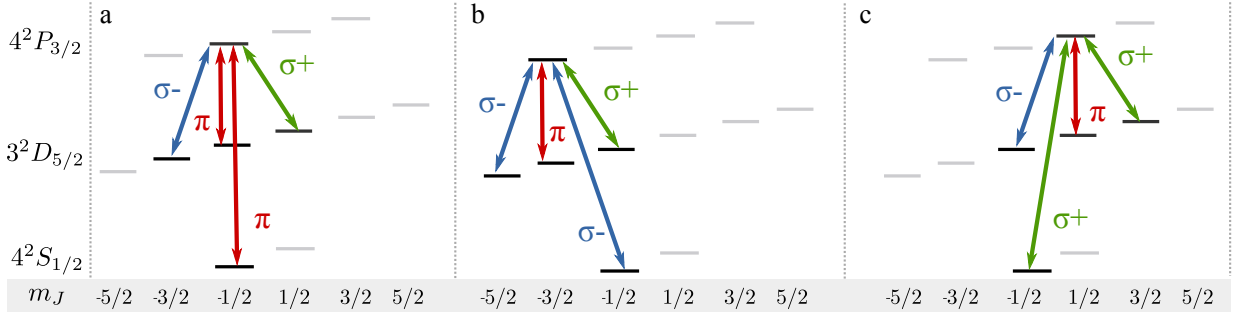


Figure 3: Representation of the nine $|S_{-1/2}\rangle \rightarrow |P_j\rangle \rightarrow |D_k\rangle$ allowed Raman transitions. Along with the other nine transitions starting from $|S_{+1/2}\rangle$ (not shown), they are in total eighteen different Raman transitions. (a) A beam linearly polarized along the magnetic field direction drives a π -transition between the $4^2S_{1/2}$ and $4^2P_{3/2}$ manifolds. (b) A left-circularly polarized beam, which propagates parallel to the magnetic field axis, drives σ^- -transitions between the $4^2S_{1/2}$ and $4^2P_{3/2}$ manifolds. (c) A right-circularly polarized beam, which propagates parallel to the magnetic field axis, drives σ^+ -transitions between the $4^2S_{1/2}$ and $4^2P_{3/2}$ manifolds. Degenerate π - and σ^\pm -transitions between the $4^2P_{3/2}$ and $3^2D_{5/2}$ manifolds can be selected by means of the frequency of the driving beam.

angular momentum of the ion along the quantization axis due to the interaction with the cavity. The frequency of the Raman beam is adjusted such that its field couples the one of the $|S_i\rangle \leftrightarrow |P_j\rangle$ transition at 393 nm with $|i - j| = |\delta m_J^{SP}| \leq 1$, where m_J^{SP} is the change of the total angular momentum due to the interaction with the Raman beam. There are eighteen allowed Raman transitions that satisfy $|\delta m_J| \leq 2$ where $\delta m_J = \delta m_J^{SP} + \delta m_J^{PD} = ((i - j) + (j - k))$. In Fig. 3, the nine transitions that start from $|S_{-1/2}\rangle$ are indicated.

As each state is shifted in energy according to Eq. 3.12, the eighteen allowed Raman transitions are shifted in frequency by [76]

$$\Delta\nu_{i \leftrightarrow k} = \mu_B B (g_{D_{5/2}} m_i - g_{S_{1/2}} m_k).$$

where the frequency reference is given by $(E_S - E_D)/\hbar$. Note that the energy shift of $|P_j\rangle$ does not play a role as the zero reference energy of the system has been defined to $|P_j\rangle$ (Eq. 3.5). Transitions with $\delta m_J = \pm 2$ are nondegenerate in frequency, transitions with $\delta m_J = \pm 1$ are doubly degenerate and transitions with $\delta m_J = 0$ are triply degenerate. Degenerate transitions, however, can be individually addressed by means of the polarization of the driving beam.

A beam linearly polarized along the magnetic field axis drives transitions that satisfy $\delta m_J^{SP} = 0$, that is, π -polarized transitions between the $4^2S_{1/2}$ and $4^2P_{3/2}$ manifolds (see Fig. 3a). A circularly polarized beam propagating along the magnetic field axis drives transitions that satisfy $\delta m_J^{SP} = \pm 1$, that is, σ^\pm -polarized transitions between the same manifolds (Fig. 3b-c). Finally, π - and σ^\pm -transitions between the $4^2P_{3/2}$ and $3^2D_{5/2}$ manifolds satisfy $\delta m_J^{PD} = 0$ and $\delta m_J^{PD} \pm 1$ respectively.

The derivation in Section 3.1 can be extended in order to calculate effective rates of Raman transitions $|S_i\rangle \leftrightarrow |D_k\rangle$ via the intermediate state $|P_j\rangle$. The Rabi frequency of each Raman transition, that is, the effective coupling strength between states $|S_i\rangle$ and $|D_k\rangle$ via the intermediate state $|P_j\rangle$, can be written as [44]

$$g(i, j, k) = \frac{\xi_{S_i P_j D_k} \zeta_{P_j D_k} \Omega g_{PD}}{\Delta}. \quad (3.13)$$

Here, Δ is the detuning of the Raman beam and the cavity to the $|P_j\rangle - |D_k\rangle$ transition and to the $|S_i\rangle - |P_j\rangle$ transition respectively, $\zeta_{P_j D_k}$ is a geometric factor that takes into account the projection of the cavity vacuum-mode polarization onto the atomic dipole moment and $\xi_{S_i P_j D_k}$ is the product of the Clebsch-Gordon coefficients of the $|S_i\rangle - |P_j\rangle$ and $|P_j\rangle - |D_k\rangle$ transitions. Finally, g_{PD} is the maximum coupling rate between the ion and the cavity (Eq. 3.2).

Calculating the effective Raman coupling

Given a specific Raman transition $|S_i\rangle \rightarrow |D_k\rangle$ via an intermediate state $|P_j\rangle$, the calculation of $g(i, j, k)$ is described as follows. First, the product of Clebsch-Gordon coefficients $\xi_{S_i P_j D_k}$ is calculated from the values shown in Fig. 4. Next, in order to calculate $\zeta_{P_j D_k}$, the projection of the vacuum-mode polarization onto the atomic dipole moment, it is necessary to consider the geometry of the setup. In the experiments presented in this thesis¹, the magnetic field $\vec{B} = B\hat{B}$ is aligned perpendicular to the cavity axis \hat{x} . Our cavity allows two orthogonal polarization modes which are considered to be degenerate as the frequency difference is smaller than the linewidth of the cavity ($2\pi \cdot 50$ kHz). We define the vertically-polarized mode (V) of the cavity such that photons in that mode are polarized along $\hat{V} = \hat{B}$ and the horizontal mode (H) such that photons in that mode are linearly polarized in the direction $\hat{H} = \hat{x} \times \hat{V}$ orthogonal to both \hat{x} and \hat{V} (see Fig. 5a).

When π -polarized transitions between the $4^2P_{3/2}$ and $3^2D_{5/2}$ manifolds are driven, that is, transitions that satisfy $\delta m_J^{DP} = 0$, the generated photons are linearly polarized such that their electric fields $\vec{E}_V = \hat{V}E$ is aligned along \hat{V} (Fig. 5b). In such a way, photons generated while driving π -transitions couple to the V mode of the optical cavity, that is,

$$\zeta_{P_j D_j} = 1 \quad \text{for} \quad j \in \{+3/2, +1/2, -1/2, -3/2\}.$$

When σ^\pm -polarized transitions between the $4^2P_{3/2}$ and $3^2D_{5/2}$ manifolds are driven, that is, transitions that satisfy $\delta m_J^{DP} = \pm 1$, photons are circularly polarized. The electric field of circularly polarized photons \vec{E}_{σ^\pm} can be written in terms of two linearly polarized electric fields that oscillate with a relative phase of $\pi/4$ between them:

$$\vec{E}_{\sigma^\pm}(t) = \vec{E}_H(t) + \vec{E}_x(t) = \frac{E}{\sqrt{2}}(\hat{H} \cos(\omega t) \pm \hat{x} \sin(\omega t))$$

¹ As two magnetic field configurations are used during experiments presented in this thesis, we use \hat{B} to denote the quantization axis and leave \hat{z} for the fixed trap axis, which is defined later on in Fig. 6.

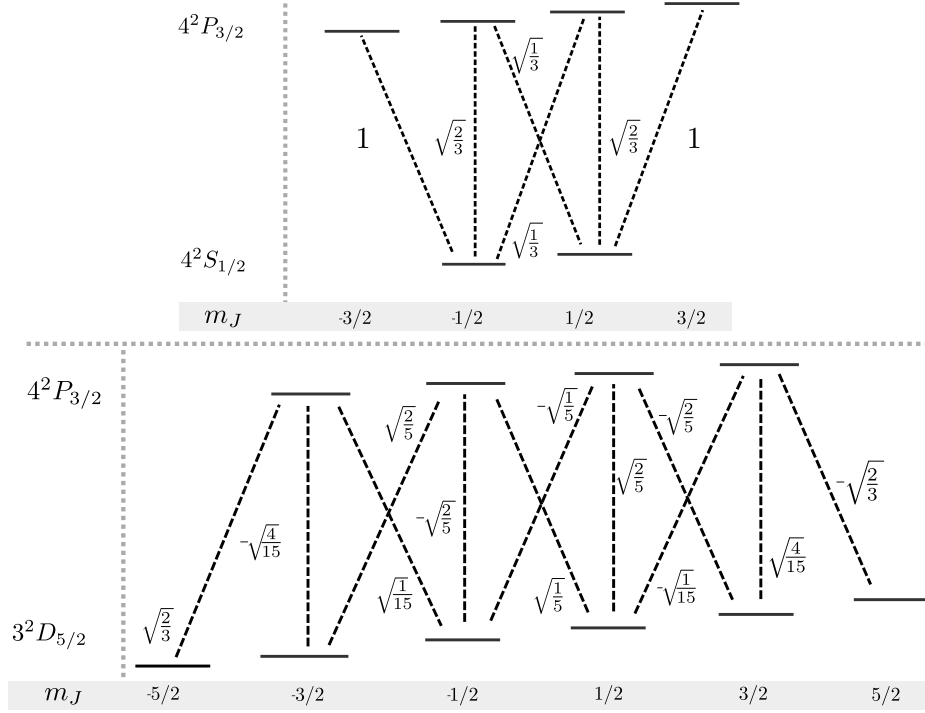


Figure 4: Clebsch-Gordan coefficients for the $|S_i\rangle - |P_j\rangle$ and for the $|P_j\rangle - |D_k\rangle$ transitions.

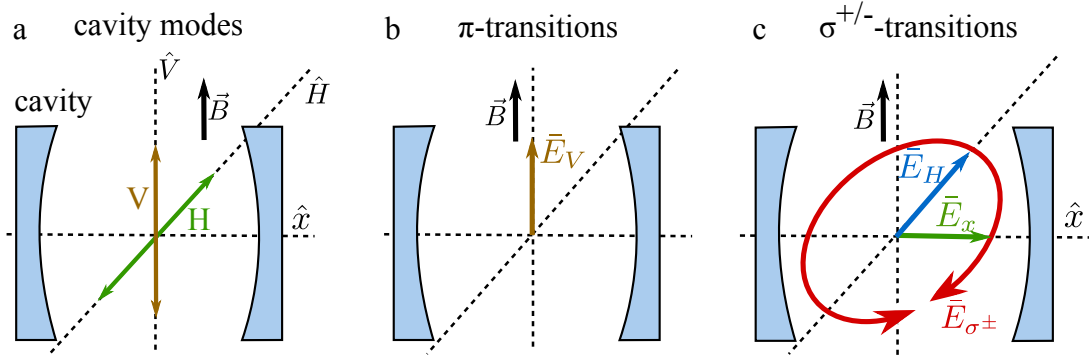


Figure 5: (a) Cavity modes: the vertical mode (V) of the cavity is defined such that photons in that mode are polarized along $\hat{V} = \hat{B}$ and the horizontal mode (H) such that photons on that mode are linearly polarized in the direction $\hat{H} = \hat{x} \times \hat{V}$. (b) π -polarized transitions between $4^2P_{3/2}$ and $3^2D_{5/2}$ generate photons that are linearly polarized such that their electric field $\vec{E}_V = \hat{V}E$ are aligned along \hat{V} . (c) σ^\pm -polarized transitions between $4^2P_{3/2}$ and $3^2D_{5/2}$ generate photons which are circularly polarized. The electric field of circularly polarized photons \vec{E}_{σ^\pm} can be written in terms of two linearly polarized electric fields: $\vec{E}_{\sigma^\pm}(t) = \vec{E}_H(t) + \vec{E}_x(t)$.

where $\vec{E}_H(t)$ and $\vec{E}_x(t)$ are the components of the electric field $\vec{E}_{\sigma^\pm}(t)$ along the cavity axis \hat{x} and \hat{H} respectively (see Fig. 5c). The electric field $\vec{E}_x(t)$ cannot propagate along the cavity axis direction \hat{x} , and therefore does not couple to the cavity². The electric field $\vec{E}_H(t)$ couples to the H mode of the optical cavity, and therefore

$$\zeta_{P_j D_i} = 1/\sqrt{2} \quad \text{for} \quad i - j = \pm 1.$$

Similarly, the geometric factor $\zeta_{P_j D_k}$ can be calculated for a situation in which the magnetic field is aligned parallel to the cavity axis [44].

In conclusion, in the previous section we have seen that by means of a Raman process, we can reach the “one-dimensional-atom” regime in the bad cavity limit in our experimental setup, a requirement for the implementation of a coherent cavity-based quantum interface. In this section we have described eighteen Raman transitions between twelve levels of a $^{40}\text{Ca}^+$ ion. The transitions can be used to generate cavity photons in the horizontal (H) or the vertical (V) mode of the optical cavity. The different transitions can be individually addressed by means of the frequency and the polarization of the Raman beam. Spectroscopy of the eighteen Raman transitions and a polarization analysis of generated photons was carried out in Refs. [44, 76].

In the experiments presented in Chapter 7, the Raman beam propagates along the magnetic field axis. The polarization of the beam has been set such that σ^- -polarized transitions are driven. For the experiments presented in Chapters 8 and 9, the Raman beam propagates in a direction perpendicular to both the magnetic field axis and the cavity axis. The polarization of the beam has been aligned parallel to the magnetic field such that π -polarized transitions are driven.

² At the center of an optical cavity, $\vec{k} \perp \vec{E}$, where \vec{E} is the electric field of the resonant with wavenumber \vec{k} .

4 The experimental setup

In the previous chapter, we have introduced an important tool for this thesis: the cavity-mediated Raman transition. We have derived expressions for the Raman coupling of each of the eighteen transitions, and we have seen that the polarization of the generated photons can be controlled by the choice of transition. In this chapter, we first summarize the relevant aspects of the ion trap and the optical cavity, which together with the Raman 393 nm beam are the key components involved in the Raman process. We also describe the setup used to study the polarization state of cavity photons, and the current values for photon losses and photon detection efficiencies are discussed.

Additionally, the laser fields utilized during the course of this thesis are introduced. Next, the changes recently implemented in the optical path of the 729 nm laser beam are described, which is used to drive quadrupole transitions between the $3^2D_{5/2}$ and $4^2S_{1/2}$ manifolds. These changes allow both global and addressing pulses of monochromatic or bichromatic 729 nm light in a single experimental sequence. This control was required for the implementation of the experiments presented in Chapters 8 and 9. Measurements in three dimensions of the profile of the addressing beam, installed by Diana Habicher [88], are then shown and discussed.

4.1 Ion trap

In our experimental setup we use a linear Paul trap, which consists of an oscillating electric field and a static electric field, to confine a $^{40}\text{Ca}^+$ ion in space [50]. This section is not meant to describe the operation of a linear Paul trap comprehensively, but rather to summarize relevant information about the ion trap used in the experiments presented in this thesis. A comprehensive description of the operation principle of the linear Paul trap can be found in the doctoral thesis of Christian Roos [72].

The trap was built by Carlos Russo, and a full description of the fabrication process can be found in his doctoral thesis [29]. The trap has two pairs of blade electrodes (four blades in total), two trap endcaps, and two further electrodes used for micromotion compensation. The line connecting the trap endcaps is defined as the trap axis.

The $^{40}\text{Ca}^+$ ions are confined in the radial plane of the trap, which is the plane orthogonal to the axial direction, by a quadrupole pseudopotential. The quadrupole pseudopotential is generated by applying an oscillating radiofrequency (RF) voltage to two opposite blade electrodes, while the other two blade electrodes are grounded. A helical resonator with a quality factor of 200 serves to amplify the RF voltage. The helical resonator with the trap as a capacitive load has a resonance frequency around 23.4 MHz, which is the frequency used to drive the oscillating RF voltage.

Confinement along the trap axis is achieved by applying a positive voltage to both trap endcaps. The distance between the endcaps is 4 mm. The voltage is provided by an ultra-

stable high voltage power supply, capable of generating up to 1000 V, with voltage fluctuations between one part in 10^{-5} to 10^{-6} . Low noise is crucial in the experiments presented in this thesis. In Section 5.8 we describe the implementation of the Mølmer–Sørensen gate, which requires a precisely calibrated detuning from the axial sidebands frequency, which in turn are determined by the voltages applied to the trap endcaps.

During experiments we apply voltages between 200–900 V to the endcaps, which translates to axial trap frequencies ω_a between 450 kHz and 1.1 MHz measured by spectroscopy on the $3^2D_{5/2} - 4^2S_{1/2}$ transition. Driving the trap with a 5 W signal at 50Ω results in a radial trapping frequency of $\omega_r \approx 3$ MHz, also measured by spectroscopy. In Chapter 6 we describe how the individual couplings of two ions to an optical cavity are tuned by changing the axial frequency.

Micromotion is the oscillation of an ion at the trap RF drive frequency, which appears when the ion is not located at the potential minimum of the quadrupole pseudopotential [72]. Micromotion in all three directions is compensated by adjusting the voltages on the electrodes that shift the ion’s position in the radial plane and the voltages applied to the trap endcaps that shift the ion’s position along the trap axis (see Ref. [76] for a detailed description of the micromotion compensation procedure in our system). In our experiment micromotion can be reduced such that the ratio $\Omega_{\hat{k}}/\Omega$ is below 5% in any direction \hat{k} , where $\Omega_{\hat{k}}$ is the Rabi frequency of driven oscillations on the micromotion sideband of a $3^2D_{5/2} - 4^2S_{1/2}$ transition along \hat{k} , and Ω is the Rabi frequency of driven oscillations, with the same power, on the carrier transition.

In order to load $^{40}\text{Ca}^+$ ions into the trap, a calcium oven is heated by a current of 4.7 A. Neutral calcium is emitted from the oven to the trap through a hole in the cavity holder. The hole serves as a beam collimator such that calcium is not spattered onto the cavity mirrors. Finally, the neutral atoms are ionized in the trapping volume by two laser beams at 422 and 375 nm [29]. Up to now, experiments in our setup have been performed using one or two ions. However, by decreasing the radial confinement and increasing the intensity of the cooling 397 nm beam, I have been able to crystalize up to four ions.

In our setup, the heating rate of the axial mode has been measured to be 1.2(2) motional quanta per second [76]. We note that this value is very similar to the one observed in [61] for a similar trap design and represents one of the lowest ion-trap heating rates ever measured [89]. Due to the low heating rate and to the strong confinement, ions remain in the trap even in the absence of cooling beams.

The operation time with the same string of ions, however, is limited by chemical reactions between the ions and the background gas. In this case, the ions form molecules which cannot longer be excited by the lasers. The molecules are thus not useful to carry out experiments, and therefore a new string of ions should be load. In general, we can perform experiments for several hours, between two and twenty, before a chemical reaction occurs. Normal values for the pressure inside our vacuum vessel are close to $1 \cdot 10^{-10}$ millibars.

The main problem associated with the process of loading ions is that the oven is not ther-

mally isolated from the vacuum vessel or the cavity. After loading ions, the holders of the cavity mirror are heated, and the process of rethermalization usually lasts between two and three hours. During that period of time, the length of the cavity drifts, and therefore it is not possible to carry out experiments that use the cavity.

It might be interesting to investigate the origin of the chemical reactions in order to decrease the rate at which they occur. The investigation can be performed by means of mass spectroscopy measurements [90]. In case that residual water is not the main responsible of such reactions, illuminating the electrodes of the trap with UV light might help to decrease the rate. In case that residual water is the responsible of such reactions, the only feasible solution might be a reassembly of the vacuum vessel in order to extract the water. Such a solution should be considered as extreme. After the optical cavity is aligned in air, the baking process affects the alignment of the cavity to the point that, after the baking, the mirrors no longer form a cavity. Although it is not mentioned in his doctoral thesis, Carlos Russo has assembled the setup several times until the cavity remained aligned in vacuum after the baking process.

4.2 The optical cavity

At the heart of our experiment lies the optical cavity, which serves as a coherent interface between $^{40}\text{Ca}^+$ ions and single photons. The optical cavity was designed and assembled by Carlos Russo, and a full characterization of the cavity can be found in his doctoral thesis [29].

Due to asymmetric mirror transmissions, the cavity field decays preferentially through one mirror of the resonator. The cavity is in a near-concentric configuration in order to minimize the mode waist. This configuration maximizes the coupling strength between the cavity field and the ion, as the coupling strength is inversely proportional to the mode volume (see Eq. 3.2).

In his doctoral thesis, Carlos Russo reported a cavity length of $L = 19.9159(5)$ mm derived from measurements of the frequency splitting of the TEM_{00} and TEM_{01} modes [29]. The frequency splitting depends on both L and the radius of curvature R of the two mirrors. In order to extract L , Carlos Russo assumed the manufacturer-specified value of $R = 10$ mm.

In 2012, Andreas Stute remeasured R and L [76]. The mirror distance $L = 19.96(2)$ mm had been determined by a measurement of the cavity's free spectral range. Then, combining the results of a measurement of the frequency splitting of the TEM_{00} and TEM_{01} with the value of the free spectral range, the radius of curvature has been inferred to be $R = 10.02(1)$ mm.

In the experiments presented in Chapters 7-9, the cavity couples the $3^2D_{5/2}$ and $4^2P_{3/2}$ manifolds at a wavelength $\lambda = 854$ nm. For this wavelength, the cavity waist is calculated to be

$$w_0 = \sqrt{\frac{\lambda}{2\pi}(L(2R - L))^{1/2}} = (13.2 \pm 0.8) \mu\text{m}$$

and the finesse was measured to be $\mathcal{F} = 77,000 \pm 1,000$ [29]. In 2015, Moonjoo Lee again performed a measurement of the finesse via the cavity ring-down technique, obtaining a value

of $\mathcal{F} = 77,000 \pm 3,000$. It is remarkable that despite the setup being under vacuum for almost ten years, we have no evidence that the finesse has changed in this time.

Using the values for \mathcal{F} , L and R , the cavity decay κ and the maximum coupling strength between the ion and the cavity on the $3^2D_{5/2}$ and $4^2P_{3/2}$ manifolds g_{PD}^{MAX} are calculated to be

$$\begin{aligned}\kappa &= \frac{2\pi c}{4L\mathcal{F}} = 2\pi \times (48.8 \pm 0.6) \text{ kHz} \\ g_{PD}^{\text{MAX}} &= \sqrt{\frac{3c\gamma_{PD}\lambda^2}{\pi^2 L w_0^2}} = 2\pi \times (1.43 \pm 0.01) \text{ MHz},\end{aligned}$$

where $\gamma_{PD} = 2\pi \times 0.675$ MHz is the spontaneous decay rate from the $4^2P_{3/2}$ manifold.

The optical cavity was built on top of two piezoelectric stacks for cavity-length stabilization in order to stabilize the resonance frequency. The cavity-length stabilization technique is described in Ref. [76]. The idea is to transfer the stability of a reference cavity to the experiment cavity via laser light [29, 73]. A reference laser at 785 nm is stabilized to the reference cavity and then used to stabilize the optical cavity via active feedback to a piezoelectric stack. The finesse of the reference cavity at 785 nm and the linewidth of the reference laser have been measured to be 2000 and 500 kHz [29, 76].

In the past [30, 31, 44–46], we have reported a reduced coupling strength between the ion and the cavity of $g_{SD}^{\text{obs}} \approx 0.9(2)$ MHz. We attributed the discrepancy between the observed value g_{SD}^{obs} and g_{SD}^{MAX} to residual motion of the ion with respect to the cavity [76].

Current analysis indicates that a jitter in the resonance frequency of the experiment cavity may be responsible for the reduced coupling. In this case, the jitter in the resonance frequency is introduced by the non-zero linewidth of the 785 nm laser and by the performance of the electronics involved in the cavity-length stabilization. Konstantin Friebe and Moonjoo Lee are currently working on the stabilization setup, and they have already been able to see evidence of an increased $g_{SD}^{\text{obs}} \approx 1.3$ MHz. In order to obtain the value of g^{obs} , they matched simulations of the temporal shape of cavity photons with data. In the context of his doctoral thesis, Konstantin Friebe will discuss the jitter in the resonance frequency of the experiment cavity and its implications.

The two piezoelectric stacks are mounted above two slip-stick piezo stages which translate the cavity in the plane perpendicular to the trap axis [29]. This allows us to align the cavity with respect to the ions with a precision on the order of tens of nanometers. In Chapter 6 we describe how the individual coupling of two ions to the optical cavity is tuned by changing the cavity position with respect to the ion trap at different axial trapping frequencies, that is, for different ion–ion separations.

Finally the output coupling efficiency η_{out} , that is, the probability that a cavity photon leaves the cavity, was calculated to be 16.0(15)% at 854 nm [29]. However, estimations performed by Andreas Stute reveal that this value is close to 20% [76]. For these estimations, single cavity photons were produced and the probability of detecting the photon was measured. The output coupling efficiency η_{out} is determined after accounting for the imperfect detection path

efficiency, which can be independently characterized. We repeated the procedure performed by Stute, and as a result, we calculate that $\eta_{out} = 20(2)\%$. See Section 4.4 for an analysis of the detection path efficiency and for details related with the calculation of η_{out} .

In order to understand the origin of the discrepancy between the value given in Ref. [29] and our estimation, we note that the calculation in Ref. [29] is based on measurements of the total losses in the cavity, which depend on the intensity transmission coefficients of the cavity mirrors. The transmission coefficient of the output mirror at 854 nm has been measured to be 13(1) ppm. The relative error of that value is three times smaller than the error given for the same mirror at 866 nm, and than the error given for the other mirror at both wavelengths (see page 52 of Ref. [29]). We therefore believe that the error in the value of the transmission coefficient of the output mirror at 854 nm was underestimated, resulting in a underestimated error for the calculated value of η_{out} .

4.3 Laser system

To perform the experiments presented in this thesis, we use laser light to address different transitions of the $^{40}\text{Ca}^+$ ion. The laser at 397 and 866 nm are used for Doppler cooling and ion state detection, and the laser at 854 nm for removing population from the $3^2D_{5/2}$ manifold. The lasers at 375 and 422 nm are used for the ionization of neutral calcium atoms. These lasers are shared with three other experiments; “LinTrap,” “Fiber Cavity” and “Segmented Trap,” which is currently not operating. A detailed description of the setup that has been built to distribute the light between the experiments and a characterization of the lasers can be found in Refs. [29,91].

The laser at 393 nm is used for the Raman transition, and the laser at 785 nm is used to stabilize the length of the experiment cavity. These lasers are currently not shared with other experiments; however, they will be shared with the Fiber Cavity experiment once the setup is ready to operate with Raman transitions [34]. The lasers and the optical paths of these lasers are described in detail in Ref. [44].

We now define a coordinate system in which the ion is located at the origin. In this coordinate system, \hat{x} points along the cavity axis, \hat{z} points along the trap axis, that is, the axis connecting the trap endcaps, and \hat{y} is the radial direction of the cavity orthogonal to both \hat{x} and \hat{z} (see Fig. 6). The Raman beam is directed to the ion from the $(-\hat{y} + \hat{z})$ direction. The polarization of the beam can be changed by adjusting the angles of quarter- and half-waveplates installed before the vacuum chamber (not shown in Fig. 6) in order to selectively drive σ^\pm or π Raman transitions (see Section 3.2). We note that the coordinate system is chosen here in order to present the experiment to the reader in the simplest way; in this case, the \hat{z} axis does not correspond to the quantization axis, which is defined by the direction of the magnetic field.

A laser field at 729 nm, also shared with the three experiments above mentioned, is used to manipulate a qubit defined between two Zeeman sublevels of the $3^2D_{5/2}$ and $4^2S_{1/2}$ manifolds of the $^{40}\text{Ca}^+$ ion. In our setup we have three 729 nm laser paths aligned such that they reach

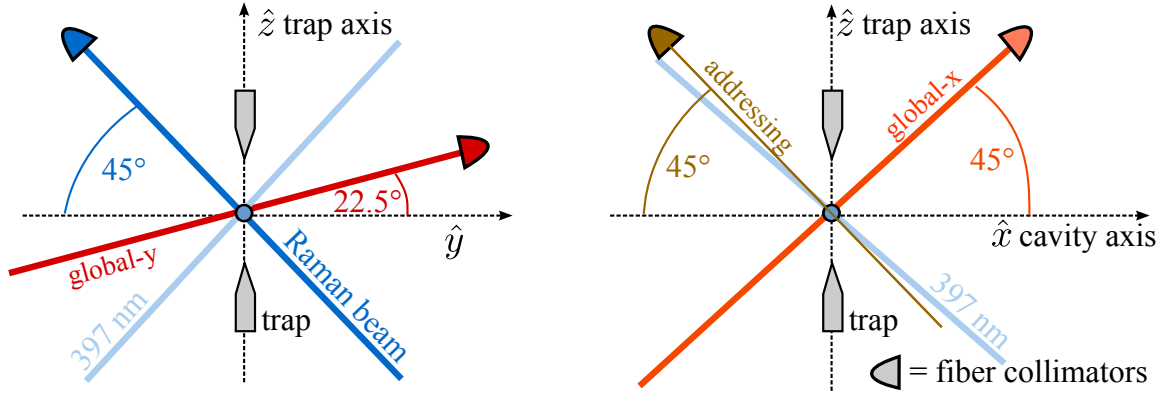


Figure 6: Alignment of the 729 nm “global-x”, “global-y”, “addressing” beams and of the 393 nm Raman beam with respect to the trap (represented by the trap endcaps) and the cavity axes. The 397 nm beams are introduced in Section 5.4.

the ions coming from different directions. These beams are labeled “global-x”, “global-y” and “addressing”. In principle, having only one addressing beam and only one global beam is sufficient for performing any arbitrary qubit operation. But two global beams have been installed to allow, in combination with the addressing beam, micromotion compensation in all three directions [76]. The label “global” means that the beam is intended to have the same intensity at the position of the ions along the trap axis. In contrast the “addressing” beam is intended to be focused such that it interacts with only one of the ions. See Section 5.5 for measurements of the intensities of the beams at the ions’ positions.

As indicated in Fig. 6, the global-x beam is directed to the ion from the $(\hat{x} + \hat{z})$ direction, while the global-y beam is directed to the ion from the $(\hat{y} + \arcsin(25^\circ) \cdot \hat{z})$ direction. The addressing beam is directed to the ion from $(-\hat{x} + \hat{z})$. The addressing beam port is discussed in Section 4.3.2.

We have modified the 729 nm optical path such that it is now possible to perform both global and addressing pulses of monochromatic or bichromatic 729 nm light in a single experimental sequence, as is now discussed.

4.3.1 The improved 729 nm optical path

In our setup, quadrupole transitions between the $3^2D_{5/2}$ and $4^2S_{1/2}$ manifolds are driven by an optical field at 729 nm. The light field is produced by a titanium-sapphire laser, or Ti:sapphire, which sits on an optical table, here referred as “the laser table”. The frequency of this laser is stabilized in the hertz regime by means of a high-finesse optical cavity. A full description of the 729 nm laser system (Ti:sapphire and high-finesse cavity) can be found in the doctoral thesis of Michael Chwalla [62].

As mentioned before, the 729 nm laser light produced by the Ti:sapphire is shared between four experiments. The Ti:sapphire produces close to 600 mW of light. From this light, 500 mW

is used by the LinTrap experiment, 70 mW is used for the frequency stabilization of the laser, and 30 mW is used as a “source” for the other three experiments.

The source light is amplified twice using tapered amplifiers (Toptica BoosTA) before being used in our experiment. From the first BoosTA, which is fed by the 30 mW source, almost 500 mW of light in a non-Gaussian mode is generated. The mode of the light is cleaned by means of a single mode optical fiber, and as a result, 170 mW of light in a Gaussian mode are available. From this light, 70 mW are used in our experiment and 100 mW are shared between the Fiber Cavity and the Segmented Trap experiments.

Fig. 7 shows a schematic representation of the 729 nm setup that has been built to transfer the light to our setup. From the laser table, the light is sent to the experiment table using a 15 meter optical fiber. On the laser table an acousto optic modulator (AOM-1) operated at -80 MHz is used for intensity stabilization and to cancel acoustic noise introduced by the fiber which transfers the light between the tables.

The intensity fluctuations are generated by fluctuations of the polarization that occur when the light travels through the optical fiber from the laser table to the experimental table. Polarization fluctuations are translated to intensity fluctuations by means of a PBS at the output of the fiber (not shown in Fig. 7). Part of the intensity of the light after the PBS is measured and stabilized via active feedback to the power of radiofrequency used to feed AOM-1. Additionally, active feedback on the frequency of AOM-1 is used to compensate the acoustic noise introduced by the fiber, which is usually in the kilohertz regime. In order to cancel the noise we follow the technique described in Ref. [92], and a detailed description of the implementation in our setup can be found in Ref. [44].

On the experiment table, 20 mW of light are amplified by means of a second tapered amplifier. This tapered amplifier has been ordered with fiber docks at both the input and the output ports. At the output of the second tapered amplifier, there are 200 mW of light available in a Gaussian mode. The light then passes through an acousto-optic modulator (AOM-D), operated at around -270 MHz in a double-pass configuration. The shifted light from AOM-D is directed to an acousto-optic modulator (AOM-2) which is operated at $+80$ MHz. Using a mechanical flip mirror, the shifted light can be directed to either the addressing or the global-y fiber couplers. The non-shifted light from AOM-2 is sent to another acousto-optic modulator (AOM-3), which is also operated at around $+80$ MHz. The shifted light from AOM-3 is sent to the global-x fiber coupler. At the input of each fiber coupler, there are 30 mW of light available.

AOM-D is used to shift the frequency of the beams to allow the transitions between Zeeman sublevels in the $3^2D_{5/2} - 4^2S_{1/2}$ manifolds to be addressed. The maximum magnetic field strength used in experiments described in this thesis is 4.6 G, which corresponds to a frequency spread of 50 MHz. AOM-3 is used to perform bichromatic pulses as required, for example, during the Mølmer-Sørensen gate operation (Section 5.8). It is important to position the global-x fiber coupler close to AOM-3; otherwise, both frequency components of the light cannot be

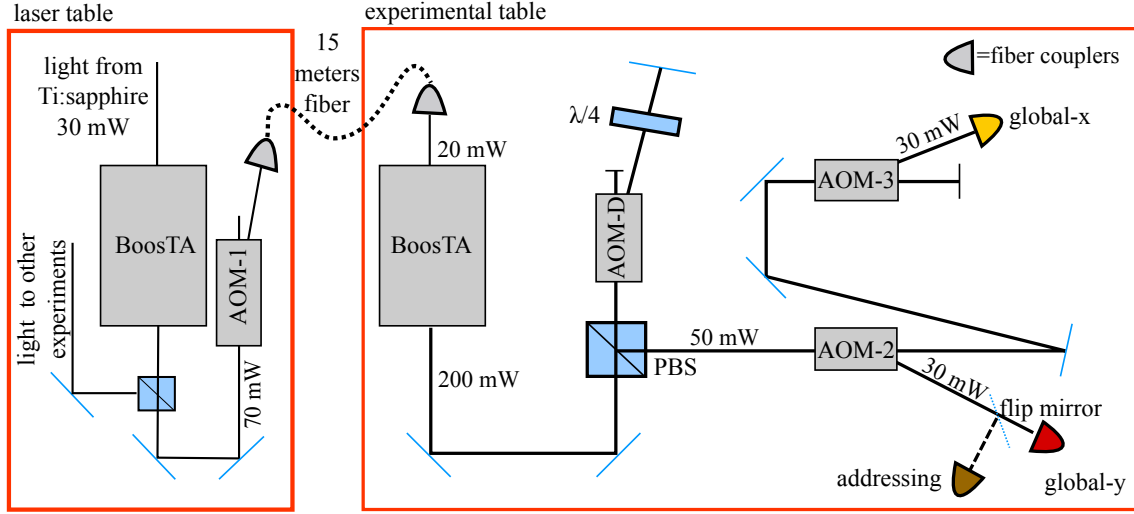


Figure 7: Schematic representation of the 729 nm setup that has been built to transfer the light from the laser table to the experimental table. Two tapered amplifiers (Toptica BoosTA) are used in order to amplify the light generated by a Ti:sapphire. AOM-1 is used for intensity stabilization and to cancel acoustic noise introduced by the fiber which transfers the light between the tables. AOM-D is used to shift the frequency of the beams to allow the transitions between Zeeman sublevels in the $3^2D_{5/2} - 4^2S_{1/2}$ manifolds to be addressed. AOM-2 is used to switch the light between the addressing/global-y and the global-x ports. AOM-3 is used to perform bichromatic 729 nm pulses.

coupled efficiently to the fiber since the two frequency components leave AOM-3 at slightly different angles.

The three fiber couplers couple the beams to two-meter long polarization-maintaining fibers. At the output of the fibers, there are 20 mW of 729 nm light. The fibers are connected to fiber collimators model 60FC-T-4-M75, which are produced by Schäfter+Kirchhoff, installed around the ion trap as indicated in Fig. 6. For the global-x and -y beams, the light is focussed using a commercial lens. For the addressing beam, the light is focussed using an objective built in house. This objective and the addressing beam setup are discussed in Section 4.3.2.

The three beams are linearly polarized. Half-waveplates installed before the vacuum chamber (not shown in Fig. 6) allow us to change the relative coupling strength on the $|S_i\rangle \leftrightarrow |D_j\rangle$ transitions for $|i - j| = 0, 1, 2$. The relative coupling depends on the angle between the polarization and the magnetic field vector projected into the plane of incidence (see Fig. 3.9 of Ref. [72]). Intensity and polarization fluctuations of the light at the ions' positions are not stabilized. We have no evidence that such fluctuations are limiting factors for the experiments presented in this thesis. The Lamb-Dicke factors of the global-x and -y beams are discussed in Section 5.8.

In the experiments described in Chapter 7, the addressing beam was not used and thus the flip mirror was set such that the global-x beam was used. In the experiments described in

Chapters 8 and 9 the addressing beam and the global-y beam were used.

4.3.2 The addressing 729 nm beam

The addressing beam setup was installed by Diana Habicher during the course of her diploma work [88]. The addressing-beam fiber coupler is mounted such that the beam is sent through an “in-house built” objective before it reaches the ions. The objective was designed as a summer project by Peter Cristofolino and was assembled in the workshop of the Institut für Experimentalphysik using a set of lenses from Lens Optics. In order to align the beam, the objective is mounted on a 3D micro-positioning stage with displacement by piezoelectric actuators which have nanometer resolution and are controlled via a serial port interface. This interface allows us to align the beam remotely from the computer controlling the experiment. A detailed description of the addressing beam system (objective, micro-positioning stage and piezoelectric actuators) can be found in Diana Habicher’s diploma thesis [88].

During her diploma work, Habicher aligned the objective such that the beam was focused close to the position at which ions are trapped. The alignment was done by moving the piezos stages iteratively to maximize the Rabi frequency of the 729 nm transition driven by the light focused through the objective. As the iterative process was carried out by hand, the alignment in all three directions required hours to days. Once the beam was aligned, the waist was measured to be $6.7 \mu\text{m}$ and $7.0 \mu\text{m}$ in the two directions orthogonal to the wave vector. Additionally, two ions were loaded in the ion trap, and it was shown that the addressing beam could be positioned so that the ratio between the Rabi frequencies of each ion due to the light focused through the objective was five.

During the course of this thesis, a piece of software was developed which automates the alignment of the addressing beam. First, a range of coordinates in all three dimensions must be specified. The software then scans the position of the addressing beam over a lattice of points spanning this range and performs a measurement at each point. During the measurement the ion state is initialized in the $|S\rangle$ state before a pulse of duration t is applied on the $|S\rangle \leftrightarrow |D\rangle$ transition (see Section 5.2). Finally the population p in the $|D\rangle$ state is measured using either the photomultiplier or the CCD camera method (see Sections 5.4 and 5.5). After the scan is finished, the software saves the population p as a function of the coordinates of the objective in all three dimensions.

Fig. 8 shows the intensity of the addressing beam at the position of the ion as a function of the coordinates of the objective. The intensity I of the addressing beam is calculated from $I \propto \Omega^2$, where Ω is the Rabi frequency of the $|S\rangle \leftrightarrow |D\rangle$ transition. The Rabi frequency Ω is calculated from the population p of the ion in the state $|D\rangle$ via

$$\sin^2(\Omega t) = p.$$

The top-left image of Fig. 8 confirms that the cross-section of the beam at the focus has a

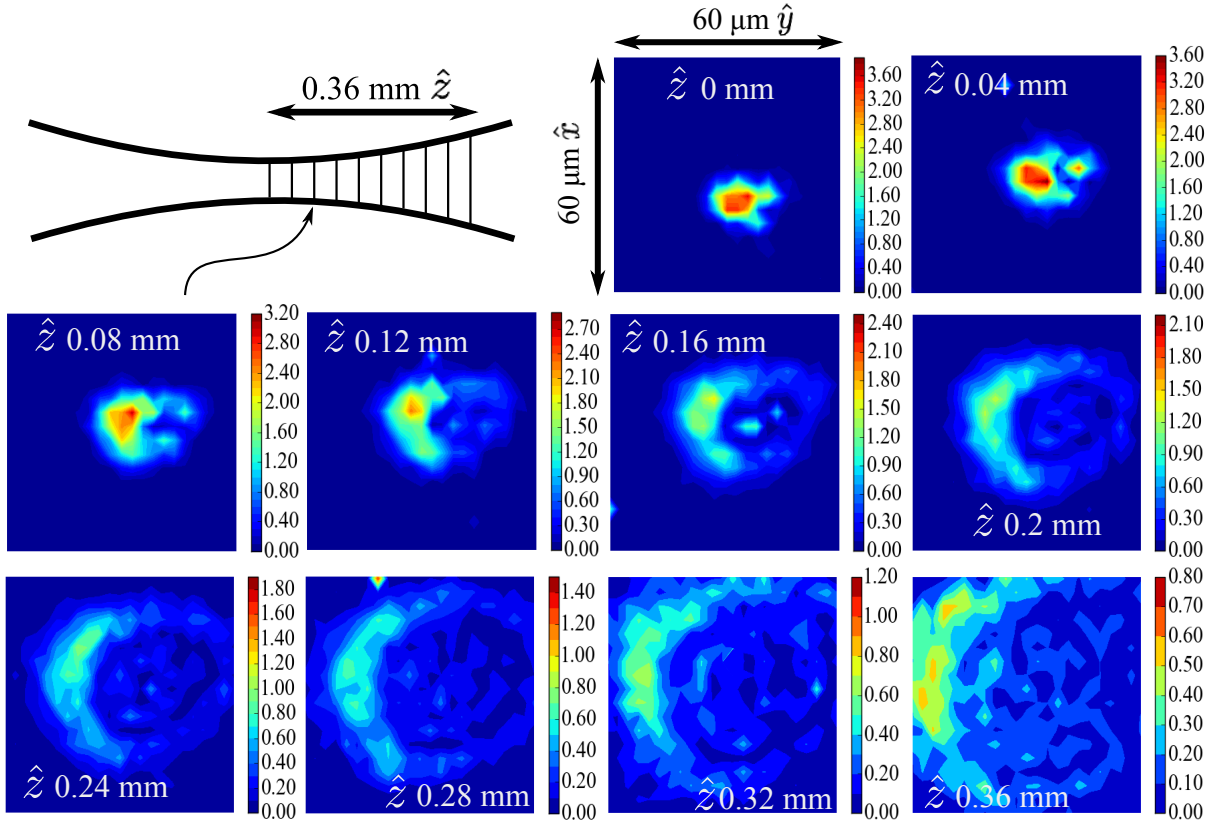


Figure 8: Intensity $I \propto \Omega^2$ of the addressing beam in arbitrary units as a function of the xyz -coordinates of the three piezoelectric actuators. The intensity is calculated from the Rabi frequency Ω of the $|S\rangle \leftrightarrow |D\rangle$ transition, which is in turn calculated from the population of the ion in the state $|D\rangle$ after a light pulse of $1\mu\text{s}$ of duration. The range of 0.36 mm in \hat{z} is panned in 10 points. The range of $60\ \mu\text{m}$ in \hat{x} and \hat{y} is panned in 20 points. The measurement took about 20 minutes.

nearly Gaussian profile. Away from the focus, the beam has aberrations and the profile does not follow the expected Airy pattern. These aberrations may originate from defects in the design or assembly process of the objective, or from misalignment of the beam — that is to say, the wave vector of the beam may not be aligned exactly parallel to the axis of the objective.

Finally we repeat the measurement of the addressing beam waist, which was originally performed by Habicher [88]. First we position the z -coordinate of the piezoelectric actuator such that the focus is at the ion position (as in the top-left image of Fig. 8). The x -coordinate is adjusted such that the population p transferred from $|S\rangle$ to $|D\rangle$ in $1\ \mu\text{s}$ is maximized. The y -coordinate is then scanned. The procedure is repeated, but with the y -coordinate fixed such that p is maximized, and the x -coordinate is scanned.

Fig. 9 shows the intensity of the addressing beam as a function of the x -coordinate of the objective for fixed yz -coordinates and as a function of the y -coordinate for fixed xz -coordinates.

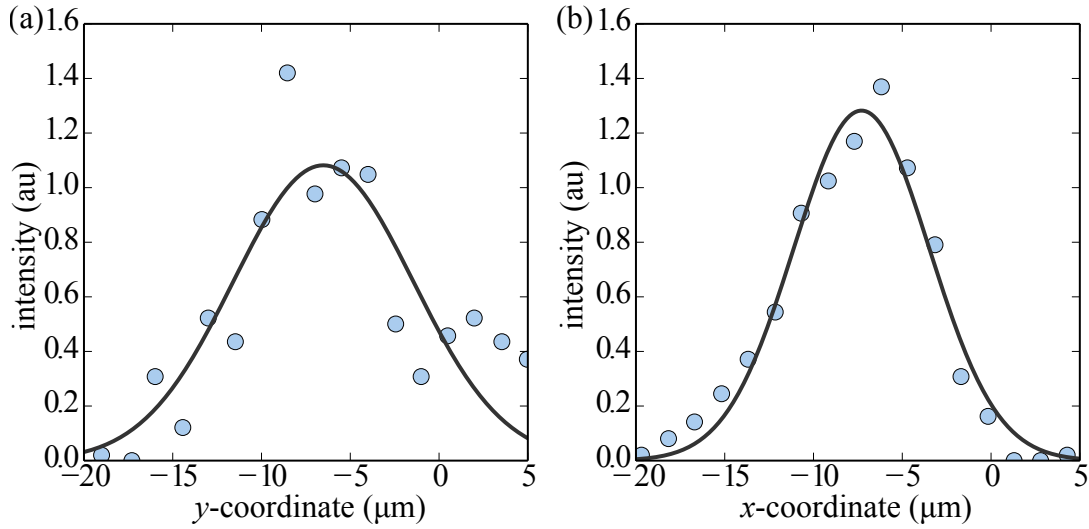


Figure 9: (a/b) Intensity of the addressing beam as a function of the x - and y -coordinates. Complementary coordinates are set such that they maximize the intensity of the beam at the position of the ion. The line corresponds to a Gaussian fit in order to extract the waist along each axis.

The intensities are calculated from the populations p as before. Ignoring the outer rings of the Airy pattern, the central lobe can be approximated as a Gaussian profile. From a Gaussian fit we extract beam waists $w_x = (3.81 \pm 0.03) \mu\text{m}$ and $w_y = (5.0 \pm 0.5) \mu\text{m}$ in the x - and y -coordinates. Despite the structure present for the y -coordinate value of $3 \mu\text{m}$, the value of w_y can be estimated within one micron. The measured values are slightly smaller than the values given in Ref. [88]. This discrepancy may be due to the improved alignment of the addressing beam for the measurement carried out in this work.

In Chapter 6, we will see that two ions can be maximally coupled to the experiment cavity for an ion–ion separation of $5 \mu\text{m}$. Such a configuration is required to perform experiments presented in Chapters 7-9. For the experiments presented in Chapters 8 and 9, it is also required to perform operations with 729 nm laser on only one of the ions. Such an operation can be performed with the addressing beam, which has a beam waist along each axis smaller than the ion–ion separation, as will be demonstrated in Section 5.9.

4.4 Detection and analysis of the polarization state of cavity photons

The experiments presented in this thesis include analysis of the polarization state of cavity photons. Polarization information is obtained by using two waveplates, a polarizing beam splitter (PBS) and two avalanche photodiodes (APDs) located at the output of the cavity (see Fig.10).

A full description of the scheme is found in Ref. [44], and summarized here. As seen in Fig.10, after photons leave the cavity, a quarter- and a half-waveplate ($\lambda/4$ and $\lambda/2$) set the polarization measurement basis. Subsequently the photons are split according to polarization

by the PBS. Two multi-mode fibers collect the light at each output port of the PBS. Photons are then sent to one of two fiber-coupled APDs. The APDs are connected to the fibers such that APD2 detects photons which are reflected by the PBS while APD1 detects photons which are transmitted through the PBS.

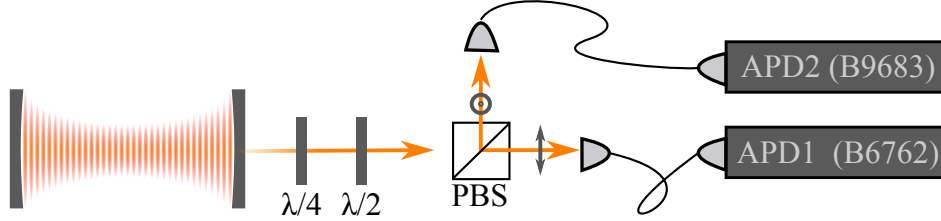


Figure 10: Analysis of the polarization state of the cavity photons. After photons leave the cavity, a quarter- and a half-waveplate ($\lambda/4$ and $\lambda/2$) set the polarization measurement basis. Subsequently the photons are split according to polarization by the PBS. Two multi-mode fibers collect the light at each output port of the PBS. Photons are then sent to two fiber-coupled APDs. The APDs are connected to the fibers such that APD2 (serial number B9683) detects photons which are reflected by the PBS while APD1 (serial number B6762) detects photons which are transmitted through the PBS.

The experiments presented in this thesis have been performed using two APDs from Laser Components, with serial numbers B9683 (APD2) and B6762 (APD1). The detection efficiencies of the APDs have been measured to be $\eta_{APD2} = (68 \pm 6)\%$ and $\eta_{APD1} = (58 \pm 7)\%$. The coupling of light into the fibers has efficiency $\eta_r = (88 \pm 3)\%$ for the light reflected off the PBS and $\eta_t = (69 \pm 2)\%$ for the light transmitted through the PBS. We have tried to increase η_t by replacing the fiber without success. We believe, however, that η_t could be increased by replacing the fiber coupler.

The detection efficiencies of the APDs were measured in October 2014. In order to perform the calibration, 10^{-8} W of light at 854 nm are sent through an optical fiber. The power at the output of the optical fiber is measured using a calibrated power meter. Using calibrated neutral density filters, the intensity of the light is attenuated by a factor of 10^{-6} . Subsequently, we connected the fiber to the APD under study. Then, we obtained the number of counts per second, and we compare the measured value with the expected number of counts. The expected number of counts is calculated by dividing the energy per photon by the total power.

In his doctoral thesis, Andres Stute reported a detection efficiency η_{APD1} of $(34 \pm 3)\%$ [76], almost half of the value reported in this thesis. When we performed the most recent measurements of η_{APD1} and η_{APD2} , we recalibrated the filters. We found that the filter internally called “cqed5” had an attenuation of $3.8 \cdot 10^{-3}$, while it had been calibrated to have an attenuation of $6.6 \cdot 10^{-3}$ at the time Stute had performed his measurement of η_{APD1} . The difference in the calibrations explains the discrepancy between the two reported values of η_{APD1} . We performed a second recalibration of the cqed5 filter, and we confirmed that the value reported in this thesis

is the correct one. The detection efficiency of APD2 was not measured by Stute because the detector had not yet then been bought.

Finally, we note that $\eta_{APD2} > \eta_{APD1}$. The reason is that the optics used in the fiber dock of APD2 was optimized for the 854 nm wavelength. The optics used in the fiber dock of APD1 was not optimized; however, such an optimization can be performed in the future by Laser Components if required.

Finally, we discuss the detection path efficiencies, that is, the probability of detecting a photon at APD1 or APD2 given that the photon was reflected or transmitted through by the PBS. The probabilities of detecting a photon at APD2 and APD1 are

$$\begin{aligned}\eta_2 &= \eta_{out} \cdot \eta_{APD2} \cdot \eta_r = (9.6 \pm 1.1)\% \\ \eta_1 &= \eta_{out} \cdot \eta_{APD1} \cdot \eta_t = (6.3 \pm 1.0)\%\end{aligned}\tag{4.1}$$

where $\eta_{out} = 20(2)\%$ is the calculated output coupling efficiency discussed in Section 4.2.

In order to determine η_{out} , we combined experimental results and simulations. After obtaining the results shown in Fig. 32 and Fig. 35, we performed simulations of the experiments. The simulations calculate the intracavity photon number, which is then multiplied by the cavity decay rate κ and the detection path efficiency η , in order to obtain the simulated detection probability shown in Fig. 32 and Fig. 35. All parameters except η are independently calibrated; therefore, η is estimated by matching the amplitude of the simulations with the measurements.

The error in the calculation of η_{out} is based on the fact that the Rabi frequency of the 393 nm field is determined with an error on the order of 20%. Varying η_{out} over a range $\pm 10\%$ allows us to match the results with simulations performed when using a Rabi frequency 20% higher than the calibrated value.

We stress that the value of $\eta_{out} = 20(2)\%$ is based on simulations, and is not a value obtained by means of a direct measurement. In order to remeasure η_{out} directly, a new calibration of the transmission coefficients of the cavity mirrors could need to be performed.

4.5 Further improvements

Currently we have the capability to implement any arbitrary qubit operation on a string of two ions. This is possible by means of the addressing and the global 729 nm beams. The main limitation lies on the addressing beam setup, which cannot be displaced during the execution of a single experimental sequence. If one wanted to work with more than two ions, arbitrary qubit operations could not be carried out since each ion would not be individually addressable.

In order to be able to address multiple ions during a single experimental sequence, we could use an acousto-optic frequency shifter (AOFS). When a beam is sent through an AOFS, the output beam is displaced depending on the power of the frequency applied to the AOFS. In general, an AOFS is designed in order to operate with beams with a diameter on the order of 1 – 2 mm. Therefore, the addressing beam should be displaced by the AOFS before the beam

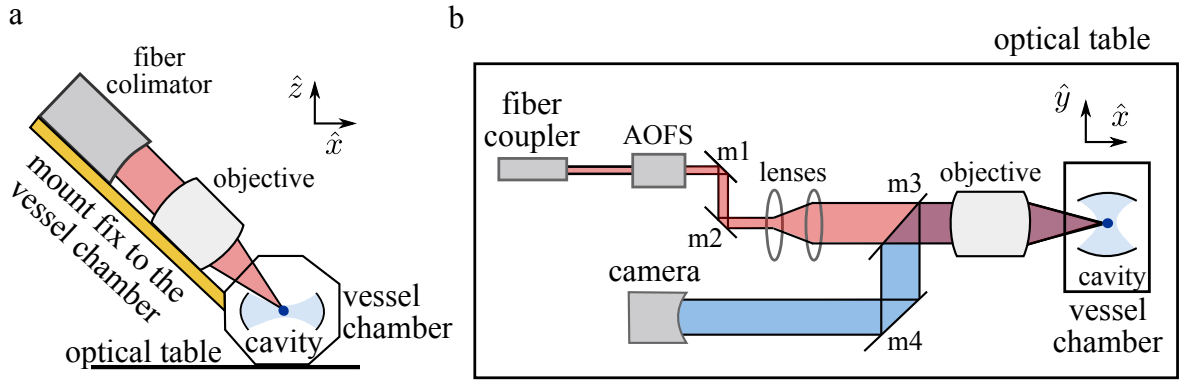


Figure 11: (a) Implementation of the addressing beam setup in our experiment. The beam is first expanded by means of a fiber collimator and then sent through the objective. Both collimator and objective are attached to a mount, which is fix to the vessel chamber. (b) Suggested implementation for a new addressing beam setup. The setup would lies in the optical table. A narrow beam is first sent through the AOFS. Subsequently, mirrors $m1$ and $m2$ direct the beam to a set of lenses in order to expand the beam. The beam then passes through the objective. Fluorescence light at 397 nm generated by the ion is collected by the objective. The collected light is reflected by the mirror $m3$, which together with mirror $m4$, directs the light to the camera.

is expanded to subsequently be sent through the objective. Fig. 11a illustrates the setup of the addressing beam in our experiment (see Fig. 5.3 of Ref. [88] for a detailed description of the setup). The beam is first expanded to a diameter of 1.5 cm by means of a fiber collimator and then sent through the objective. Both collimator and objective are attached to a mount built in house, which is fixed to the vessel chamber at an angle of 45° from the yx -plane.

In order to install the AOFS, I recommend following the solution adopted by the LinTrap experiment in our research group [93]. In the LinTrap experiment, the addressing beam is sent through the viewport which is used for the CCD camera. Therefore, the same objective is used for both focusing the addressing beam and imaging the string of ions. In such a way, the addressing beam setup sits on the optical table instead of in a mount attached to a vacuum vessel, a configuration that we have seen to be unstable. Such an implementation is described in Fig. 11b. A narrow beam with a diameter on the order of 1 millimeter is first sent through the AOFS. Subsequently, two mirrors, $m1$ and $m2$, direct the beam to a set of lenses in order to expand the beam. The beam then passes through the objective, which focuses the beam at the ion position.

In the recommended setup, the same objective is also used to collect 397 nm fluorescence light from the ion generated during a detection interval (see Section 5.5). The collected light is reflected by mirror 3 ($m3$), which together with mirror 4 ($m4$) direct the light to the camera. In this case, $m3$ should be coated such that 729 nm light is transmitted through it, and 397 nm light is reflected. The objective should be designed such that it does not produce optical aberrations for light at both 729 and 397 nm. Finally, mirrors $m1$ and $m2$ would be utilized to align the

addressing beam, mirrors $m3$ and $m4$ would be utilized to align the fluorescence light from the ion to the camera, and the AOFS would be used to displace the addressing beam during the execution of a single experimental sequence.

As we currently use an objective with the required characteristic to image the ions using the CCD Camera, I suggest offering a master's student project with the objective of performing the upgrade described in this section.

5 A toolbox for quantum computing

In the previous chapter we have introduced and characterized the relevant components and devices of our setup: the ion trap, the optical cavity and the laser fields. In this chapter we describe the implementation of general methods used for quantum information processing that make use of those devices [94] and are required to perform the experiments presented in this thesis.

In the first part of this chapter, we describe general tools for cooling the ions and initialize their state. Then, we describe a method to detect the state of the ions using a photomultiplier tube (PMT). We characterize the photon counting statistics and summarize the recent improvements to the scheme. Subsequently, we describe a more sophisticated method to detect the state of each individual ion using a charge-coupled device (CCD) camera. Then, we test the alignment of both the addressing and the global 729 nm beams using the CCD camera. Finally, in the last part of this chapter, we describe the implementation of two quantum gates: the Mølmer-Sørensen gate [60] and the AC-Stark shift gate [95]. The first gate is used to generate an entangled state of multiple ions, and the second gate is used to rotate the state of one ion. Those tools have been used to obtain the results described in Chapters 7, 8 and 9.

5.1 Doppler-Cooling and state reinitialization

When the ions are illuminated with a beam that is red-detuned from an optical transition frequency, a cooling force acts on the ion. This cooling mechanism is usually referred as Doppler cooling [51, 52, 72]. In summary, in a Doppler cooling cycle, an ion is more likely to absorb a photon from the red-detuned beam if the ion moves towards the source³. In case the ion absorbs a photon, due to energy conservation the ion decreases its kinetic energy along the direction of propagation of the beam (recoil). Subsequently, the ion decays back by emitting a photon. As the direction of emission is random, after many cycles, there is no net change in momentum of the ion due to this emission, resulting in an effective cooling force along the direction of propagation of the red-detuned beam.

This technique, however, cannot be used to cool the ion's motion to the vibrational ground state. There is a limit in the cooling force, and this limit is set by the natural linewidth of the transition used to cool [72]. In order to cool the ions' motion further, Raman cooling [96] or sideband cooling [53] techniques are in general implemented. The implementation of the sideband cooling technique in our setup is described in the next section.

In order to cool the ions using the Doppler effect, the ions are illuminated with a red-detuned 397 nm beam and with resonant 866 and 854 nm light. The 866 nm light is required to remove population from the $4^2D_{3/2}$ manifold. The 854 nm light is not required for the process; however,

³ Due to Doppler effect, in a reference system in which the emitter is still, the red-detuned beam is shifted towards the resonance frequency if the emitter moves towards the source.

it is used to remove population from the $3^2D_{5/2}$ manifold in case the previous experiment has left the ion these $3^2D_{5/2}$ states, which are dark to the Doppler cooling process.

In order to reach the Doppler cooling limit, the power and the frequency of the laser beams are carefully adjusted [76]: The Rabi frequency of the 397 nm beam is set to half of the value at saturation. This beam is red-detuned from resonance by half the linewidth. The power of the 866 nm beam is set below saturation in order to avoid power broadening, which would decrease the temperature of the Doppler limit. Finally, this beam is red-detuned by about 1 MHz in order to avoid coherent population trapping [97].

The Doppler cooling process is usually performed for approximately $500 - 1000 \mu\text{s}$. After that time, the mean phonon numbers in the axial and the radial modes have been measured to be $\bar{\eta}_a = 9.4$ and $\bar{\eta}_r = 3.5$ respectively [76].

5.2 State manipulation

In this section we demonstrate the coherent manipulation of the atomic state, and we introduce a notation that is extensively used in this thesis: “ π -pulse,” “ $\pi/2$ -pulse or -rotation” and “ $|S_i\rangle \leftrightarrow |D_i\rangle$ transition”.

In order to demonstrate the coherent manipulation between states of the $4^2S_{1/2}$ and the $3^2D_{5/2}$ manifolds, Rabi oscillations between $|S\rangle \equiv |S_{-1/2}\rangle$ and $|D\rangle \equiv |D_{-5/2}\rangle$ are shown. First, an ion is prepared in the state $|S\rangle$. Then, for a time t , we illuminate the ion with 729 nm light at a frequency $\omega = (E_S - E_D)/\hbar$, where E_S and E_D are the energy of the state $|S\rangle$ and the state $|D\rangle$. In the course of this thesis, such an operation will be referred as to drive the $|S\rangle \leftrightarrow |D\rangle$ transition. The state of the ion is then expected to be transferred according to:

$$|S\rangle \rightarrow |\psi(t)\rangle = \cos(\Omega t) |S\rangle + e^{i\phi} \sin(\Omega t) |D\rangle. \quad (5.1)$$

where ϕ is set by the phase of the 729 nm light adjusted by AOM-D (see Fig. 7) and Ω is the Rabi frequency of the beam.

Fig. 12 shows the population of the state $|D\rangle$ as function of the duration t of the pulse. The method used to calculate the population is described in the Section 5.4. From a fit, we extract the Rabi frequency Ω of the $|S\rangle \leftrightarrow |D\rangle$ transition. When the duration of the pulse is $t = \pi/2\Omega$, the process is referred as the implementation of a π -pulse. After preparing the ion in $|S\rangle$, a π -pulse on the $|S\rangle \leftrightarrow |D\rangle$ transition transfers the electronic state of the ion to $|D\rangle$ (see Fig. 12). Such an operation is also referred as a mapping; in particular, the process described above is the mapping $|S\rangle \mapsto |D\rangle$. When the duration of the pulse is $t = \pi/4\Omega$, the process is referred as the implementation of a $\pi/2$ -pulse or -rotation. After preparing the ion in $|S\rangle$, a $\pi/2$ -pulse on the $|S\rangle \leftrightarrow |D\rangle$ transition transfers the electronic state of the ion to $(|S\rangle + e^{i\phi} |D\rangle)/\sqrt{2}$ (see Fig. 12), where ϕ is the phase used to perform the rotation.

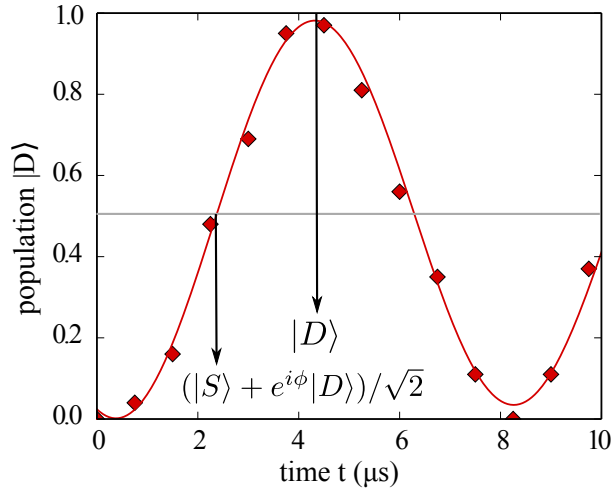


Figure 12: Population of the state $|D\rangle$ as function of the duration t of the 729 nm pulse. The ion was initially prepared in the $|S\rangle$ state. After a time $t = 2.15 \mu\text{s}$, the electronic state of the ion is in $(|S\rangle + e^{i\phi}|D\rangle)/\sqrt{2}$. After a time $t = 2.3 \mu\text{s}$, the electronic state of the ion is in $|D\rangle$. The line is a fit performed to extract the Rabi frequency of the $|S\rangle \leftrightarrow |D\rangle$ transition.

5.2.1 Preparing the state of the ions

In the experiments presented in this thesis, the ions are prepared in either $|S_{+1/2}\rangle$ or $|S_{-1/2}\rangle$ states of the $4^2S_{1/2}$ manifold. This state preparation is performed immediately after the Doppler cooling process.

To prepare the ions in $|S_{-1/2}\rangle$, we first transfer the population of $|S_{+1/2}\rangle$ to $|D_{-3/2}\rangle$ by means of a global π -pulse using the 729 nm beam. Subsequently, we repump the ions, that is, we illuminate the ions with 866 and 854 nm light for $10 \mu\text{s}$ in order to transfer the population back to the $4^2S_{1/2}$ manifold. After the repump process, the state $|S_{-1/2}\rangle$ is approximately 90% populated, while the state $|S_{+1/2}\rangle$ is approximately 10% populated. Subsequently, we again map again the state $|S_{+1/2}\rangle$ to the state $|D_{-3/2}\rangle$, followed by the repumping process. The procedure is repeated up to five times. After such a process, the ions are prepared in the state $|S_{-1/2}\rangle$ with a probability that exceeds 99.9%.

In order to initialize the ions in the state $|S_{+1/2}\rangle$, a similar procedure is performed, but the state $|S_{-1/2}\rangle$ is mapped to $|D_{+3/2}\rangle$ instead.

5.3 Sideband cooling

After ions are cooled to the Doppler limit, further cooling to the vibrational ground state can be reached by means of Raman cooling [96] or sideband cooling [53] techniques. Both techniques are based on the same principle of removing energy by addressing a so-called red-sideband transition.

The procedure is summarized as follows: Assume a two-level emitter with ground state

$|g\rangle$ and excited state $|e\rangle$, with energy difference $E_e - E_g = \hbar\omega_0$ and decay rate γ from $|e\rangle$ to $|g\rangle$. In the case that the emitter is sufficiently cold, its motional degree of freedom can be treated as a quantum mechanical harmonic oscillator with given frequency ν and phonon state $|n\rangle$. Assume a classical electromagnetic driving field with a frequency ω and that the emitter is well localized compared to the wavelength $2\pi c/\omega_0$ of the transition (Lamb Dicke regime). By writing the Hamiltonian of the system [98], one finds that if the driving field has a frequency $\omega = \omega_0$, the field drives the carrier transition

$$|g, n\rangle \leftrightarrow |e, n\rangle,$$

inverting the population of the emitter and leaving the phonon state unaltered. In the case that the driving field has a frequency $\omega = \omega_0 + \nu$, the transition

$$|g, n\rangle \leftrightarrow |e, n + 1\rangle$$

is driven. In such a case, not only the population of the emitter is inverted, but also a quantum of motion is added to the emitter. Such a transition is called a blue-sideband transition, as its frequency is increased compared to the frequency of the carrier transition. Analogously, in the case that the driving field has a frequency $\omega = \omega_0 - \nu$, the transition

$$|g, n\rangle \leftrightarrow |e, n - 1\rangle$$

is driven, and as a result, a quantum of motion is removed. Such a transition is called a red-sideband transition, as its frequency is decreased compared to the frequency of the carrier transition.

In case that $\gamma < \nu$, the sideband transitions can be addressed in frequency and sideband cooling can be performed. In a sideband cooling process, the red-sideband and the carrier transitions are alternately driven until the emitter reaches the motional ground state. In some cases, the transitions can be directly driven [53, 98] or they can be driven using a third state in a Raman scheme [96].

In our setup, we cool the ion's motion to the ground state by removing phonons on both the axial and the radial modes by driving the red sideband of the $|S_{-1/2}\rangle \leftrightarrow |D_{-5/2}\rangle$ transition. Instead of driving the red-sideband and the carrier transitions alternately as previously described, here, we use a continuous scheme. During sideband cooling in our setup, the axial or radial red sideband transition $|S_{-1/2}, n\rangle \leftrightarrow |D_{-5/2}, n - 1\rangle$ transition is driven continuously for up to 5 milliseconds, where n denotes the phonon number in the axial and in the radial modes. Simultaneously, the ions are illuminated with resonant 866 nm and 854 nm light in order to bring back the population to the state $|S_{-1/2}\rangle$. Each time that the ion is pumped from the $3^2D_{5/2}$ manifold to the $4^2S_{1/2}$ manifold, a phonon is removed.

Efficient sideband cooling is achieved using the $|S_{-1/2}\rangle \leftrightarrow |D_{-5/2}\rangle$ transition. In the case that a transition $|S_{-1/2}\rangle \leftrightarrow |D_i\rangle$ with $i \in \{-3/2, -1/2, +1/2, +3/2\}$ is used, the resonant 866 and 854 nm light might bring back the ion to the state $|S_{+1/2}\rangle$, interrupting the cooling cycle.

We implement sideband cooling in experiments in which the Mølmer–Sørensen gate operation is used; that is in the experiments presented in Chapters 8 and 9. In theory, the gate is not sensitive to the temperature of the ion; however, we have seen that after performing sideband cooling, the fidelity of the gate operation is increased by 1 – 2% compared with a situation in where the gate is operated with Doppler cooled ions. As described in Section 5.8, the Mølmer–Sørensen gate has been implemented using the axial mode. Therefore, only the axial modes have been cooled to the motional ground state. After sideband cooling, the mean phonon number in the axial mode is $\bar{\eta}_a \ll 1$. Previous measurements performed in our setup have shown that the axial mode is cooled down to a mean phonon number $\bar{\eta}_a \approx 0.022 \pm 0.001$ [76].

5.4 Ions’ state detection using a PMT

In this thesis work, we use Zeeman sublevels of the $4^2S_{1/2}$ and $3^2D_{5/2}$ manifolds of $^{40}\text{Ca}^+$ ions to perform quantum gate operations or to store quantum information. For example, in sections 5.8 and 5.9 we demonstrate the implementation of two gate operations between the states $|S_{-1/2}\rangle$ and $|D_{-1/2}\rangle$: the Mølmer–Sørensen gate and the AC-Stark shift gate. In the experiment presented in Chapter 7, we entangle the states $|D_{-5/2}\rangle$ and $|S_{-3/2}\rangle$ of two ions with the polarization degree of freedom of two photons, and in the experiment presented in Chapter 9, we use the states $|S_{1/2}\rangle$ and $|S_{-1/2}\rangle$ to store quantum information, which is subsequently transferred to a single photon.

In the experiments described above, it is necessary to detect the electronic state of the ions. Here, fluorescence detection via the electron shelving technique is used [28, 53, 63]. With this technique, it is possible to distinguish whether a state of the $4^2S_{1/2}$ manifold or a state of the $3^2D_{5/2}$ manifold is populated.

The method is as follows: During the detection interval, two lasers illuminate the ions, one at 397 nm coupling the $4^2S_{1/2}$ and $4^2P_{1/2}$ manifolds and another at 866 nm coupling the $4^2P_{1/2}$ and $3^2D_{3/2}$ manifolds. If the ion is in the “bright” $4^2S_{1/2}$ manifold, it can be excited by the 397 nm laser to the $3^2P_{1/2}$ manifold. From the $3^2P_{1/2}$ manifold, with a probability close to 16/17, the ion will spontaneously decay back to the $4^2S_{1/2}$ manifold by emitting a photon which is detected with the PMT ⁴. With probability 1/17, the ion will scatter to the $3^2D_{3/2}$ manifold, from which it will be excited back to $3^2P_{1/2}$ manifold by means of the 866 nm laser beam. In order hand, if ions are in the “dark” $3^2D_{5/2}$ manifold, only background light is recorded as the 397 nm and 866 nm lasers do not couple the $3^2D_{5/2}$ manifold. A schematic representation of the process is shown in Fig. 13. A detailed description and characterization of the PMT, the 397 nm and 866 nm lasers can be found in Ref. [29].

⁴ The probability is calculated from the decay rates indicated in Fig. 1

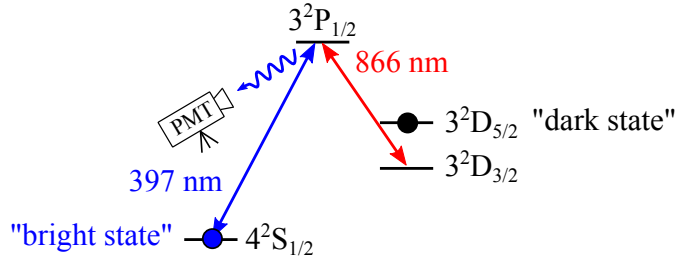


Figure 13: Relevant level scheme of the electronic states of $^{40}\text{Ca}^+$ involved in fluorescence detection. Two lasers at 397 nm and 866 nm illuminate the ion. If the ion is in the “bright” $4^2S_{1/2}$ state, photons at 397 nm are scattered and detected with a photomultiplier (PMT). If the ion is in the “dark” $3^2D_{5/2}$ state, only background light is recorded.

The goal of each fluorescence detection is to identify the number n of ions in the $4^2S_{1/2}$ manifold as well as the error of this identification given a number s of detected counts by the PMT. Ideally, the histogram of detected counts per fluorescence detection is described by a Poissonian distribution

$$p_n(s) = \frac{(nd)^s}{s!} e^{-(nd)}, \quad (5.2)$$

where d is the mean number of photons that a single ion scatters during the detection interval. After a calibration of d , one should find the value of $i \in \{0, 1, 2, 3, \dots\}$ that maximizes $p_i(s)$ and assign $n = i$.

In our setup, efficient Doppler cooling of the ions was achieved with two laser beams at 397 nm directed to the ions from the $(\hat{x} - \hat{z})$ and the $(-\hat{y} - \hat{z})$ directions (see Fig. 6). The two beams have been installed since one beam is not sufficient to address both radial motional modes effectively [76]. These two beams are also used for fluorescence detection. However, it was seen while acquiring data for the experiments of Chapter 7 that interference between these two fields at the ions’ position leads to fluctuations in the fluorescence, such that d is no longer constant in time. Thus, the statistics of the detected counts do not take the form of a Poissonian distribution.

Instead, for n ions in the $4^2S_{1/2}$ manifold, the statistics of detected counts per fluorescence detection is well described by a Gaussian distribution [72]

$$g_n(s) = \frac{1}{\sigma_n \sqrt{2\pi}} \cdot e^{-(s-s_n)^2/2\sigma_n^2}, \quad (5.3)$$

in which a single fluorescence detection results in s counts, and σ_n and s_n represent the variance and the mean value of the distribution. This follows from the central limit theorem, given the assumption that the fluctuations of μ_n are Gaussian. Given a number s of detected counts, the process to identify the number n of ions in the $4^2S_{1/2}$ manifold is analogous to the one above described but using the Gaussian distributions $g_n(s)$ instead of Poissonian distributions $p_n(s)$.

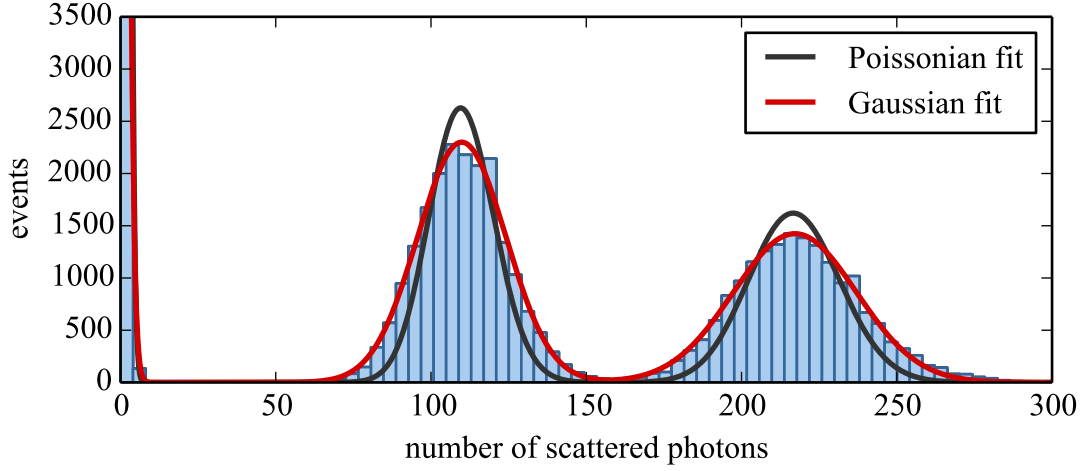


Figure 14: Histogram of the number of photons that two ions scattered in 2 ms of fluorescence detection. Fluorescence detection has been performed using two 397 nm beams (setup configuration before April 5, 2013). Fits using both a sum of three Gaussian distributions and a sum of three Poissonian distributions are shown.

In order to find s_n and σ_n , a calibration is performed. After optical pumping to the $|S\rangle \equiv |S_{-1/2}\rangle$ state, we apply a global $\pi/2$ -rotation on the $|S\rangle \leftrightarrow |D\rangle \equiv |D_{-5/2}\rangle$ optical transition to prepare the state

$$\frac{1}{\sqrt{4}}(|SS\rangle + |DD\rangle + |SD\rangle + |DS\rangle).$$

Finally, fluorescence detection is implemented.

Fig. 14 shows a typical histogram of the number of photons scattered by two ions in 2 ms of fluorescence detection. We perform a fit using a sum of three Gaussian distributions (Eq. 5.3) extracting s_n and σ_n for $n \in \{0, 1, 2\}$. The extracted values are:

	0	1	2
s	8	106	212
σ	20	405	790

Table 1: Variances s_n and mean values σ_n for $n \in \{0, 1, 2\}$ for the Gaussian distribution shown in Fig. 14.

For comparison, we also perform a fit using a sum of three Poissonian distributions. From the fit we extract the mean number of photons that a single ion scatters in 2 ms; $d = 110$. Fig. 14 shows that the distribution of recorded counts is similar to but broader than a distribution described by a Poissonian statistics.

Calculating the ions' state populations

A set of measurements for experiments with two ions consists of η_0 events in which none of the ions were in $|S\rangle$, η_1 events corresponding to one of the ions in $|S\rangle$ and η_2 events corresponding to both ions in $|S\rangle$. Using the PMT method we discriminate between three populations or probabilities: p_0 is the population of the $|DD\rangle$; p_1 is the population of $|SD\rangle$ or $|DS\rangle$; and p_2 is the population of $|SS\rangle$. The probabilities p_0, p_1 , and p_2 are then calculated as

$$p_i = \frac{\eta_i}{\sum_j \eta_j}, \quad (5.4)$$

The uncertainty δp_i associated with p_i has two components:

$$\delta p_i = \delta p_{\text{stat}} + \delta p_{\text{proj}}.$$

The first component, δp_{stat} , is the result of propagating the errors δ from all η_i events. Following Ref. [99], the associated error δ is calculated as

$$\delta = \frac{\sum_{j \neq i} g_j(s)}{\sum_j g_j(s)}. \quad (5.5)$$

The second component corresponds to the quantum projection noise [100]

$$\delta p_{\text{proj}} = \sqrt{\frac{(1 - p_i)p_i}{\eta_i}}$$

for $p_i \neq 0, 1$ and

$$\delta p_{\text{proj}} = \sqrt{\eta_i}$$

otherwise.

Improvements in the detection scheme

Above, I have mentioned that there are intensity fluctuations of the ion fluorescence due to interference between the two beams for Doppler cooling and ion state detection. The main problem that these fluctuations present is that the distribution probabilities associated with n ions in the $4^2S_{1/2}$ manifold become broader. This broadening leads to a non-negligible overlap between the distributions.

This situation is illustrated as follows: After preparing the ions in the state

$$\frac{1}{\sqrt{4}}(|SS\rangle + |DD\rangle + |SD\rangle + |DS\rangle),$$

1 ms of fluorescence detection is implemented. Fig. 15 shows the histogram of the number of photons scattered by two ions during fluorescence detection.

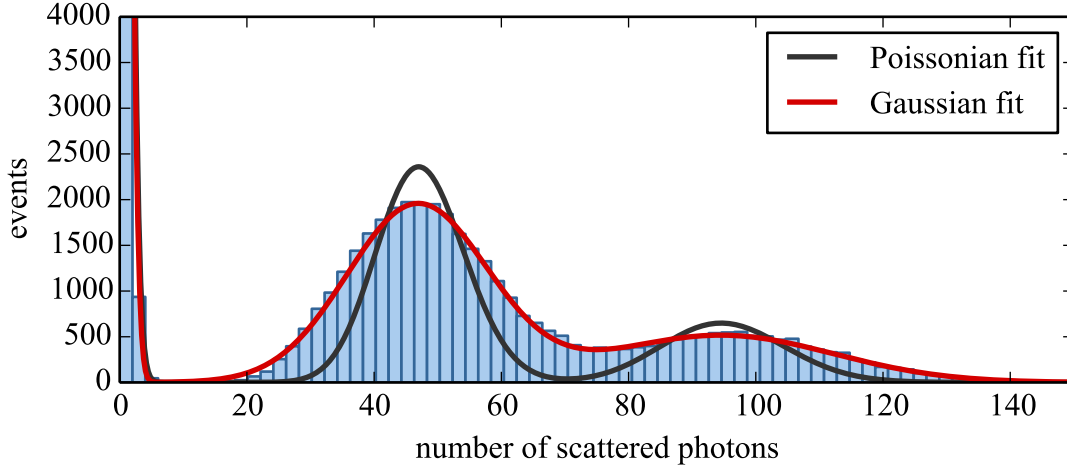


Figure 15: Histogram of the number of photons that two ions scattered in 1 ms of fluorescence detection. Fluorescence detection has been performed using two 397 nm beams (setup configuration before April 5, 2013). Fits using both a sum of three Gaussians distributions and a sum of three Poissonian distributions are shown.

The parameters that describe the three fitted Gaussians are:

	0	1	2
s	1	43	88
σ	2	220	745

Table 2: Variances s_n and mean values σ_n for $n \in \{0, 1, 2\}$ for the Gaussian distributions shown in Fig. 15.

Assuming that in a particular measurement 70 counts are recorded, the values of the Gaussian distributions $g_i(70)$ are:

$$g_0(70) = 10^{-300} \quad g_1(70) = 7 \cdot 10^{-4} \quad g_2(70) = 2 \cdot 10^{-4}.$$

The event is assigned to one ion being in $|D\rangle$ as $g_1(70) > g_2(70) > g_0(70)$, but the associated error calculated using Eq. 5.5 is 20%. The data shown in Fig. 15 have been measured under the same conditions as the data in Fig. 14, but with half the detection time. The overlap between $g_1(s)$ and $g_2(s)$ is smaller in the data shown in Fig. 14 than in the data of Fig. 15. Thus, we see that a simple solution to reduce the error is to detect for a longer time. A longer detection time, however significantly decreases the repetition rate of the experiment.

Following the measurements presented in Chapter 7, we modified the setup such that while the two 397 nm beams are used to Doppler cool the ions, only one beam is used for fluorescence detection. The modified 397 nm beam path is shown in Fig. 16. A 397 nm beam which is -80 MHz detuned from the ion's resonance frequency is brought from the laser table to the

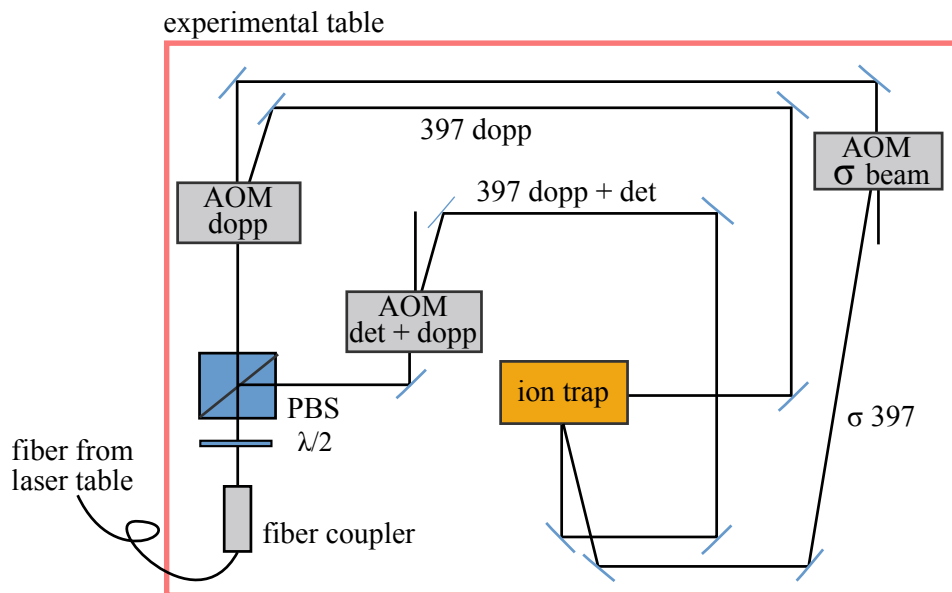


Figure 16: Modified 397 nm optical path on the experimental table. The 397 nm light is brought from the laser table to the experimental table using an optical fiber. After the fiber coupler, the light is divided and directed to two AOMs using a half-waveplate ($\lambda/2$) and a PBS. The “AOM dopp” is switched on during Doppler cooling, and “AOM det+dopp” is switched on during both detection and Doppler cooling. The “AOM σ -beam” uses the zeroth-order of the “AOM dopp”. The σ -beam is only utilized to align the magnetic field direction and remains off during the experiment.

experimental table using a polarization-maintaining fiber. At the experimental table, the light is split according to polarization by means of a polarizing beam splitter (PBS). The amount of light at each output port of the PBS can be varied by means of a half-waveplate ($\lambda/2$) located immediately before the PBS. At each output port of the PBS, the beam is directed to an acousto-optic modulator (AOM) operated at 80 MHz. The “AOM dopp” is switched on during Doppler cooling, and “AOM det+dopp” is switched on during both detection and Doppler cooling. The “AOM σ -beam” uses the zeroth-order of the “AOM dopp”. The “397 det+dopp” is sent to the ion trap from the $(-\hat{y} - \hat{z})$ direction (the coordinate system is described in Fig. 6). The “ σ 397” is sent to the ion trap from the $(-\hat{y} + \hat{z})$ direction, and it is only used to align the magnetic field direction [76], remaining switched off during experiments.

After this modification, the fluorescence measurement was repeated with the “AOM dopp” switched off during detection. Fig. 17 shows a histogram of the number of photons scattered by two ions in 1.2 ms of fluorescence detection. In this case, a sum of three Poissonian distributions with $d = 31$ fits the data with good agreement, demonstrating that significant intensity fluctuations of the 397 nm field at the ions’ position are no longer present. Given s counts, we now use Poissonian distributions (Eq. 5.2) instead of Gaussian distributions (Eq. 5.3) to identify n , the number of ions in the $4^2S_{1/2}$ manifold.

The detection time used to record the data shown in Fig. 17 is slightly longer than the detection time of Fig. 15, but shorter than that of Fig. 14. There is still some overlap between $p_1(s)$ and $p_2(s)$ in Fig. 17, but this overlap can be reduced by slightly reducing the power sent through the “AOM dopp” branch and increasing the power sent through the “AOM det+dopp” branch. Typically, this adjustment can be performed by rotating the half-waveplate by less than one degree (see Fig. 16). The improved scheme using one 397 nm beam to perform fluorescence detection is used to measure the results presented next in this Chapter, and in Chapters 8 and 9.

5.5 Ions’ state detection using a CCD camera

In the previous section, we have seen how the electronic states of the ions are detected from the PMT signal. This method has the advantage that it is fast: the quantum detection efficiency of the PMT is relatively high (25% [29]) and the scattered light that is collected is directed to only one detector. The main disadvantage associated with this technique is that one PMT does not provide spatial resolution. Therefore, it is not possible to measure the state of the ions individually, that is, we can determine that one ion is in the $4^2S_{1/2}$ manifold and one ion is in the $3^2D_{5/2}$ manifold, but not which ion.

One way to resolve the states of a string of ions spatially, is to build an array of PMTs and redirect the light of each ion such that it is detected by one PMT [101]. Another way is to use a charge-coupled device (CCD camera) sufficiently large such that the ions can be imaged onto the sensor. The main disadvantage of using a CCD camera is that detection is slower than detection with arrays of PMTs. The camera detection method requires image post-processing,

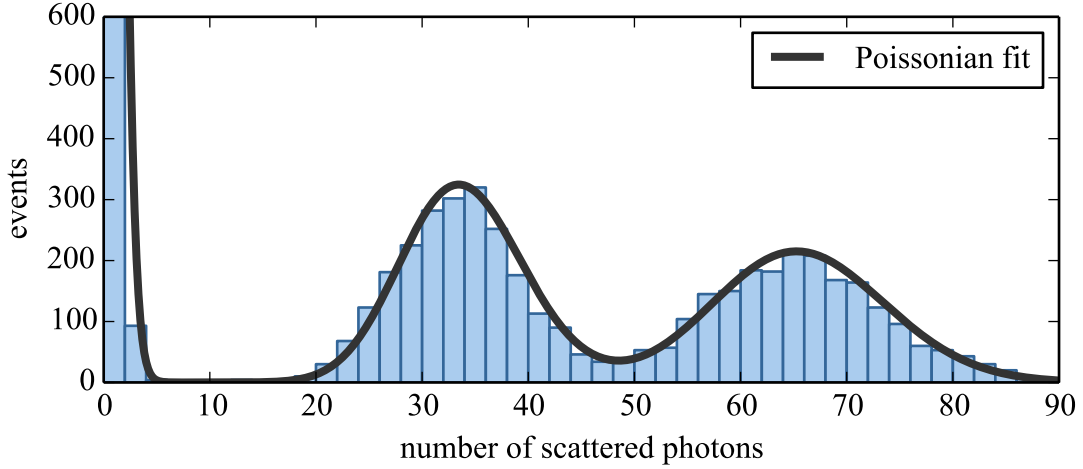


Figure 17: Histogram showing the number of photons scattered by two ions during 1.2 ms of fluorescence detection. Fluorescence detection has been performed using only one 397 nm beam, although two beams were used for Doppler cooling (current setup configuration). A fit using a sum of three Poissonian distributions is shown. For the three fitted Poissonian distributions, $d = 31$.

and unless this post-processing is implemented digitally in a field-programmable gate array (FPGA), the processing algorithm might be time consuming. Time consumption is especially high if a string of many ions is analyzed and the algorithm is implemented such that it considers cross talk between adjacent pixels.

The procedure for detection with the camera is similar to that for detection with the PMT. During the detection interval, lasers at 397 nm and 866 nm illuminate the ions. An ion in the “bright” $4^2S_{1/2}$ state scatters photons at 397 nm, a fraction of which are then detected with the CCD camera.

The CCD camera operates as an array of detectors: each array point is called a pixel. In our experiment, light from each ion is captured by an array of 3×2 pixels, typically separated each other by 3 – 5 pixels, as seen in Fig. 18a. Given a particular detection event, the procedure to determine whether an ion is in $|D\rangle$ or in $|S\rangle$ is described below.

Each pixel of the CCD has a resolution of eight bits. This means that the amount of light recorded by a single pixel V_i is scaled from a minimum value of 0 to a maximum value of 255. After an image has been recorded, our software calculates the sum

$$S_j = \sum_{i=1}^6 V_i^j \quad (5.6)$$

where the index j spans the subset of 2×3 pixels that record the light from the ion j . Subsequently, the value S_j is compared to a threshold T_j , and the state of ion j is assigned according

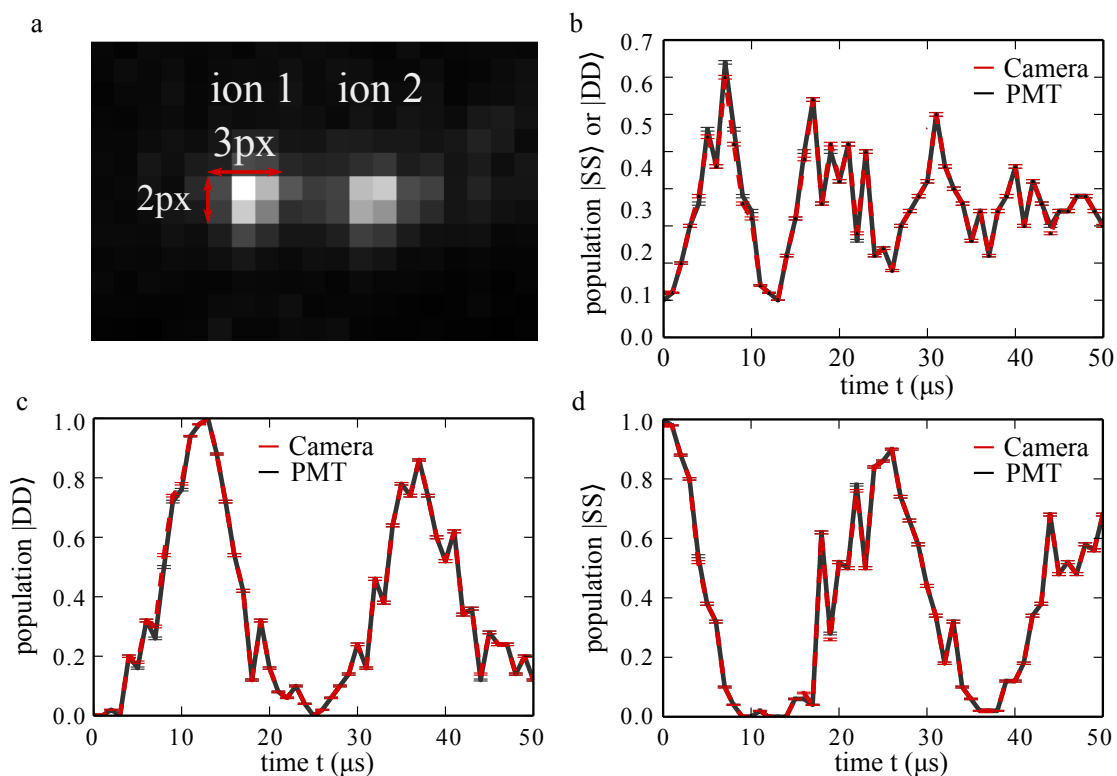


Figure 18: (a) Image of two ions recorded by our CCD camera. The light of each ion is captured by an array of 3×2 pixels. (b) Populations of $|SS\rangle$ or $|DD\rangle$, (c) $|DD\rangle$ and (d) $|SS\rangle$ calculated from both CCD and PMT detection as a function of the time t during which a global rotation on the $729 \text{ nm } |S\rangle \leftrightarrow |D\rangle$ transition is applied. Error bars are calculated according to Eq. 5.5.

to the rule:

$$\begin{aligned}
 S_j < T_j &\Rightarrow \text{ion } j \text{ in state } |D\rangle \\
 S_j \geq T_j &\Rightarrow \text{ion } j \text{ in state } |S\rangle
 \end{aligned}$$

The threshold values T_j are extracted from a prior calibration: first, ions are prepared in $|S\rangle$; next detection is performed and the “high” values S_j^M are calculated; then, a second detection is performed with the ions prepared in $|D\rangle$, from which the “low” values S_j^m are calculated; finally, T_i is calculated as

$$T_i = \frac{S_j^M - S_j^m}{2}$$

Note that the method to determine the state of each ion described in this section is different from the method described in Ref. [102]. There, the state of each ion is calculated after performing a fit to $X(i) = \sum_j V(i, j)$, where $V(i, j)$ is the intensity of the ij -pixel of the CCD image. The coordinates of the image are chosen such that the indices i and j describe the axial and the radial directions of the trap.

Calculating the ions' state populations

As in the PMT method, the ions' state populations are extracted from a set of measurements. Here, a set consists of η_D^j events in which the ion j was in $|D\rangle$ and η_S^j events in which the ion j was in $|S\rangle$. The probabilities p_j^S and p_j^D of the ion j being in states $|S\rangle$ and $|D\rangle$ respectively are then calculated as

$$p_j^S = \frac{\eta_j^S}{\eta_j^S + \eta_j^D} \quad , \quad p_j^D = \frac{\eta_j^D}{\eta_j^S + \eta_j^D}. \quad (5.7)$$

The uncertainties δp_j^S and δp_j^D associated with p_j^S and p_j^D correspond to quantum projection noise [100]

$$\delta p_j^S = \sqrt{\frac{(1 - p_j^S)p_j^S}{\eta_j^S + \eta_j^D}} \quad , \quad \delta p_j^D = \sqrt{\frac{(1 - p_j^D)p_j^D}{\eta_j^S + \eta_j^D}} \quad (5.8)$$

for $p_j^S \neq 0, 1$ and $p_j^D \neq 0, 1$ and

$$\delta p_j^S = \delta p_j^D = \sqrt{\eta_j^S + \eta_j^D}$$

otherwise.

5.6 Comparing the CCD and the PMT ions' state detection methods

In order to verify the correct functionality of the CCD method, we compare the results of the PMT method with the results of the CCD method. To perform the comparison, we load two ions in the ion trap. After Doppler cooling, the ions are prepared in the state $|SS\rangle$. Subsequently, during a time t we apply a rotation on the $|S\rangle \leftrightarrow |D\rangle$ transition using the global 729 nm beam. Finally, the state of the ions is simultaneously detected for 5 ms using both the CCD method (Eq. 5.7) and the PMT method (Eq. 5.4).

As described in Section 5.4, the PMT method allows us to discriminate between three populations: p_0 is the population of $|DD\rangle$; p_1 is the population of $|SD\rangle$ or $|DS\rangle$; and p_2 is the population of $|SS\rangle$. These populations are probabilities conditioned on the state of the two ions. The CCD method (Eq. 5.7), in contrast, provides the individual populations of each ion. The populations obtained with the CCD camera are unconditioned probabilities. Using the CCD method, the conditioned probabilities p_0, p_1 and p_2 are calculated as:

$$p_0 = \frac{\eta^{DD}}{\eta} \quad p_1 = \frac{\eta^{SD} + \eta^{DS}}{2\eta} \quad p_2 = \frac{\eta^{SS}}{\eta}$$

where η^{IJ} are the number of events where the first ion was in state $|I\rangle$ and the second in state $|J\rangle$, and η is the total number of events. Fig 18(b-d) shows the populations p_0, p_1 and p_2 calculated using both the CCD and the PMT methods as function of the time t . The calculated values of the populations using both methods are identical, within the error bars, for all t . We therefore conclude that using a long detection time of 5 ms, both methods give the same result.

We have not performed an exhaustive study to determine the detection time for which the CCD method is no longer accurate. We have however repeated the measurements presented in Fig 18(c-d) using a detection time of 2 ms, and both methods produce identical results. Thus, the detection time of 2 ms is sufficient and was used in the experiments presented in this thesis.

5.7 Testing the alignment of addressing and global 729 nm beams

In the previous section, we have described a method to detect the state of each ion using the CCD camera. In this section, we test the alignment of the addressing and the global 729 nm beams (Section 4.3.1) with respect to the position of two ions using the CCD camera.

In Section 4.3.2, we have seen that the addressing beam is focused to an area of roughly $(5 \times 4) \mu\text{m}^2$, and as the ion-ion separation is typically about $5 \mu\text{m}$, the beam can be positioned such that it interacts with only one of the ions while the other one remains decoupled. The alignment procedure is carried out with a software that has been developed in the course of this thesis. Once the beam has been positioned, we test the alignment of the beam with respect to the position of two ions.

In order to perform the test, after Doppler cooling, the ions are prepared in the state $|SS\rangle$. Subsequently, we apply a rotation on the $|S\rangle \leftrightarrow |D\rangle$ transition using the 729 nm addressing beam. Finally, the state of the ions is detected with the CCD camera. Fig 19(a) shows p_1^D and p_2^D (Eq. 5.7), the population of the states $|D\rangle$ for ions 1 and 2, as a function of the duration t of the rotation. We fit the data for each ion with a function of the form

$$e^{-\left(\frac{t^2}{2\sigma^2}\right)} \sin^2\left(\frac{\Omega_i^a t}{2}\right),$$

where σ is related to the temperature of the ions and with the atomic decoherence, Ω_i^a corresponds to the Rabi frequency of the ion i due to its interaction with the addressing beam. From this fit, we extract $\Omega_1^a = 2\pi \times 127$ kHz and $\Omega_2^a = 2\pi \times 6$ kHz. In this case, the ratio $\Omega_2^a/\Omega_1^a \approx 0.05$, confirming that the addressing beam is aligned such that it mainly interacts with the first ion. In particular, after a time $t = 4.6 \mu\text{m}$, the state $|SD\rangle$ is generated with a fidelity of 98(3)%, which is sufficient for experiments performed in this thesis work.

We now describe the procedure to test the alignment of both global 729 nm beams (see Fig. 6). The global beams are carefully broadened and positioned with the goal that the intensity of the fields are equal and near-maximum at each ion's position. Again, after Doppler cooling, the ions are prepared in the state $|SS\rangle$. Subsequently, we apply a rotation on the $|S\rangle \leftrightarrow |D\rangle$ transition using the global-x 729 nm beam. Finally, the state of the ions is detected with the CCD camera. Fig 19(b) shows the population of the state $|D\rangle$ for ions 1 and 2 as function of t . From a fit we extract $\Omega_1^g = 2\pi \times 390$ kHz and $\Omega_2^g = 2\pi \times 435$ kHz, where Ω_i^g are the Rabi frequencies of the ion i due to the interaction with the global beam. In this case, the ratio $\Omega_2^g/\Omega_1^g \approx 0.9$.

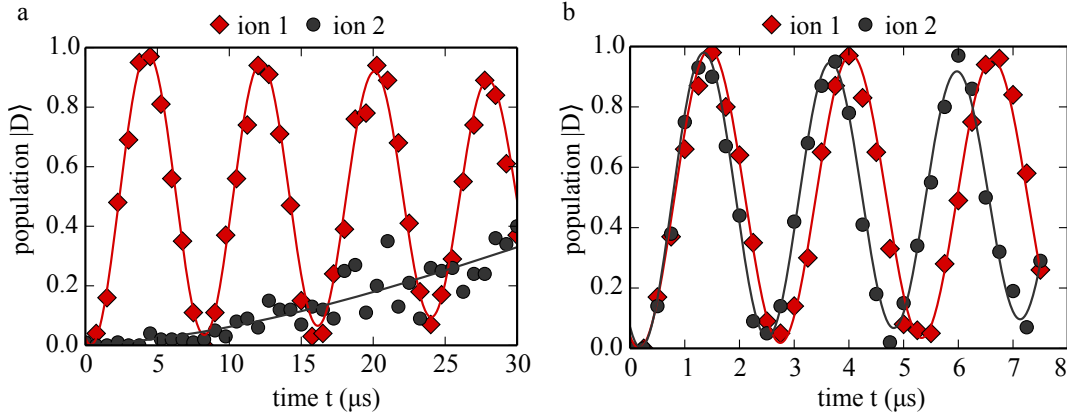


Figure 19: Population of the state $|D\rangle$ of ion 1 and ion 2 as function of the duration t of a rotation on the $|S\rangle \leftrightarrow |D\rangle$ using: (a) the addressing and (b) the global 729 nm beams. Lines are fits in order to extract the Rabi frequencies of the ions. Error bars are calculated according Eq. 5.8 and are smaller than the symbols. The scatter in (a) is attributed to intensity fluctuations of the addressing beam due to beam pointing stability.

In normal operation of the experiment, we attempt to align the global beams such that they interact equally with both ions. When the ratio Ω_2^g/Ω_1^g differs from one by more than 5%, the beam is re-aligned. In case that the ratio differs from one by exactly 5%, the error introduced in a single rotation is 0.3%. A priori, the error seems negligible, however, typical experiments consist of many global pulses; therefore, the introduced error scales exponentially with the number of pulses. The maximum number of rotations we have implemented to perform experiments in this thesis work was five. In such a case, the introduced error was close to 3.5%. It should be possible to decrease the error without a significant reduction of the Rabi frequency by slightly broadening the beam. In our setup, the global beams have a spherical profile at the ions' position. In order to simultaneously address more than two ions, I recommend to install a cylindrical lens such that the power is efficiently distributed along the string of ions.

5.8 Mølmer-Sørensen gate

Entanglement between two ions is required as a resource to perform the experiments presented in Chapters 8 and 9. We generate this entanglement by means of the Mølmer-Sørensen gate operation [60].

The Mølmer-Sørensen gate is used to entangle the electronic state of a string of ions located in the same trap. The gate can be operated with a high repetition rate, that is, within a few tens of μs [61]. For the gate operation, a bichromatic field that drives blue and red motional sidebands generates a spin-dependent force, coupling the ion's motion and internal electronic state. A main advantage of the gate is its insensitivity to the phonon state of the ions in contrast to other entangling gates [58]. Therefore, sideband cooling to the ground state [103], a process that usually lasts a few milliseconds, is not essential for high-fidelity entangling operations [94].

Consider a string of $^{40}\text{Ca}^+$ ions and two Zeeman substates $|S\rangle \equiv |S_i\rangle$ and $|D\rangle \equiv |D_j\rangle$ from the $4^2S_{1/2}$ and the $3^2D_{5/2}$ manifolds respectively, such that $|i - j| \leq 2$. During the Mølmer–Sørensen gate operation, the string of ions is illuminated by a bichromatic light field consisting of two frequencies $(v \pm \omega \mp \delta) \times 2\pi$, where ω is the frequency of a $|S\rangle \leftrightarrow |D\rangle$ transition, v is the axial or radial center-of-mass frequency and δ is the detuning from the sidebands.

If the ions are initialized in $|SS\rangle$, after a time $T = 1/\delta$, the two ions are prepared in the entangled state

$$|\Phi\rangle = (|SS\rangle + i|DD\rangle)/\sqrt{2}.$$

In order to be able to implement an entangling gate of duration T , the laser intensity needs to be set such that

$$4\eta\Omega = 2\pi \times \delta \quad (5.9)$$

where η is the Lamb-Dicke factor of the axial or radial mode, and Ω is the Rabi frequency of the $|S\rangle \leftrightarrow |D\rangle$ transition when driven on resonance [104]. The Lamb-Dicke factor

$$\eta = |\vec{k}| \cos(\theta) \sqrt{\frac{\hbar}{2Mv}}$$

describes the coupling of a field with wave vector \vec{k} to the axial or radial mode of oscillation of the string of ions, where M denotes the mass of one ion, θ is the angle between k and the direction of oscillation, and v is the frequency of this oscillation.

Let us calculate the Lamb-Dicke factor of the vibrational mode used to operate the gate. As seen in see Section 4.3, in our setup, there are two global 729 nm beams. Those beams are the global-x and the global-y, and they are installed such that they form angles of approximately 45° and 67.5° with respect to the axial direction of the trap. To implement the Mølmer–Sørensen gate, we use the axial vibrational mode. The frequency of this mode is significantly more stable than the frequencies of the radial modes, because the axial frequency is set by the trap endcap voltage, which is generated by ultra-stable high-voltage power supplies (see Section 4.1). In contrast, the radial frequencies are set by the amplitude of the oscillating voltage (RF) on the trap electrodes, which in our setup is not actively stabilized⁵. For an axial frequency of $\omega \approx 1$ MHz, the Lamb-Dicke factors of these beams are

$$\eta_y = 0.038 \quad \text{and} \quad \eta_x = 0.068. \quad (5.10)$$

The Mølmer–Sørensen gate is used in Chapter 8 and 9. For the experiment described in Chapter 8, there are no restrictions related to which $|S\rangle$ and $|D\rangle$ states can be used in order

⁵ In our setup, the RF is amplified by means of a ZHL-20W-13+ RF amplifier produced by Mini Circuits. Thermal drifts of both the vessel chamber, which lead to variations in the capacitive load of the trap, or in the the amplifier lead to fluctuations at the transmitted RF power to the blade electrodes. These fluctuations translate to drifts in the radial frequency in the kilohertz regime. The transmitted RF power can be stabilized by compensating drifts in the RF power that the trap electrodes reflect.

to perform the gate. For the experiment described in Chapter 9, an entangled state between $|S_{-1/2}\rangle$ and $|D_{-1/2}\rangle$ or between $|S_{-1/2}\rangle$ and $|D_{+1/2}\rangle$ is required. The gate is performed after sideband cooling, which is efficiently implemented using the red-sideband of the $|S_{-1/2}\rangle \leftrightarrow |D_{-5/2}\rangle$ transition (see Section 5.2). Due to selection rules, the polarization of the 729 nm beam can be adjusted to simultaneously maximize the coupling strength of transitions $|S_i\rangle \leftrightarrow |D_j\rangle$ with $|i - j| = 0, 2$ [72]. Both, the sideband cooling and the Mølmer–Sørensen gate operation require high coupling strengths on the transitions involved on these processes. Therefore, the $|S_{-1/2}\rangle \leftrightarrow |D_{-1/2}\rangle$ transition is used for the implementation of the Mølmer–Sørensen gate, and the polarization of the 729 nm beam is set accordingly to simultaneously maximize the coupling to the $|S_{-1/2}\rangle \leftrightarrow |D_{-1/2}\rangle$ and the $|S_{-1/2}\rangle \leftrightarrow |D_{-5/2}\rangle$ transitions.

During the gate operation, coherences between the states $|S\rangle$ and $|D\rangle$ are created. In our experiment, the coherence time for information stored in the $|S_{-1/2}\rangle - |D_{-1/2}\rangle$ qubit is $\tau = 475 \mu\text{s}$ [76], which is calculated following the model for the fidelity of a state in the stationary regime [93]. In such a case, the coherence is described by a Gaussian decay of the form $A_0 \exp(-\frac{t^2}{2\tau})$, where A_0 is the amplitude at time $t = 0$. To produce a maximally entangled state $|\Phi\rangle$ with a fidelity of at least 95%, the gate time T should be shorter than $150 \mu\text{s}$.

To minimize T , the global beam with a higher Lamb-Dicke parameter is used. In order to check the intensity at each ion’s position, we drive Rabi flops on the $|S\rangle \leftrightarrow |D\rangle$ transition and measure the population of $|D\rangle$ for each ion using the camera detection system (Section 5.7). In such a way, we verify that both ions are transferred from $|S\rangle \mapsto |D\rangle$ at the same time, as shown in Fig. 19b. Typical Rabi frequencies in our setup are $\Omega \approx 2\pi \times 80 \text{ kHz}$, which corresponds to a detuning δ of 21 kHz (Eqs. 5.9 and 5.10).

In Fig. 20, the populations of the states $|SS\rangle$, $|DD\rangle$, and $|SD\rangle$ or $|DS\rangle$ are shown as a function of the Mølmer–Sørensen gate duration time t for a detuning $\delta = 18.2 \text{ kHz}$. In this case, the populations are measured with the PMT and calculated as described in Section 5.4. After a time $T = 1/18.2\text{kHz} = 55 \mu\text{s}$ a maximally entangled state $|\Phi\rangle$ is generated. The solid lines in the figure indicate the ideal time evolution of the gate operation [61].

Fidelity calculation

We calculate the fidelity F_Φ of the generated state with respect to $|\Phi\rangle$ in the following way [61]: After $|\Phi\rangle$ is created, we apply an “analysis” $\pi/2$ -rotation on the $|S\rangle \leftrightarrow |D\rangle$ transition with a variable phase α with respect to the previous entangling pulse. Subsequently, the value of the parity operator [61]

$$P = p_0 + p_2 - p_1$$

is calculated from fluorescence measurements of the ion populations (Section 5.4), where p_0 and p_2 are the probabilities to find both ions in $|SS\rangle$ and $|DD\rangle$, respectively, and p_1 is the probability to find one ion in $|S\rangle$ and the other in $|D\rangle$. Fig. 20b shows the parity P as a function of the phase of the analysis rotation α . If A is the amplitude of the parity oscillation,

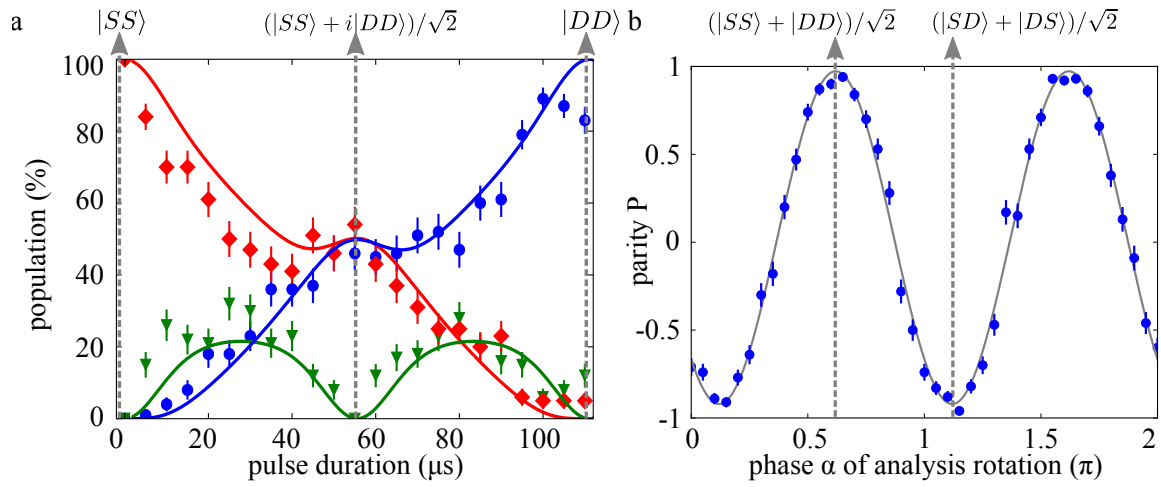


Figure 20: (a) Populations of the states $|SS\rangle$ (red diamonds), $|DD\rangle$ (blue circles), and $|SD\rangle$ or $|DS\rangle$ (green triangles) as a function of the Mølmer-Sørensen gate duration. Ions are in the state $|SS\rangle$ before the gate is applied. After $55 \mu\text{s}$ of gate duration, a maximally entangled state $|\Phi\rangle = (|SS\rangle + i|DD\rangle)/\sqrt{2}$ is created. After $110 \mu\text{s}$, the ions are in the state $|DD\rangle$. Solid lines indicate the ideal time evolution of the gate operation [61]. (b) Oscillations of the parity P of the ion populations as a function of the phase α of the analysis rotation on the $|S\rangle \leftrightarrow |D\rangle$ transition, following the creation of $|\Phi\rangle$. The dashed vertical line at phase 1.2π corresponds to $|\Psi^+\rangle = (|SD\rangle + |DS\rangle)/\sqrt{2}$. The dashed vertical line at phase 0.7π corresponds to $|\Psi^+\rangle = (|SS\rangle + |DD\rangle)/\sqrt{2}$. Error bars represent projection noise. The figure has been taken from Ref. [46].

then the fidelity F_Φ is bounded from above via $F_\Phi \geq A$. From a fit to the data of Fig. 20a, we calculate that $|\Phi\rangle$ is created with a fidelity of at least 95(2)%.

Finally, we note that the only state that satisfies $P = +1$ is the maximally entangled state

$$|\Psi^+\rangle = (|SD\rangle + |DS\rangle)\sqrt{2}.$$

From Fig. 20b, we see that P is maximized for $\alpha = 1.2\pi$. We therefore conclude that after the Mølmer-Sørensen gate operation, a $\pi/2$ -rotation with phase $\alpha = 1.2\pi$ generates the state $|\Psi^+\rangle$. In an analogous way, the only state that satisfies $P = -1$ is the maximally entangled state

$$|\Phi^+\rangle = (|SS\rangle + |DD\rangle)\sqrt{2}.$$

Therefore, a $\pi/2$ -pulse with phase $\alpha = 0.7\pi$ after the gate operation creates the state $|\Phi^+\rangle$.

In this section, we have shown that we can generate high-fidelity entanglement between two ions by means of the Mølmer-Sørensen gate operation. This entanglement is required to perform the experiments described in Chapters 8 and 9. The generation of entanglement by means of the Mølmer-Sørensen gate operation is deterministic, and the repetition rate in our experiment is close to one event every 2 milliseconds. In Chapter 7, we focus on another method to entangle two ions, namely, entanglement mediated by the optical cavity. This protocol could have also been used to generate the required entanglement for the experiments of Chapters 8 and 9, but in practice, the low repetition rate (one high-fidelity entangling event every five seconds) makes it unsuitable.

5.9 AC-Stark shift gate

In order to create an entangled state of two ions of the form $|\Psi(\phi)\rangle = (|SD\rangle + e^{i\phi}|DS\rangle)\sqrt{2}$, as required for the experiments described in Chapters 8 and 9, we introduce a phase shift in one of the ions after the creation of the state $|\Psi^+\rangle = (|SD\rangle + |SD\rangle)\sqrt{2}$. We have just seen that the state $|\Psi^+\rangle$ is created by means of the Mølmer-Sørensen gate operation followed by a global $\pi/2$ -rotation on the $|S\rangle \leftrightarrow |D\rangle$ transition with phase 1.2π .

To introduce a phase shift in one ion, we implement a so-called AC-Stark shift gate [95], which makes use of the addressing 729 nm beam. The operation of the gate is illustrated as follows: Assume that the initial state of one ion is

$$(|S\rangle + |D\rangle)/\sqrt{2}.$$

If the ion is illuminated by a laser field with Rabi frequency Ω_{AC} and detuned by δ_{AC} from the $|S\rangle \leftrightarrow |D\rangle$ transition, the ion acquires a phase $\phi(t)$ which is a function of the duration t of the pulse, such that the initial state is transferred to:

$$(|S\rangle + e^{i\phi(t)}|D\rangle)/\sqrt{2}$$

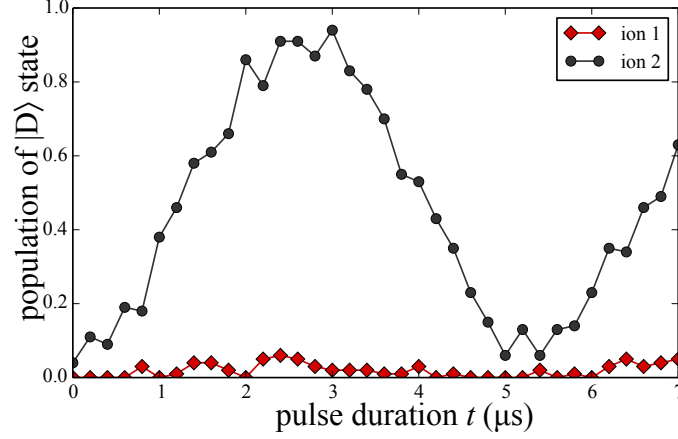


Figure 21: Population of the state $|D\rangle$ for each of two ions as a function of an AC-Stark shift pulse of duration t applied to the second ion. Both ions are initially prepared in $|SS\rangle$. Subsequently, a global $\pi/2$ -rotation on the $|S\rangle \leftrightarrow |D\rangle$ is introduced. Then, the AC-Stark shift pulse of duration t applied. Finally, a second global $\pi/2$ -rotation on the $|S\rangle \leftrightarrow |D\rangle$ is introduced. After $t = 2.6 \mu\text{s}$, the ions' state has a fidelity of 91(4)% with respect to $|SD\rangle$.

where the phase $\phi(t)$ is determined by [95]:

$$\phi(t) = \frac{\Omega_{\text{AC}}^2 t}{4\delta_{\text{AC}}}.$$

If now the initial state of two ions is $|\Psi^+\rangle = (|SD\rangle + |DS\rangle)\sqrt{2}$ and the addressing beam is positioned such that it interacts with only the first ion, after an AC-Stark shift gate of duration t , the state $|\Psi^+\rangle$ is transferred to:

$$|\Psi(\phi)\rangle = (|SD\rangle + e^{i\phi(t)} |DS\rangle)\sqrt{2}.$$

The implementation of the Stark-shift gate is demonstrated by performing an effective $|S\rangle \leftrightarrow |D\rangle$ rotation on one of the ions. After the ions are initialized to the state $|SS\rangle$, the rotation is implemented in three steps:

1. We apply a $\pi/2$ -rotation on the $|S\rangle \leftrightarrow |D\rangle$ transition using the global beam, generating the state

$$(|S\rangle + |D\rangle) \otimes (|S\rangle + |D\rangle)/\sqrt{2}.$$

2. We implement the AC-Stark shift gate for a time t :

$$(|S\rangle + e^{i\phi(t)} |D\rangle) \otimes (|S\rangle + |D\rangle)/\sqrt{2}.$$

3. A second global $\pi/2$ -rotation on the $|S\rangle \leftrightarrow |D\rangle$ transition with the same phase as the first rotation is applied:

$$(\sin(\phi(t)) |S\rangle + \cos(\phi(t)) |D\rangle) \otimes |D\rangle/\sqrt{2}. \quad (5.11)$$

Fig. 21 shows the population of the state $|D\rangle$ of each ion as a function of t measured with the CCD method (see Section 5.5). Here we have set $\delta_{AC} = 10$ MHz and $\Omega_{AC} = 8.6$ MHz. After $t = 2.6 \mu s$, the ions' state has a fidelity of 91(4)% with respect to $|SD\rangle$, thus demonstrating the operation of the AC-Stark shift gate.

The fidelity of 91(4)% is below the fidelity that we expect. The combined fidelity of the two global $\pi/2$ -rotations is 99(1)%, and the addressing beam is aligned such that the ratio between the Rabi frequencies of each ion is close to five (see Fig.19a). Under these conditions, the fidelity of the generated $|SD\rangle$ state should be mainly limited by the error introduced by the two $\pi/2$ -rotations [95]. I attribute the decrease in the fidelity to intensity fluctuations of the beam at the ions' position caused by small vibrations of the mount in which the addressing beam sits. However, such a hypothesis should be studied more in detail.

6 Tunable coupling of two ions to an optical cavity

In this chapter, we report on coupling two ions to the mode of an optical cavity and show that the interaction strength of each ion with the cavity can be controlled.

In order to demonstrate the control that this system affords in coupling multiple ions to the cavity mode, we show two ion–cavity configurations. In the first, one ion is maximally coupled to the cavity, and another ion is minimally coupled. The second configuration corresponds to both ions maximally coupled to the cavity mode. Our result constitutes a stepping stone for protocols requiring the controlled coupling of multiple ions to a single cavity [36, 105–107]. These results have been published in Ref. [45].

We emphasize two advantages of using ions in this experiment. First, the coupling strength of the ions to the optical cavity is deterministically set, and second, its value remains stable for times up to hours. Recently, two atoms have been maximally coupled to an optical cavity, but the relative sign of the interaction of the ions with respect to the cavity was randomly set by the atoms’ position during the loading process, an action that has to be repeated on a millisecond time scale [108]. The coupling strength of a single atom to the mode of an optical cavity has been controlled and kept stable for up to tens of seconds by means of active feedback, but so far the method has not been used for controlling the coupling of more than one atom [109, 110]

6.1 Setting and probing the coupling

In our setup, the control of the coupling strength of one ion to the cavity field has already been studied [42, 44], and the localization of a Doppler-cooled ion has been measured to be (13 ± 7) nm [76]. Due to the small spread of the ion’s position compared to the quarter of the wavelength of the cavity field of 854 nm, it has been possible to locate a single ion in the antinode of the standing-wave field, such that the coupling rate between the ion and the cavity has been maximized; that is, the coupling rate was not limited by the ion’s motion. This coupling has been achieved by either moving the cavity while keeping the ion’s position fixed or vice versa.

The situation is not as simple when considering two ions. In our setup, the trap axis \hat{z} along which the two ions are confined has been designed to be perpendicular to the cavity axis \hat{x} . In such a case, both ions would sit in the same standing wave node or antinode. If an equal coupling strength is desired, an ion–ion separation d smaller than the cavity waist $w \sim 13 \mu\text{m}$ is required (see Section 4.1). As illustrated in Fig. 22a, once the ions are positioned at the cavity waist, symmetrically with respect to the cavity axis, the coupling could be simultaneously varied by translating the cavity along \hat{x} . When both ions sit in the antinode, the coupling is maximum and when they sit in the node it is minimum. In the case that it is desired to couple only one of the ions, the ion–ion separation d could be increased such $d \gg w$. Varying the center-of-mass position a with respect to the trap center, one of the ions could be positioned such that it is

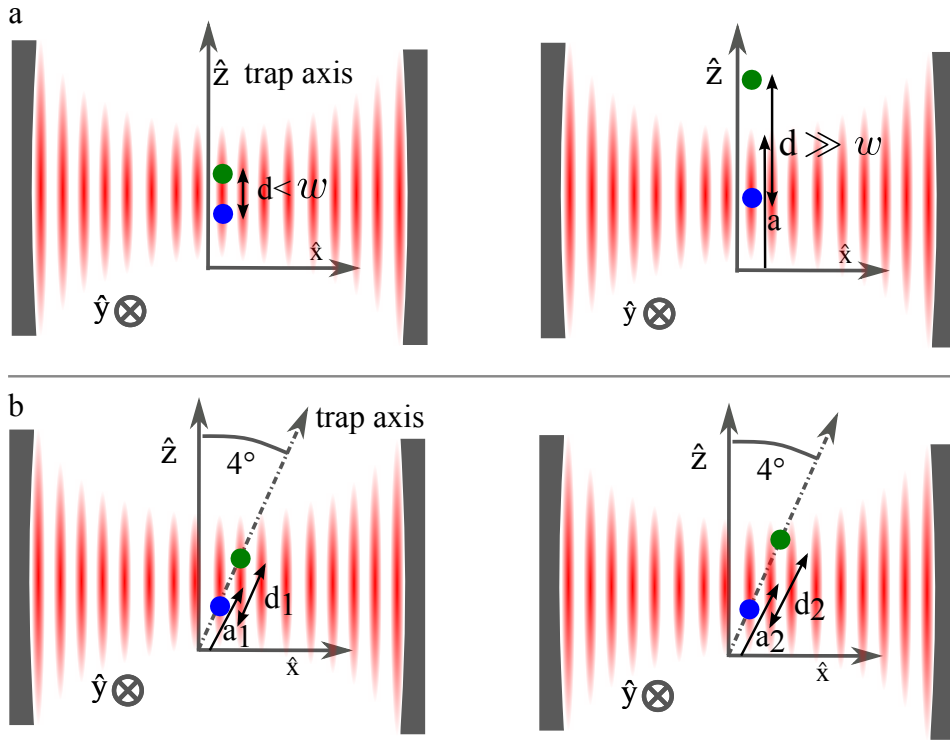


Figure 22: Side view of the setup. (a) Two trapped ions in a linear Paul trap within an optical cavity. Situation corresponding to the experimental design in which the cavity axis \hat{x} and the trap axis \hat{z} are orthogonal. Two configurations are illustrated. In the case that d is smaller than the cavity waist w , both ions can be equally coupled to the cavity mode, and the coupling can be varied by translating the cavity along \hat{x} . In the case that $d \gg w$, the center of mass position a with respect to the trap center can be set such such one ion is maximally coupled while the other remains minimally coupled. (b) Actual situation. There is a 4° -angle between the trap axis and \hat{z} . For an ion–ion separation of d_1 and a center of mass position a_1 with respect to the trap center, both ions are maximally coupled to the cavity field. For d_2 and a_2 , one ion is maximally coupled while the other remains minimally coupled.

decoupled from the cavity mode while the other remains coupled (see Fig. 22a).

Due to imperfect assembly, however, the cavity axis is not perfectly orthogonal to the trap axis, resulting in a 4° angle between the trap axis and the yz plane (Fig. 22b). Due to this small angle, the procedure to equally couple the two ions to the cavity is not as simple as described before. In this case, it is in principle possible to vary the relative coupling of the ion to the cavity by changing both the ion–ion separation d and their center-of-mass position a with respect to the trap center. Fig. 22b illustrates how by choosing appropriate values for d and a , it is possible to maximally couple both ions, or maximally couple one while the other remains completely decoupled. The ion–ion separation d and center-of-mass position a are set by the voltages applied to the trap endcaps (Fig. 23a). The relative voltage between both endcaps sets a , and the total voltage applied to both endcaps sets the ion–ion separation d . Typical values for the endcaps electrodes are shown in Section 6.3.

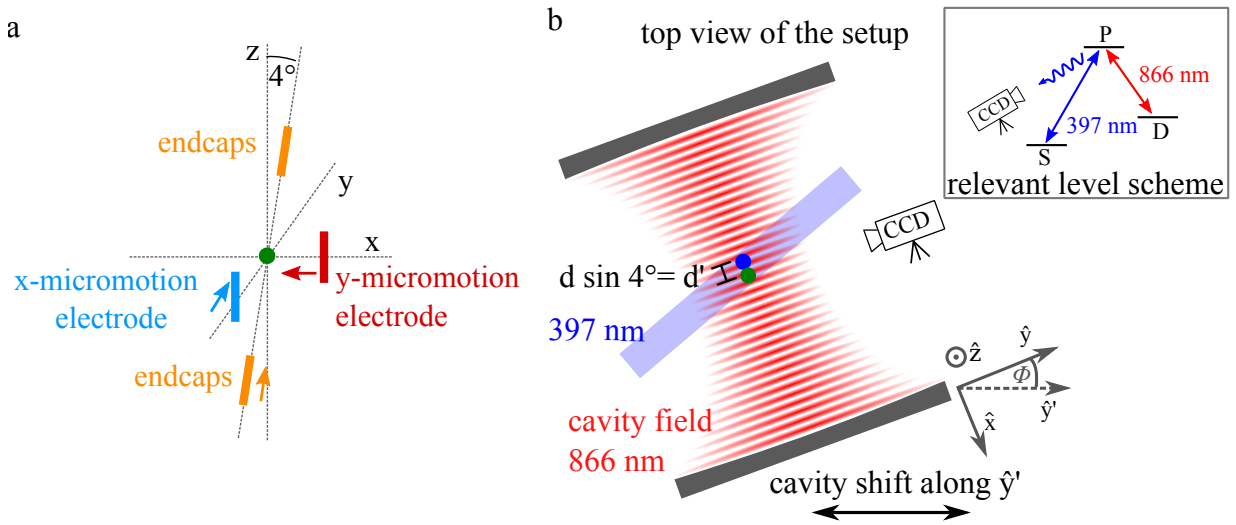


Figure 23: (a) Schematic representation of the ion trap showing the trap endcaps and the micromotion compensation electrodes. Voltages applied to the trap endcaps shift the ion’s position along the trap axis, and voltages applied to y - and x -micromotion electrodes shift the ion’s position in the xy plane. (b) A piezo stage translates the cavity along \hat{y}' , direction which is tilted at an angle $\phi \sim 5^\circ$ with respect to \hat{y} . As the piezo stage is translated, due to the small angle between \hat{y} and \hat{y}' , the coupling of each ion to the TEM_{00} mode is sinusoidally modulated. The projection of the ion–ion separation d in the xy plane is d' . The relevant level scheme of the $^{40}\text{Ca}^+$ ion involved in the measurements presented in this chapter is shown in the black inset. Levels S , P and D are short notations for $4^2S_{1/2}$, $4^2P_{1/2}$ and $3^2D_{3/2}$ respectively.

In practice, one needs to consider the ions’ micromotion. Micromotion is referred as the oscillation of the ion at the trap drive frequency that appears when the ion is not located at the minimum of the quadrupole pseudopotential that the trap generates [72, 111]. Micromotion in all three directions is compensated by adjusting the voltages on the x - and y -electrodes that shift the ion’s position in the xy -plane and the voltages applied to the trap endcaps that shift the ion’s position along the trap axis [76] (Fig. 23a and Section 4.1). Therefore, once micromotion has been compensated, it is no longer possible to change a .

To change the relative coupling between the ions without changing a , the cavity can be moved relative to the ion trap. In our setup, piezo stages allow us to shift the cavity with respect to the ions along both the cavity axis \hat{x} and the near-orthogonal axis \hat{y}' as indicated in Fig. 23b. Due to a small angle ϕ between \hat{y} and \hat{y}' (Fig. 23a), the ions interact with a Gaussian TEM_{00} mode modulated by the sinusoidal structure of the cavity standing wave as the cavity is translated along \hat{y}' [45].

Once d and a are set, a particular cavity position along \hat{y}' determines the coupling strength of both ions to the cavity field. To determine the ions’ coupling, we rely on the fact that fluorescence on the $4^2S_{1/2} \leftrightarrow 4^2P_{1/2}$ $^{40}\text{Ca}^+$ transition at 397 nm requires a repump laser (see

relevant levels in Fig. 23b). The ions are driven by a 397 nm laser from the side of the cavity and repumped by a cavity standing wave resonant with the $3^2D_{3/2} \leftrightarrow 4^2P_{1/2}$ transition, at $\lambda = 866$ nm. The standing-wave intensity is below saturation intensity, so that the fluorescence of each ion depends on the ion's position in the standing wave. A CCD camera images both ions.

6.2 Results

For a two-ion crystal of the same species, the ion-ion separation d is related to the axial trap frequency ω via [72]

$$d = \left(\frac{e^2}{4\pi\epsilon_0} \right)^{1/3} \left(\frac{2}{m\omega^2} \right)^{1/3} \quad (6.1)$$

where m is the mass of each ion. The frequency ω is determined via spectroscopy on the axial motional sideband of the $4^2S_{1/2} - 3^2D_{5/2}$ transition.

An axial trap frequency of $\omega = 2\pi \times 450$ kHz corresponds to a spacing of $d = 9.6 \mu\text{m}$ between two $^{40}\text{Ca}^+$ ions. The projection of this spacing along the cavity axis is given by $d' = d \sin 4^\circ = 670 \text{ nm} \approx 3\lambda/4$, sufficient to position one ion in a field node and the second ion in an antinode. This case is shown in Fig. 24a, in which the intensity of the cavity field seen by each ion is plotted as the cavity is shifted along \hat{y}' . A separate calibration is used to translate the measured fluorescence at 397 nm into intensity at 866 nm. By fitting a sinusoidally modulated Gaussian to the data, we extract a relative phase of 0.9π between the two ions with respect to the standing wave.

To couple two ions maximally to the cavity mode, that is, to place both ions in an antinode of the standing wave field, we increase the axial trap frequency to $\omega = 2\pi \times 1.09$ MHz, corresponding to $d = 5.3 \mu\text{m}$ and $d' \approx \lambda/2$. This separation together with an appropriate cavity position allows us to position both ions in neighboring antinodes. In the situation shown in Fig. 24b, the two ions experience almost the same field as the cavity is translated; a phase difference of 0.2π is determined from the fit. More generally, this technique can be used to select any target phase difference between these two extremes.

6.3 Experimental considerations

Ideally, it should be possible to vary d by simultaneously changing the voltage of both trap endcaps while keeping the difference between them constant. In such a way, the ions' center of mass position a should remain fixed, and micromotion would thus not be affected. But in practice, simultaneously changing the voltage of both trap endcaps affects the micromotion. On CCD camera images, it is possible to see how the ions are shifted not only in the trap axis direction, but also in the xy -plane (see 23a). The additional shift on the ions' position could be explained by a small misalignment of the endcaps with respect to the trap electrodes, that

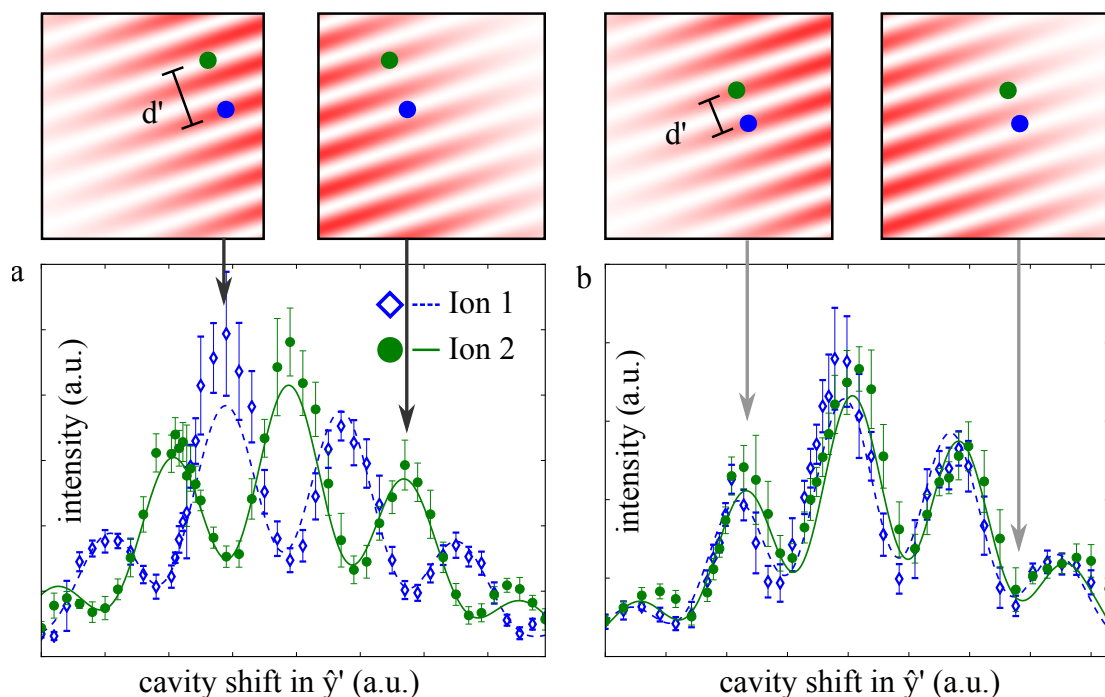


Figure 24: (a) For a projected ion–ion separation of $d' = 670$ nm, as the cavity is translated along \hat{y}' , the ions couple to the cavity with phase difference 0.9π . The cavity standing wave at 866 nm (red) is used to repump the ions, and fluorescence of the ions at 397 nm is measured on an EM-CCD. (b) For $d' = 370$ nm, the relative phase difference is 0.2π .

might introduce electrostatic fields in the xy -plane. Therefore, for any new particular choice of d , micromotion has to be re-compensated.

It might be time-consuming to re-compensate micromotion when changing d from a known compensated situation to an arbitrary new value. We have found that a first easy step to re-compensate it is to mark the ions' positions on the CCD camera image when micromotion is compensated. Then, d is changed to the target value, and the ions' positions are set close to the marked ones on the CCD camera image by adjusting the voltages of the micromotion compensation electrodes and the relative voltage between the endcaps. From this situation, a fine adjustment of the voltages applied to the compensation electrodes and the trap endcaps should be enough to re-compensate micromotion in all three directions. The fine adjustment can be implemented by minimizing the micromotion sidebands measured via spectroscopy on the $4^2S_{1/2} - 3^2D_{5/2}$ optical quadrupole transition [44]

Below, the voltages are given, that have been applied to the trap endcaps and the compensation electrodes in the two configurations described in the previous section. Internally, we call V_I and V_{II} to the voltage applied to compensation electrodes, and V_{diff} and V_{ave} to the difference and the average of the voltage applied to the endcaps.

- Both ions equally coupled ($d = 5.3 \mu\text{m}$):

$$V_I = -169.5 \text{ V}$$

$$V_{II} = 204.91 \text{ V}$$

$$V_{\text{diff}} = 30 \text{ V}$$

$$V_{\text{ave}} = 900 \text{ V}$$

- One ion coupled and the other decoupled ($d = 9.6 \mu\text{m}$):

$$V_I = -43.71 \text{ V}$$

$$V_{II} = 8.61 \text{ V}$$

$$V_{\text{diff}} = 6.71 \text{ V}$$

$$V_{\text{ave}} = 200 \text{ V}$$

6.4 Conclusions

In this chapter, we have shown how the coupling strength of two ions to the mode of an optical cavity can be controlled. In particular, we have shown a configuration in which two ions are equally and maximally coupled, a requirement to perform the experiments presented in chapters 7-9. This configuration is therefore used for the experiments presented in the remaining part of this thesis.

The technique presented in this chapter can be utilized to equally couple more than two ions. As seen before, the ion–ion separation needed to position two ions in the antinode is of the order of $5 \mu\text{m}$. In our setup, ions are trapped perpendicular to the cavity axis, therefore the length of a string of three ions is shorter than the cavity waist $w \sim 17 \mu\text{m}$. In such a case, the ions can be positioned symmetrically with respect to the cavity axis, resulting in a configuration with one ion maximally coupled to the cavity, while the coupling of the other two ions is reduced by a factor of 0.84. To estimate this reduction, we have assumed that the radial profile of the cavity mode at the waist has a Gaussian shape, which is proportional to $e^{-2(\frac{r}{w})^2}$ where r is the distance from the cavity axis. Four ions symmetrically positioned results in a configuration in which the coupling to the cavity of the inner ions is reduced by a factor of 0.94, while for the outer ones, the coupling is reduced by a factor of 0.68. Therefore, before performing an experiment with three or four ions, I recommend to estimate either analytically or by means of simulations the effect of the inhomogeneous ion–cavity coupling.

Finally we note that control of the coupling of multiple ions to the cavity mode constitutes an important step toward hybrid quantum networks, in which small ion-trap registers in cavities are linked via optical fibers [112]. The idea is schematically represented in Fig. 25. There, we show two ion-based quantum computers surrounded by two optical cavities interconnected by an optical fiber. Coupling only one of the ions to the cavity and performing a protocol like the one described in Chapter 7, it is possible to efficiently entangle the two quantum computers duplicating the available resources for quantum computation. In Ref. [14], modular entanglement has been achieved using three ions. There, high numerical aperture lenses are used to collect the

light of the ions in order to generate entanglement between the two remote quantum computers, and phonons to generate entanglement between the two ions located in the same quantum computer.

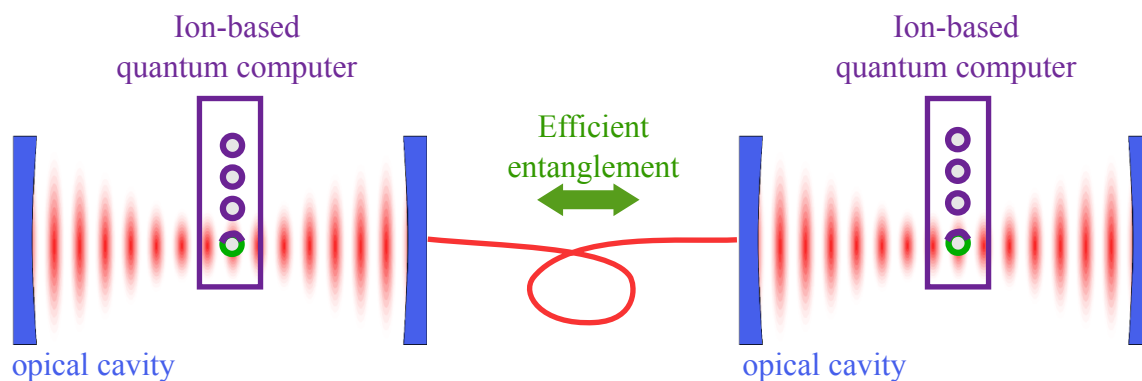


Figure 25: Proposal for the implementation of a hybrid quantum networks, in which the available resources for quantum computation are doubled. Two ion-based quantum computers surrounded by two optical cavities are interconnected by an optical fiber. Efficient entanglement of the two quantum computer can be achieved with a protocol like the one studied in Chapter 7.

7 Entanglement of two ions in an optical cavity

In the previous chapter, we have shown that we can couple two ions to the mode of an optical cavity and that the interaction strength of each ion with the cavity can be controlled. In this chapter, we present a protocol that relies on this coupling: heralded entanglement between the two ions.

For ions confined in a shared potential as in our experiment, entanglement is already possible via motional degrees of freedom by means of, e.g., the Mølmer–Sørensen gate operation, as seen in Section 5.8 and in Ref. [47]. However, in other quantum registers such as arrays of neutral atoms confined by optical dipole traps [113, 114], the absence of a common mode due to the low atom–atom coupling rate as compared to the trapping frequencies hinders the implementation of the Mølmer–Sørensen gate. In such a case, this cavity-based method that we have demonstrated represents a promising route for generating entanglement.

For remote ions confined without a shared potential, the cavity-based protocol presented here can be extended to generate entanglement between the ions in an efficient way [23, 115]. As discussed in Section 6.4, the generation of remote entanglement is a stepping stone for the implementation of distributed quantum computing [112]. These results have been published in Ref. [45].

7.1 Introduction

The generation of atom–atom entanglement via a cavity is a long-standing goal in the cavity quantum electrodynamics (CQED) community, so far only achieved by Serge Haroche’s group, first in 1997 and then in 2001 [32, 33]. In the pioneering experiments by Haroche, entanglement between two Rydberg atoms is based on the unitary evolution of the atom–cavity interaction at rate $2g$. For high-fidelity entanglement, such schemes [32, 33, 116, 117] typically require the strong-coupling regime $g \gg \{\kappa, \gamma\}$, where κ and γ are decay rates of the cavity field and the atom. More recent strategies for dissipative preparation of entanglement are less stringent but still assume a cooperativity parameter $\mathcal{C} \equiv g^2/(2\kappa\gamma)$ of more than 10 [118–120].

Here, we present the entanglement of two ions mediated by an optical cavity, following a completely different approach than those mentioned above. In our experiment, high-fidelity entanglement is achieved in a system with effective parameters $\gamma \gg g \gg \kappa$ and with a cooperativity parameter close to one.

We use a modified version of the proposal by Duan and Kimble to generate entanglement between two distant atoms [19]. In Ref. [19], the two atoms interact with two optical cavities, and entanglement between a single photon and a single atom is generated. Photons leaving the cavities interfere at a non-polarizing beam splitter. After a joint detection of orthogonally-polarized photons at each output ports of the beam splitter, as photons are indistinguishable, atoms are projected onto an entangled state. In our scheme, we use two ions interacting with

one optical cavity. The two photons that are entangled with the ions are emitted into the optical cavity in the same spatial mode; therefore, they are indistinguishable. As in the proposal described in Ref. [19], a joint detection of orthogonally-polarized photons leads to entanglement of the ions. The fidelity of the ion–ion entanglement generated by this protocol is robust against spontaneous emission and the probability of success approaches 1/2.

7.2 Description of the protocol

Our entangling scheme relies on the method for ion-photon entanglement described in more details in Refs. [30, 76]. In summary: a single $^{40}\text{Ca}^+$ ion is confined in a linear Paul trap and coupled to an optical cavity. The optical cavity at 854 nm couples the $4^2P_{3/2}$ and $3^2D_{5/2}$ manifolds. A bichromatic Raman beam at 393 nm couples the $4^2S_{1/2}$ and $3^2D_{5/2}$ manifolds. The beam is aligned parallel to a magnetic field of magnitude $B = 2.96$ G and orthogonal to the cavity axis (see Fig. 26b). The beam is circularly polarized and has two frequency components such that it simultaneously drives the cavity-mediated Raman transitions $|S\rangle \rightarrow |D\rangle$ and $|S\rangle \rightarrow |D'\rangle$ via the intermediate state $|P_{-3/2}\rangle$ as shown in Fig 26a, where $|S\rangle \equiv |S_{-1/2}\rangle$, $|D\rangle \equiv |D_{-5/2}\rangle$ and $|D'\rangle \equiv |D_{-3/2}\rangle$. Following optical pumping to $|S\rangle$, applying this Raman process to the ion results in entanglement of the ion’s electronic state with the polarization H or V of a single cavity photon at 854 nm:

$$|\psi(\theta, \phi_r)\rangle = \sin(\theta)|DH\rangle + e^{i\phi_r} \cos(\theta)|D'V\rangle, \quad (7.1)$$

where ϕ_r is determined by the relative phase between the two frequency components of the Raman beam, and the angle θ is identified as $\tan^{-1}(g_1/g_2)$, where g_1 and g_2 are the effective Rabi frequencies given by Eq. 3.13. The value for θ is an approximation valid for the case $g_i \gg \gamma_{\text{eff}}$, where γ_{eff} is given by equation Eq. 3.10 [76]. When ϕ_r is set to zero and the effective Rabi frequencies g_1 and g_2 are set such that $\theta = \pi/2$, the following maximally entangled state is created:

$$|\psi\rangle = (|DH\rangle + |D'V\rangle)/\sqrt{2}, \quad (7.2)$$

Applying the ion-photon entanglement protocol to two $^{40}\text{Ca}^+$ ions that are equally coupled to the cavity generates two photons entangled with the two ions:

$$|\Psi_{\text{tot}}\rangle = |\psi\rangle \otimes |\psi\rangle = \sqrt{1/4}(|DHDH\rangle + |D'VDH\rangle + |DHD'V\rangle + |D'VD'V\rangle). \quad (7.3)$$

The two photons exit the cavity, and H and V components are split at a polarizing beamsplitter (PBS). Finally, photons are detected using two avalanche photodiodes (APD1 and APD2) located at each output port of the PBS. If the photons are indistinguishable (Section 7.5), and one photon with horizontal (H) polarization and one with vertical (V) polarization are detected (Fig. 26b), the state $|\Psi_{\text{tot}}\rangle$ is projected onto the state

$$|\Psi_{\text{herald}}\rangle = \sqrt{1/2}(|DD'\rangle + |D'D\rangle). \quad (7.4)$$

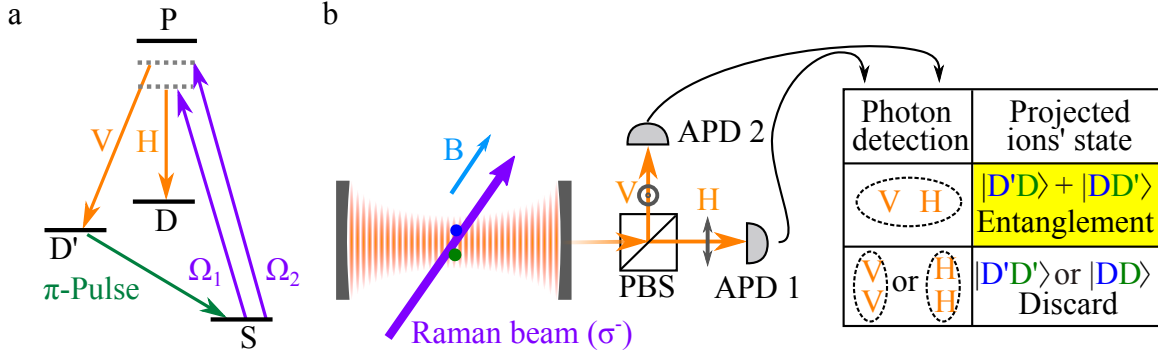


Figure 26: Schematic representation of the experiment. (a) Relevant level scheme of the $^{40}\text{Ca}^+$ ion involved in the process. Two ions are prepared in the electronic state $|S\rangle$. A Raman process, driven by a bichromatic field at 393 nm with Rabi frequencies Ω_1 and Ω_2 , detuned from the excited state $|P\rangle$, generates two cavity photons at 854 nm. The photons' polarization, either horizontal (H) or vertical (V), is entangled with the states $|D\rangle$ and $|D'\rangle$ of both ions. An optical π -pulse at 729 nm then coherently transfers population in $|D'\rangle$ to $|S\rangle$. (b) The Raman beam is parallel to a magnetic field of B and orthogonal to the cavity axis. A polarizing beam splitter (PBS) at the cavity output enables independent measurement of polarization components using avalanche photodiodes (APDs). Measurement of one H - and one V -polarized photon projects the ions into an entangled state.

The joint detection event thus heralds ion–ion entanglement [23]. In order to perform state readout of the ions via fluorescence detection (Section 5.4), we map $|\Psi_{\text{herald}}\rangle$ onto the qubit basis $\{|S\rangle, |D\rangle\}$ with a π -pulse on the $|D'\rangle \leftrightarrow |S\rangle$ optical transition at 729 nm, ideally generating the Bell state

$$|\Psi^+\rangle = \sqrt{1/2}(|DS\rangle + |SD\rangle). \quad (7.5)$$

7.3 State fidelity via parity flops ⁶

The fidelity of the experimentally generated state $|\Psi\rangle$ with respect to the target state $|\Psi^+\rangle$ can be bounded without reconstructing the full two-ion density matrix $\rho = |\Psi\rangle\langle\Psi|$ [121]. Specifically, the fidelity F_{Ψ^+} is determined from three components of ρ :

$$\begin{aligned} F_{\Psi^+} &= \langle\Psi^+|\rho|\Psi^+\rangle \\ &= (\rho_{SD,SD} + \rho_{DS,DS})/2 + \text{Re}(\rho_{SD,DS}). \end{aligned} \quad (7.6)$$

The first term represents a direct measurement of population in states $|SD\rangle$ and $|DS\rangle$. This population, equivalent to the probability that one ion is in $|S\rangle$, is determined by fluorescence detection on a photomultiplier over multiple trials (Section 5.4). More generally, the photomultiplier measurement allows us to determine p_k , the probability that k ions are in $|S\rangle$, where $p_0 + p_1 + p_2 = 1$.

⁶The text in this section and its argumentation informations follow Ref. [45]

The second term of F_{Ψ^+} represents coherences between $|SD\rangle$ and $|DS\rangle$. To estimate these coherences, we need to implement two additional measurements. First, we apply two global $\pi/2$ rotations on the $|D\rangle \leftrightarrow |S\rangle$ optical transition [61, 122]. The first rotation $\sigma_x^{(1)}\sigma_x^{(2)}$ maps $|\Psi^+\rangle$ to $|\Phi^+\rangle = \sqrt{1/2}(|SS\rangle + |DD\rangle)$, where $\sigma_j^{(i)}$ denotes a Pauli spin operator acting on ion i . The second rotation is given by $\sigma_\phi^{(1)}\sigma_\phi^{(2)}$, where $\sigma_\phi^i = \sigma_x^i \cos \phi + \sigma_y^i \sin \phi$ and ϕ is the relative phase between the pulses. The rotations are followed by a measurement of the parity P , defined as $p_0 + p_2 - p_1$. The parity oscillates as a function of ϕ and reaches a maximum for $\phi = \pi/2$ [122],

$$P(\pi/2) = 2 \operatorname{Re}(\rho_{SD,DS} - \rho_{SS,DD}), \quad (7.7)$$

where $\rho_{SS,DD}$ represents the coherence between $|SS\rangle$ and $|DD\rangle$. For the particular case in which $\rho_{SD,SD} + \rho_{DS,DS} = 1$, population $\rho_{SS,SS}$ and $\rho_{DD,DD}$ are zero, and therefore the coherence term $\rho_{SS,DD}$ is also zero. In such a case, the coherence term $\rho_{SD,DS}$ can be directly determined from Eq. 7.7.

But in general, the coherence term $\rho_{SS,DD}$ may be nonzero and a second measurement is required in order to bound $\operatorname{Re}(\rho_{SD,DS})$. After joint detection of orthogonal photons and the subsequent mapping from $|D'\rangle \mapsto |S\rangle$, the rotation $\sigma_\phi^{(1)}\sigma_\phi^{(2)}$ is implemented. The phase ϕ is defined with respect to the phase of the mapping pulse. The parity $P(\phi)$ is then measured as a function of ϕ . A function $P_{\text{fit}}(\phi) = C \sin(2\phi + \phi_0)$ is fit to the data of the resulting parity oscillation, where $C = 2|\operatorname{Re}(\rho_{SS,DD})|$ and ϕ_0 is the phase that maximizes the contrast in order to obtain a maximum bound [61].

Since

$$\operatorname{Re}(\rho_{SD,DS} - \rho_{SS,DD}) \leq \operatorname{Re}(\rho_{SD,DS}) + |\operatorname{Re}(\rho_{SS,DD})|,$$

the second term of Eq. 7.6 can now be bounded from above:

$$\operatorname{Re}(\rho_{SD,DS}) \geq \operatorname{Re}(\rho_{SD,DS} - \rho_{SS,DD}) - C/2,$$

where $\operatorname{Re}(\rho_{SD,DS} - \rho_{SS,DD})$ is determined from the parity measurement corresponding to Eq. 7.7. Thus, the fidelity F_{Ψ^+} can also be bounded from below, and this bound is given by

$$F_{\Psi^+} \geq (\rho_{SD,SD} + \rho_{DS,DS} + P(\pi/2) - C)/2.$$

7.4 Implementation of the protocol and results ⁷

To perform the protocol for heralded entanglement, two $^{40}\text{Ca}^+$ ions separated by $5.6 \mu\text{m}$ are confined along the axis of the linear Paul trap and coupled to the optical cavity. We position the ions such that $g_{PD}^1 \approx g_{PD}^2 \approx 2\pi \times 1 \text{ MHz}$, where g_{PD}^i represents the coupling strength of the ion i to the cavity (Chapter 6).

⁷The text in this section and its argumentation informations follow Ref. [45]

Subsequently, we set the Rabi frequencies Ω_1 and Ω_2 of the Raman beam. According to Section 7.2, the Rabi frequencies Ω_1 and Ω_2 should be set such that $\tan^{-1}(g_1/g_2) = \pi/2$, that is, $g_1 = g_2$. By using Eq. 3.13, we obtain expressions for $g_{1,2}$:

$$1 := \frac{g_1}{g_2} = \frac{\xi_{SPD'} \zeta_{PD'}}{\xi_{SPD} \zeta_{PD}} \frac{\Omega_1}{\Omega_2} \sim 0.9 \frac{\Omega_1}{\Omega_2} \Rightarrow \Omega_2 \sim 0.9 \Omega_1. \quad (7.8)$$

However, there is a discrepancy between the expected ratio Ω_1/Ω_2 of 0.9 and the value of 0.75 used in Ref. [30]. We attribute the discrepancy to the fact that the detuning of 400 MHz of both the Raman beam and the cavity might not be large enough compared to the Rabi frequencies $\Omega_i \approx 50$ MHz. In such a case, the approximation of g_i given by Eq. 3.13 might not be accurate.

To perform the experiment presented in this chapter, the ratio between Ω_1 and Ω_2 is set experimentally as follow. After loading only one ion in the trap, we perform the ion-photon entanglement protocol [31]. Subsequently the Rabi frequencies Ω_1 and Ω_2 are set such that the fidelity of the experimentally created state with respect to $|\psi\rangle$ (see Eq. 7.2) is maximized. Using $\Omega_2 = 2\pi \times 47$ MHz and $\Omega_1 = 2\pi \times 29$ MHz, the fidelity is maximized and measured to be $(97 \pm 2)\%$. The fidelity is calculated via quantum state tomography of the compound system of the ion and the photon [76].

Once the Rabi frequencies are set, the experimental sequence to generate entanglement between two ions is described as follows. The ions are first Doppler-cooled, then optically pumped to $|S\rangle$. This preparation step lasts 1.7 ms. Next, a 40 μ s bichromatic Raman pulse is applied, generating the state $|\Psi_{\text{tot}}\rangle$. If two orthogonally polarized photons are not detected at the APDs within these 40 μ s, optical pumping to $|S\rangle$ and the Raman pulse are repeated up to ten times. If all ten trials are ineffective, the sequence starts again with Doppler cooling. In the case of joint detection at times t_1 and t_2 , $|\Psi_{\text{tot}}\rangle$ is projected to $|\Psi_{\text{herald}}\rangle$. Subsequently, the mapping $|D'\rangle \rightarrow |S\rangle$ is implemented, ideally generating the Bell state $|\Psi^+\rangle$. Finally, fluorescence detection for 2 ms determines how many ions are in $|S\rangle$. For coherence measurements, the analysis rotations described in Section 7.3 are implemented before fluorescence detection. For each of the 27 values of the phase ϕ , approximately 1300 entanglement events are recorded, corresponding to 1.5 hours of data acquisition.

The data corresponding to a time interval $T = t_2 - t_1 \leq 0.5 \mu$ s between the two photon detection events are plotted in Fig. 27. The population measurement is indicated by a line, where $\rho_{SD,SD} + \rho_{DS,DS} = 1.00 \pm 0.03$. After the $\sigma_x^{(1)}\sigma_x^{(2)}$ and $\sigma_\phi^{(1)}\sigma_\phi^{(2)}$ rotations, the parity $P_{\Phi^+}(\phi)$ oscillates with period π and has a value of 0.86 ± 0.01 at phase $\pi/2$, determined from a sinusoidal fit. A similar fit to the parity $P_{\Psi^+}(\phi)$ measured without the $\sigma_x^{(1)}\sigma_x^{(2)}$ rotation yields a contrast $C = 0.02 \pm 0.03$.

The contrast of parity oscillations decreases with increasing T . In Fig. 28, the lower bound for the fidelity F_{Ψ^+} is plotted as a function of T for the full data set. Each time bin contains ~ 1750 entanglement events, so that the first bin corresponds to the data of Fig. 27; the bin spacing increases with T as photon coincidence becomes less likely. The observed loss of

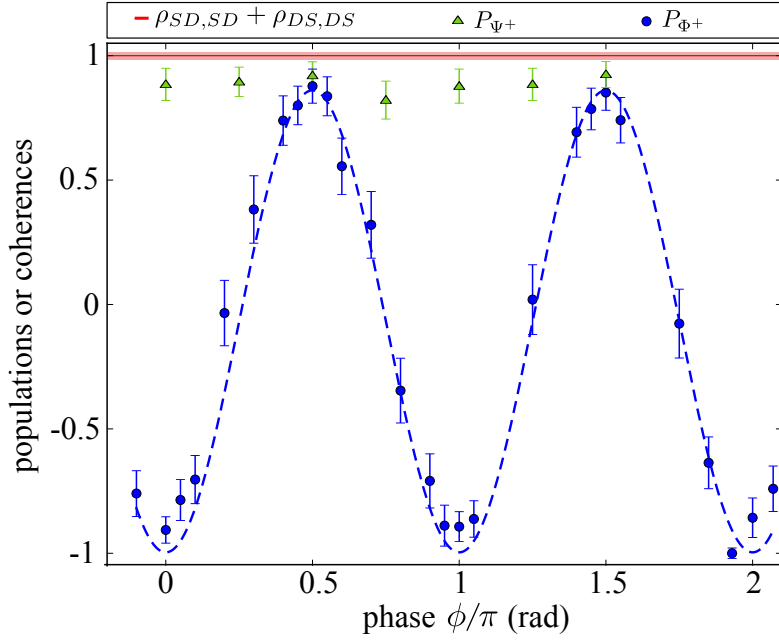


Figure 27: Parity measurements. Three measurements are used to bound the fidelity of the entangled state. First, the sum of population terms $\rho_{SD,SD}$ and $\rho_{DS,DS}$ is determined directly after entanglement. This measurement is independent of phase and is indicated by a red line whose width represents the uncertainty. Second, after two $\pi/2$ rotations on the $|S\rangle \leftrightarrow |D\rangle$ optical transition, the parity is measured (see text for definitions). The parity oscillates as a function of the relative phase of the rotations (blue circles). A sinusoidal fit is indicated by a dashed line. Third, the parity is measured after only one $\pi/2$ pulse as a function of that pulse's phase (green triangles). Each data point represents about 50 entanglement events. Error bars represent one standard deviation, where the sources of error are projection noise and the determination of p_k from fluorescence data. The figure has been taken from Ref. [45].

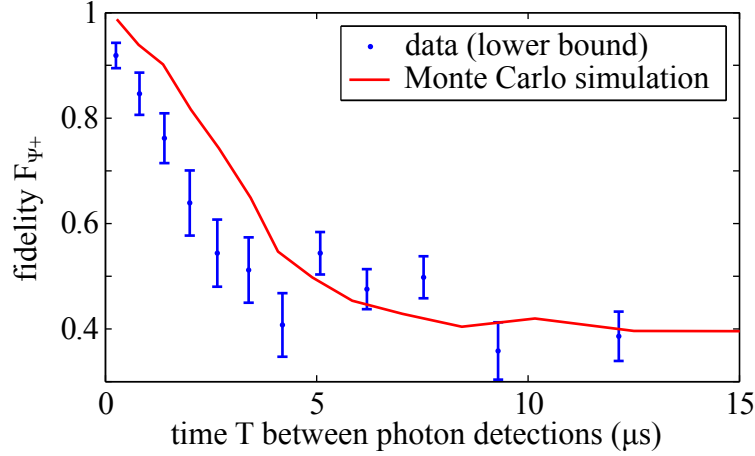


Figure 28: Lower bound of the fidelity of the entangled state with respect to Ψ^+ as a function of the detection interval T between photons. As scattering within this interval removes the indistinguishability of the ions, the fidelity decreases with increasing T . The fidelity drops below 50% for large T due to the possibility of coherent evolution after a scattering event, which may result in the Bell state Ψ^- . This process is reproduced by a Monte Carlo simulation of the fidelity (red line). Error bars correspond to one standard deviation. The figure has been taken from Ref. [45].

fidelity is due to scattering from the $4^2P_{3/2}$ manifold back to $|S\rangle$ while the coherent Raman transition is in progress. A scattering event allows us in principle to distinguish between the two ions. Thus, the indistinguishability required for entanglement is lost.

One might expect that for large times T , the coherence $\rho_{SD,DS}$ approaches zero with population p_1 remaining constant, resulting in a fidelity at the classical limit of 50%. However, the fidelity drops below this limit (Fig. 28), due to the generation of coherences following scattering. When an ion spontaneously decays after one cavity photon has already been detected, the ions are projected to a state with the first ion in $|S\rangle$ and the second in $|D\rangle$ or $|D'\rangle$. The second photon can be generated in two ways. In one process, the second photon is generated from the ion in $|S\rangle$ and exits the cavity. In another process, the photon does not exit the cavity but is reabsorbed via the reverse Raman transition by the ion in $|D\rangle$ or $|D'\rangle$. Subsequently, this ion emits another photon, which exits the cavity. Because a geometric phase is acquired in the second process, the interference of these two processes results in a negative coherence term $\rho_{DS,SD}$.

This effect has been reproduced in numerical simulations via the quantum Monte Carlo method using the Quantum Optics Toolbox for Matlab [123]. The simulations have been implemented by Birgit Brandstätter in the context of her doctoral thesis, and further details of the implementation can be found in Ref. [34]. For each ion, the system Hamiltonian takes into account the four electronic levels shown in Fig. 26a and an additional Zeeman state $|D_{-1/2}\rangle$ that is weakly coupled to $|S\rangle$ by an off-resonant Raman process. The ions are coupled to the

two cavity modes. The two-ion state is evaluated as a function of the arrival times of two orthogonally polarized photons, with the result shown in Fig. 28. In comparison to the data, the fidelity in the simulation is higher for small T . This mismatch is attributed to imperfect state readout due to the finite ion temperature. Furthermore, the simulated fidelity decreases slightly more slowly than the measured fidelity, which is explained by uncertainties in the calibration of laser linewidths, ion-cavity coupling strengths and Rabi frequencies.

Finally, we discuss the entanglement rate and the probability of success of the experiment, that is, the ratio between the number of attempts in which entanglement has been measured and the total number of attempts. For the data corresponding to a time interval $T \leq 0.5 \mu\text{s}$ with a fidelity $F_{\Psi^+} \geq (91.9 \pm 2.5)\%$, entanglement of the two ions is generated at a rate of 0.2 events per second. In this case, the probability of success of the protocol is 0.010%. For the data with a minimum fidelity of $F_{\Psi^+} = (54 \pm 2)\%$, the entanglement rate is increased up to 4.8 events per second, with a probability of success of 0.07%.

7.5 Experimental considerations of the protocol

In Section 7.2, we describe a protocol to generate heralded entanglement between the ions. Two assumptions have been made in order to write Eq. 7.4. The first assumption is that the bichromatic Raman field applied to both ions generates the state $|\psi\rangle \otimes |\psi\rangle$ (see Eq. 7.3), and the second is that the photons generated by the ions are indistinguishable.

Let us first analyze the assumption of photon indistinguishability. Photon indistinguishability requires both temporal and spatial indistinguishability. Temporal indistinguishability means that the probability to generate a photon as function of time should be the same for both ions, i.e., the temporal shape of each photon generated by each ion should overlap. The temporal shape of the photons is influenced by both the coupling strength g_{DP}^i of ion i to the cavity mode and the Rabi frequency of the Raman beam seen by that ion.

In Chapter 6, we have seen how the two ions can be positioned such they are coupled with equal strength to the cavity mode. Additionally, the Raman beam has been broadened such that its intensity is the same at the position of each ion. Thus the temporal indistinguishability is established. In Chapter 9, we will see measurements of the temporal shape of photons generated by each ion. In order to take those measurements, we have made use of the addressing 729 nm beam to selectively “hide” one of the ions in a state that is not coupled to the Raman process. The software needed to implement the “hiding” operation was developed after the measurements presented in this chapter were taken (see Fig. 19a).

Spatial indistinguishability means that the probability to detect a photon as function of any spatial coordinate should be the same for photons generated by both ions. In our scheme, photons are emitted into the optical cavity in the same spatial mode, thus providing intrinsically spatial overlap. Therefore both spatial and temporal photon indistinguishability is completely fulfilled.

Now, we discuss the assumption that the bichromatic Raman field applied to both ions generates the state $|\psi\rangle \otimes |\psi\rangle$ (see Eq. 7.3). In general, the process described in Ref. [30] generates entanglement between the electronic state of the ion and the polarization of a single cavity photon:

$$|\psi(\theta, \phi_r, \phi_g)\rangle = e^{i\phi_g} \cdot (\sin(\theta)|DH\rangle + \cos(\theta)e^{i\phi_r}|D'V\rangle), \quad (7.9)$$

where the phase ϕ_r is the relative phase between the two frequency components of the Raman beam, the angle θ is defined by the relative intensity between the two frequencies component and ϕ_g is the optical phase of both components at the ion's position at the beginning of the process.

If the process is applied to two ions, two indistinguishable photons that are entangled with the two ions are generated. As explained in Section 7.2, the two photons exit the cavity and are separated spatially depending on their polarization by using the PBS (see Fig. 26b). If one horizontally polarized and one vertically polarized photon are detected, and we use Eq. 7.9 instead of Eq. 7.2, the state $|\Psi_{\text{tot}}\rangle = |\psi(\theta_1, \phi_{r_1}, \phi_{g_1})\rangle \otimes |\psi(\theta_2, \phi_{r_2}, \phi_{g_2})\rangle$ is projected to:

$$|\Psi_{\text{herald}}\rangle = e^{i(\phi_{g_1} + \phi_{g_2})} (\sin(\theta_1) \cos(\theta_2) |DD'\rangle + e^{i(\phi_{r_2} - \phi_{r_1})} \cdot \cos(\theta_1) \sin(\theta_2) |D'D\rangle) \quad (7.10)$$

where now the subindex 1 or 2 in each variable is used to distinguish between the two ions.

We note that:

- The phase $\phi_{g_1} + \phi_{g_2}$ is a global phase and therefore can be neglected.
- As the Raman beam has been broadened such that the intensity of the beam is the same at the position of each ion, the relative intensity between the two frequency components of the Raman beam is the same for both ions, that is, $\theta_1 = \theta_2 \equiv \theta$.
- Although the optical phases of the two components of the Raman beam at each ion's position are different, the phase difference is the same, that is, $\phi_{r_1} = \phi_{r_2}$.

Considering these points above discussed, Eq. 7.10 can be written as Eq. 7.4.

We finally note that in order to write Eq. 7.4, it is not required to set the Rabi frequencies of the two components of the Raman beam such that $\theta = \pi/2$. The angle θ determines which of both Raman transitions is strongly driven. For example, in the case that the transition $|S\rangle \rightarrow |D\rangle$ is driven stronger than the transition $|S\rangle \rightarrow |D'\rangle$, then, it is more probable to detect photons which are H polarized than V polarized. However, as $\theta_1 = \theta_2$, both ions generate H polarized photons with an increased probability; thus, the polarization degree of freedom does not contain information related to which of the ions has generated the photon. Therefore, in the case that two orthogonally polarized photons are detected, ions are projected onto a maximally entangled state as photons are completely indistinguishable. For $\theta = \pi/2$, the probability to detect two orthogonally polarized photons is one half, leading to a situation where the protocol is maximally efficient. In the case that $\theta \neq \pi/2$, the efficiency of the process is reduced but without affecting the fidelity of the entangled state of the ions.

7.6 Conclusions

In the experiment presented in this chapter, we have generated ion–ion entanglement with a fidelity of at least 55(2)% at a rate of one event every 0.23 seconds, while the data subset of Fig. 27 with a high-fidelity of 91.9(25)% corresponds to a rate of one event every 5 seconds. The probability of success of the protocol in these cases are 0.01% and 0.07%, respectively. These rates would be similar if the ions were located in spatially separated cavities in order to generate entanglement of remote ions as discussed in Section 6.4.

In 2007, Hofmann et al. generated entanglement of remote atoms with a fidelity of 63(3)% with respect to a Bell state at a rate of about one event every 100 seconds. The probability of success was measured to be between $10^{-5}\%$ and $10^{-7}\%$ [24]. In this case, photons were emitted in free space and only 2% of them were collected with the use of a high numerical aperture lens. In 2015, Hucul et al. generated entanglement of remote ions with a fidelity of 78(3)% with respect to a Bell state at a rate of one event every 0.22 seconds [14]. In this work, the repetition rate has been substantially increased in comparison with the work of Ref. [23], mainly due to the implementation of a large numerical aperture single-atom microscope objective ($NA = 0.6$), which collects 10% of the light emitted by the ion. The probability of success has thus been increased and measured to be 0.009%.

In our current setup, the entanglement rate can be further increased without performing changes to the experimental apparatus. First, both Doppler cooling and detection times can be decreased. For the presented data, we used 1.7 ms and 2 ms for each of these processes; however, 700 μ s for Doppler cooling and 1 ms for detection would have been sufficient. Second, in 2013, after the data shown in this chapter had been taken, we installed a new computer to control the experiment. With the old computer, every 200 repetitions of the experiment⁸, the computer required almost 100 ms in order to process the data recorded by the PMT and by the APD. With the new computer, this time has been significantly decreased to 30 ms. Thus, in the case that a new set of data is taken, considering the point mentioned, I estimate that the entanglement rate could be increased by at least 40%.

Further improvement in the probability of success and in the entanglement rate can be obtained by implementing a cavity with higher output efficiency, a faster cavity decay or a stronger ion-cavity coupling. Note that our current cavity has a relatively low output coupling efficiency of 20(2)% (see Section 4.4) and a low decay rate of 50 kHz (see Section 4.2). In the next chapter we will see how the ion-cavity coupling can be effectively increased by using a crystal of ions in a superradiant state.

Finally, we note that the present scheme could also be extended to generate N –ion Dicke states, heralded by the detection of m horizontal and $(N - m)$ vertical photons [19].

⁸In our group, these repetitions are usually referred to as a cycles

8 Sub- and superradiance with two ions and an optical cavity

In Chapter 6 we have seen that the individual coupling of two ions to the mode of the optical cavity can be tuned. In particular, a configuration in which both ions are equally and maximally coupled to the optical cavity has been shown. Using such a configuration, we presented our results in Chapter 7 regarding entanglement generation between the two ions mediated by the optical cavity. In this chapter we show the implementation of a second experiment that relies on the technique described in Chapter 6. We demonstrate the generation of subradiant and superradiant states [35] of two ions in an optical cavity.

To generate the subradiant and superradiant states, we prepare a maximally entangled state of two ions that are equally and maximally coupled to the optical cavity. The phase of the entangled state determines the collective interaction of the ions with the cavity mode, that is, whether the emission of a single photon into the cavity is suppressed or enhanced. By adjusting this phase, we tune the ion–cavity system from sub- to superradiance. These results have been published in Ref. [46].

The enhancement in the emission of a single photon originates from the effective enhancement in the coupling strength to the mode of the optical cavity that the superradiant state exhibits. In Chapter 9, the implementation of a quantum protocol that makes use of such an enhancement will be described. We will encode a single qubit in the two-ion superradiant state and show that this encoding enhances the transfer of quantum information onto a photon.

Note that in order to perform the experiment described in this chapter, the entanglement between the two ions has been generated via a Mølmer–Sørensen gate operation (see Section 5.8). The heralded protocol described in Chapter 7 could also be used to generate the required entanglement; however, the Mølmer–Sørensen gate offers higher fidelity at a higher repetition rate.

8.1 Introduction

Subradiance and superradiance are fundamental effects in quantum optics that occur when a group of emitters coherently interacts with the same mode of an electromagnetic field [35, 124, 125]. This interaction causes suppression or enhancement of the rate at which the light is radiated, and this variation is related to the particular collective state of the emitters. Those states are referred as sub- and superradiant states.

Superradiance and subradiance are discussed in detail in Ref. [35], in which it is first studied for two emitters and then for large ensembles. For the latter case, superradiance has been widely studied, and effects such as changes in radiation rates [37], a phase transition [38, 39] and narrow-linewidth lasing [40] have been observed. The case of two emitters is discussed below in detail. We first study the interaction between the emitters and the vacuum field and then between the emitters and the field of an optical cavity.

8.1.1 Two emitters in free space

Consider two emitters and their radiation into the vacuum field. Here, we discuss how the presence of one emitter affects the emission of the other following the analysis of Dicke [35]. Assume an atomic two-level system with an electric dipole transition between the ground and the excited level. If one atom is in the excited state, it will emit a photon into the vacuum mode after a time $1/\Gamma$, where Γ is the decay rate. Now, consider a second atom in the ground state such that the atom–atom separation is much smaller than the wavelength of the radiated light. This assumption implies photon indistinguishability, i. e., it is not possible to say which atom emitted the photon. Assuming that both emitters are completely independent, the radiation process of the first atom should be unaffected by the presence of the second, and therefore after a time $1/\Gamma$, the probability of finding both atoms in the ground state should be one. But according to a quantum mechanical description that takes into account the symmetry of the system under the interchange of particles, the same probability is just one half.

The result described above can be explained as follows. The initial state $|\psi_0\rangle$ of one atom in the ground state $|\downarrow\rangle$, another in the excited state $|\uparrow\rangle$, and the radiation field in the vacuum state can be written as

$$|\psi_0\rangle = |\uparrow\downarrow\rangle |0\rangle = (|\psi_+\rangle + |\psi_-\rangle) |0\rangle / \sqrt{2}, \quad (8.1)$$

where

$$\begin{aligned} |\psi_+\rangle &= (|\uparrow\downarrow\rangle + |\downarrow\uparrow\rangle) \sqrt{2}, \\ |\psi_-\rangle &= (|\uparrow\downarrow\rangle - |\downarrow\uparrow\rangle) \sqrt{2} \end{aligned} \quad (8.2)$$

are triplet and singlet components. Due to symmetry conservation, the triplet component $|\psi_+\rangle$ is capable of radiating and decaying to the ground state $|\downarrow\downarrow\rangle$ as both states are part of the triplet subspace. The singlet component $|\psi_-\rangle$ is decoupled from the triplet space and therefore does not decay. Thus, after a time $t \gg 1/\Gamma$:

$$|\psi_0\rangle \mapsto (|\downarrow\downarrow\rangle |1\rangle + |\psi_-\rangle |0\rangle) / \sqrt{2}$$

and the probability of finding the system in $|\downarrow\downarrow\rangle$ is one half, corresponding to the emission of one photon.

In the case that no photon has been emitted, the system is in the state $|\psi_-\rangle$, and it is no longer possible to say which of the atoms is excited. This state is referred to as the subradiant state $|\Psi_{\text{sub}}\rangle \equiv |\psi_-\rangle$, as it does not radiate into the vacuum field. On the other hand, the triplet state $|\psi_+\rangle$ interacts with the vacuum field and the transition rate of its decay to the ground state $|\downarrow\downarrow\rangle$ can be calculated to be 2Γ using Fermi's golden rule [35, 126]. The triplet state $|\psi_+\rangle$ thus decays faster than a single atom, and therefore it is referred to as the superradiant state $|\Psi_{\text{super}}\rangle \equiv |\psi_+\rangle$.

Assume now that the atom–atom separation becomes larger than the wavelength of the radiated light and that a detector of light is located beside the atoms. The initial state $|\psi_0\rangle$ is written as

$$|\psi_0\rangle = |\uparrow_{\vec{k}}\downarrow_{\vec{k}'}\rangle, \quad (8.3)$$

where \vec{k} and \vec{k}' are the wave vectors of the light that arrives from each atom at the detector. In general, if the detector is located such that $\vec{k} \neq \vec{k}'$, the decomposition of $|\psi_0\rangle$ into triplet and singlet components is not possible as the atoms are coupled to different light modes. Therefore, after a time $1/\Gamma$,

$$|\psi_0\rangle \mapsto |\downarrow_{\vec{k}}\downarrow_{\vec{k}'}\rangle,$$

and the probability of finding both atoms in the ground state is one, corresponding to the first atom having emitted a photon.

Both sub- and superradiance of two emitters were observed in a pioneering experiment using two trapped ions [41]. In the experiment described in Ref. [41], a microscopic ion trap of planar geometry [127] was used. Such a trap produced a confinement potential strong enough to bring two barium ions within 1 micrometer of each other. In order to see sub- and superradiance, a strong light pulse first excited both ions, preparing the state $|\uparrow\uparrow\rangle$. Ideally, that is assuming photon indistinguishability, after the detection of a first photon, the ions' state was projected to $(|\uparrow\downarrow\rangle + e^{i\phi(d)}|\downarrow\uparrow\rangle)/\sqrt{2}$, in which the phase ϕ was a function of the ion–ion separation d . Varying the ions' separation allowed both the sub- and superradiant state to be populated. Finally, the lifetime of the state was measured for various values of d . The excited-state lifetime was measured to be $(1.5 \pm 0.8)\%$ longer for the subradiant state, and $(1.2 \pm 0.9)\%$ shorter for the superradiant state. The contrast was limited because spontaneous emission from the ions was not indistinguishable, as the ions' separation ($\approx 1\mu\text{m}$) was on the order of the wavelength of the emitted light ($\approx 500\text{ nm}$).

This limitation can be overcome by observing emission into a preferred spatial mode, such as that defined by an optical cavity. Looking at Eq. 8.3, for the particular case in which $k = k'$, the emitted light is indistinguishable, and Eq. 8.3 can be written as Eq. 8.1. Therefore sub- and superradiance can be observed. In a cavity setting, a cavity photon is spatially delocalized in the cavity mode. The probability that a photon has been emitted by a particular emitter is related to the coupling of that emitter to the cavity mode. Therefore, photon indistinguishability is guaranteed if emitters are equally coupled, even if their separation is larger than the wavelength of the cavity field. In a cavity configuration, subradiance corresponds to suppressed interaction of the joint state of the emitters with the cavity mode, while for the superradiant state, the interaction is enhanced.

8.1.2 Two emitters in an optical cavity

Consider two emitters interacting with a single mode of an optical cavity. As before, assume that each emitter is a two-level system with a ground $|\downarrow\rangle$ and an excited $|\uparrow\rangle$ state, and that the

cavity frequency matches the energy difference $\hbar\omega$ between the ground and the excited state. The system is described by the Tavis–Cummings Hamiltonian [128]:

$$H_{\text{TC}} = H_{\text{emitters}} + H_{\text{cavity}} + H_{\text{int}}$$

where H_{emitters} and H_{cavity} are the bare Hamiltonians of the emitters and the cavity, and H_{int} describes the interaction between the emitters and the cavity field:

$$\begin{aligned} H_{\text{emitters}} &= \frac{\hbar\omega}{2} \left(\sigma_z^{(1)} + \sigma_z^{(2)} \right) \\ H_{\text{cavity}} &= \hbar\omega a^\dagger a \\ H_{\text{int}} &= \hbar g \left(\sigma_-^{(1)} + e^{i\zeta} \sigma_-^{(2)} \right) a^\dagger + \text{h. c.}, \end{aligned} \quad (8.4)$$

where $\sigma_z^{(j)} = (|\uparrow^{(j)}\rangle\langle\uparrow^{(j)}| - |\downarrow^{(j)}\rangle\langle\downarrow^{(j)}|)$, $\sigma_-^{(j)} = |\uparrow^{(j)}\rangle\langle\downarrow^{(j)}|$ is the lowering operator for the emitter j , ζ represents a relative phase, a^\dagger is the creation operator of a photon in the cavity mode, and g is the coupling strength between each emitter and the cavity field.

The sub- and superradiant states for H_{TC} are the states that respectively minimize and maximize the transition probability⁹ to the state $|\downarrow\downarrow\rangle$. The subradiant state

$$|\Psi_{\text{sub}}\rangle = |\downarrow\uparrow\rangle + e^{-i\zeta} |\uparrow\downarrow\rangle \quad (8.5)$$

can be shown to satisfy

$$T_{\text{sub}} = \frac{2\pi}{\hbar} |\langle\downarrow\downarrow| H_{\text{int}} |\Psi_{\text{sub}}\rangle|^2 = 0,$$

while the superradiant state is

$$|\Psi_{\text{super}}\rangle = |\downarrow\uparrow\rangle + e^{-i(\zeta+\pi)} |\uparrow\downarrow\rangle \quad (8.6)$$

for which the transition probability is maximized:

$$T_{\text{super}} = \frac{2\pi}{\hbar} |\langle\downarrow\downarrow| H_{\text{int}} |\Psi_{\text{super}}\rangle|^2 = 2g^2. \quad (8.7)$$

In order to quantify the enhancement, we calculate the transition probability of the separable state $|\uparrow\downarrow\rangle$ to the ground state $|\downarrow\downarrow\rangle$:

$$T_{\text{one}} = \frac{2\pi}{\hbar} |\langle\downarrow\downarrow| H_{\text{int}} |\uparrow\downarrow\rangle|^2 = \frac{2\pi}{\hbar} |\langle\downarrow| H_{\text{int}} |\uparrow\rangle|^2 = g^2, \quad (8.8)$$

that is, half the probability of that of the superradiant state.

⁹ The transition probability calculated as $T_{i \rightarrow f} \equiv \frac{2\pi}{\hbar} |\langle\Psi_f| H |\Psi_i\rangle|^2$ [126] depends on the coupling strength between the initial state $|\Psi_i\rangle$ and the final state $|\Psi_f\rangle$ of a system described by H , and on the number of ways the transition can happen, that is, on the density of the final states. A transition probability $T_{i \rightarrow f} = 0$ means that the initial and the final state are not coupled, i. e., the transition is forbidden, while $T_{i \rightarrow f} \neq 0$ means that the initial and the final state are coupled. In the case that the energies are discrete and non-degenerate, the density of the final states is one.

Tavis–Cummings model as an effective Jaynes–Cummings model

In order to interpret the results of the previous section, we now estimate the rates of the atomic population transfer when the emitters are prepared in the superradiant state and in the subradiant state, and we compare these rates with those of the single emitter.

In the case that both emitters are prepared in the entangled state $|\Psi(\phi)\rangle = |\downarrow\uparrow\rangle + e^{-i\phi} |\uparrow\downarrow\rangle$, the two-emitter crystal interacting with an empty quantized field can be studied as a single emitter interacting with the same quantized field. In other words, the Tavis–Cummings model can be described as an effective Jaynes–Cummings model with an effective coupling $g_{\text{eff}}(\phi)$ between both emitters and the quantized field.

This description is possible because the states $|n\rangle |\Psi(\phi)\rangle$ and $|n+1\rangle |\downarrow\downarrow\rangle$ under the interaction of H_{int} are decoupled from the rest of the Hilbert space, where $|n\rangle$ denotes the photon number state of the cavity. Therefore, the two two-level systems can be studied as one effective two-level system with states $|\Psi(\phi)\rangle$ and $|\downarrow\downarrow\rangle$. The coupling rate between these states is given by the effective Rabi frequency $g_{\text{eff}}(\phi)$, the frequency of the Rabi oscillation between $|\downarrow\downarrow\rangle$ and $|\Psi(\phi)\rangle$.

Assuming that the initial state of the system is $|\Psi(\phi)\rangle$ and the cavity is empty, the populations of the states $|\Psi(\phi)\rangle$ and $|\downarrow\downarrow\rangle$ as a function of time t are given by

$$P_{\Psi}(t) = \cos^2(2g_{\text{eff}}t) \quad P_{\downarrow\downarrow}(t) = \sin^2(2g_{\text{eff}}t), \quad (8.9)$$

and the photon number in the cavity is $\bar{n}(t) = P_{\downarrow\downarrow}(t)$.

In case that the emitters are prepared in $|\Psi_{\text{sub}}\rangle$, the effective coupling is $g_{\text{eff}} = 0$, and the joint state does not exchange energy with the cavity ($\bar{n} = 0$). On the other hand, if the emitters are prepared in the state $|\Psi_{\text{super}}\rangle$, the joint state exchanges energy with the cavity at the maximum half-rate of $g_{\text{eff}} = \sqrt{T_{\text{super}}} = g\sqrt{2}$, which is $\sqrt{2}$ times faster than the half-rate of energy exchange of the single emitter (see Eqs. 8.7 and 8.8).

The sub- and superradiant nature of a system consisting of two emitters coupled to an optical cavity is therefore present in the effective coupling g_{eff} between the joint state of the emitters and the cavity mode. In chapter 6 we have shown that we can equally couple two ions to the same mode of an optical cavity. In the next section we will describe how we prepare a maximally entangled two-ion state and tune its emission properties between sub- and superradiance, that is, between a dark state $|\Psi_{\text{sub}}\rangle$ and a state $|\Psi_{\text{super}}\rangle$ that couples with enhanced strength $g\sqrt{2}$ to the cavity. In Chapter 9 we will implement a quantum information transfer protocol that benefits from the described coupling enhancement exhibited by the superradiant state.

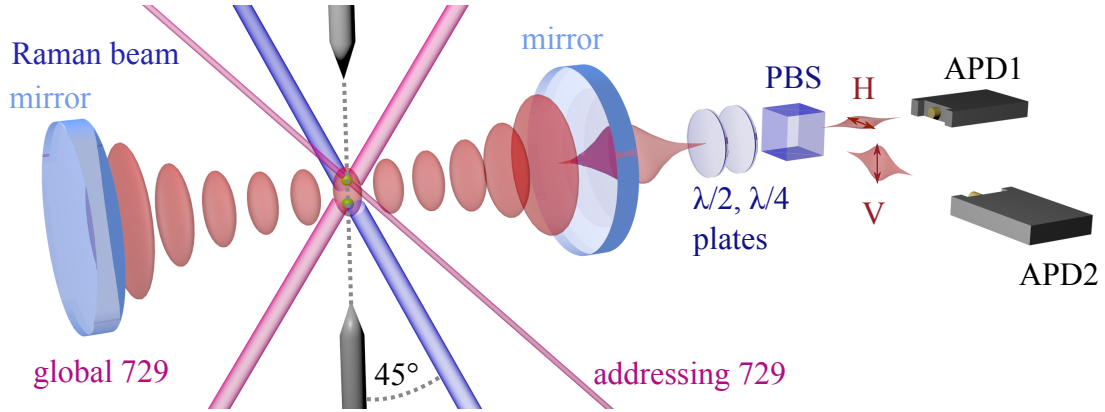


Figure 29: Two $^{40}\text{Ca}^+$ ions in a linear Paul trap couple with equal strength to the mode of a high-finesse optical cavity. For the purpose of illustration, the two ions are shown as being coupled to the same antinode. In the experiment, they are in fact coupled to adjacent antinodes. Quantum information stored in the ions is manipulated using two 729 nm beams: the global beam couples to both ions, while the addressing beam is focused onto one ion. A 393 nm laser beam drives a cavity-mediated Raman transition, generating a single photon in the cavity. At the cavity output, two wave plates ($\lambda/2$, $\lambda/4$) select the basis in which photon polarization is analyzed. Two avalanche photodiodes (APD1 and APD2) detect the horizontally (H) or vertically (V) polarized photons at the output of a polarizing beamsplitter (PBS). The figure has been taken from Ref. [46].

8.2 Description of the experiment ¹⁰

Two $^{40}\text{Ca}^+$ ions separated by $5.6 \mu\text{m}$ are confined along the axis of a linear Paul trap and coupled to an optical cavity. The optical cavity at 854 nm couples the $4^2P_{3/2}$ and $3^2D_{5/2}$ manifolds. We position the ions so that $g_{PD}^1 \approx g_{PD}^2 \approx 1 \text{ MHz}$, where g_{PD}^j represents the coupling strength of the ion j to the cavity (see Chapter 6). A Raman beam at 393 nm that couples the $4^2S_{1/2}$ and $3^2D_{5/2}$ manifolds is orthogonal to both a magnetic field of magnitude $B = 4.5 \text{ G}$ and the cavity axis (see Fig. 29).

We now follow the derivation described in Section 3.1. Assume that $|S\rangle$, $|P\rangle$ and $|D\rangle$ are three states from the $4^2S_{1/2}$, $4^2P_{3/2}$ and $3^2D_{5/2}$ manifolds respectively. The part of the Hamiltonian that describes the interaction of the ions with the Raman laser and the cavity is (see Eq. 3.5)

$$H_{\text{int}} = \hbar g_{PD} (\sigma_{PD}^{(1)} - \sigma_{PD}^{(2)}) a^\dagger + \frac{\hbar \Omega}{2} (e^{i\phi_R^{(1)}} \sigma_{SP}^{(1)} + e^{i\phi_R^{(2)}} \sigma_{SP}^{(2)}) + \text{h.c.}, \quad (8.10)$$

where $\sigma_{PD}^{(i)} \equiv |D\rangle\langle P|$, $\sigma_{SP}^{(i)} \equiv |P\rangle\langle S|$, a^\dagger is the photon creation operator, and $\phi_R^{(i)}$ is the optical phase of the Raman beam when interacting with the ion i , and the minus sign between the first, and the second terms of Eq. 8.10 accounts for the fact that in our system the two ions are located

¹⁰The text in this section and its argumentation informations follow Ref. [46]

in adjacent antinodes of the cavity.

When the Raman resonance condition is met (see Eq.3.7), the three-level system ($|S\rangle$, $|P\rangle$ and $|D\rangle$) can be mapped onto an effective two-level system ($|S\rangle$ and $|D\rangle$) with an effective Raman coupling between the two states. In such a case, Eq. 8.10 can be rewritten as Eq. 8.4, identifying $\zeta = (\phi_R^{(1)} - \phi_R^{(2)})$ and $\sigma_- = |D\rangle\langle S|$. The relative phase ζ is given by $\zeta = 2\pi d \sin \theta / \lambda$, where d is the ions' separation, $\theta \approx 45^\circ$ is the angle between trap axis and Raman beam, and $\lambda = 393$ nm is the wavelength of the Raman beam (see Fig. 29). The coupling g in Eq. 8.4 corresponds to the effective Rabi frequency of the Raman process given by Eq. 3.8.

In this experiment we use $|S_{-1/2}\rangle$, $|P_{-1/2}\rangle$ and $|D_{-1/2}\rangle$. A linearly polarized Raman beam with Rabi frequency $\Omega = 19$ MHz drives the $|S_{-1/2}\rangle \rightarrow |D_{-1/2}\rangle$ transition, generating linearly polarized cavity photons. Photons leaving the cavity cross a half- and a quarter-wave plate aligned such that they are reflected by the beam-splitter and detected by APD2 (see Fig. 29). Using Eq. 3.13 and Eq. 3.10, we calculate that the rates of the effective two-level system are $\gamma_{\text{eff}} = 2\pi \times 6$ kHz and $g = 2\pi \times 18$ kHz. The cavity decay rate $\kappa = 2\pi \times 50$ kHz is thus the dominant rate.

To generate an entangled state of the two ions, we use the global 729 nm laser beam (Fig. 29) that couples with equal strength to both ions on the $4^2S_{1/2} - 3^2D_{5/2}$ quadrupole transition (see Fig. 19b). The target state

$$|\Psi^+\rangle \equiv (|S\rangle|D\rangle + |D\rangle|S\rangle) / \sqrt{2}$$

is prepared with a fidelity of at least $(95 \pm 2)\%$ via a Mølmer-Sørensen gate operation followed by a $\pi/2$ -rotation on the $|S\rangle \leftrightarrow |D\rangle$ transition with a phase 1.2π with respect to previous entangling pulse. Refer to Section 5.8 for a detailed description of both the Mølmer-Sørensen gate operation and the calculation of the fidelity of the entangled state. Subsequently, the addressing 729 nm beam is used to induce AC-Stark shifts in the addressed ion (see Section 5.9), which contribute a phase φ to the entangled state [95]:

$$|\Psi(\varphi)\rangle \equiv (|S\rangle|D\rangle + e^{i\varphi}|D\rangle|S\rangle) / \sqrt{2}. \quad (8.11)$$

By adjusting the length of the Stark-shift pulse, we shift this phase φ , which determines the effective coupling g_{eff} of $|\Psi(\varphi)\rangle$ to the cavity mode. In analogy to Eq. 8.5 and Eq. 8.6, the superradiant and subradiant states are given by

$$\begin{aligned} |\Psi_{\text{super}}\rangle &\equiv |\Psi(\varphi = -\zeta)\rangle \\ |\Psi_{\text{sub}}\rangle &\equiv |\Psi(\varphi = -\zeta + \pi)\rangle. \end{aligned} \quad (8.12)$$

As discussed in Section 8.4, the Raman process between $|S\rangle$ and $|D\rangle$ generates a single cavity photon from $|\Psi(\varphi)\rangle$ as only one ion is in the state $|S\rangle$. In the next section, we discuss how the temporal shape of this photon is expected to be influenced by the effective coupling $g_{\text{eff}}(\varphi)$ of the state $|\Psi(\varphi)\rangle$. In Section 8.3 we then show our measurement of the variation of the temporal shape of the photon as function of the effective coupling g_{eff} .

8.2.1 Expected variation of the temporal shape of generated photon in our setup

Now, we discuss the influence of the effective coupling g_{eff} of the state $|\Psi(\varphi)\rangle$ on the temporal shape of the photon when a Raman process is driven. First note that in the absence of scattering ($\gamma_{\text{eff}} = 0$), the probability that a photon has been generated in the cavity is given by the population of the state $|DD\rangle$. As seen in Section 8.1.2, the population of the state $|DD\rangle$ is calculated considering the Rabi oscillation at the effective Rabi frequency $2g_{\text{eff}}$ between the states $|\Psi_{\text{super}}\rangle$ and $|DD\rangle$.

Assuming that the ions' state at time zero is $|\Psi_{\text{super}}\rangle$, the population of the state $|DD\rangle$ as function of the duration t of the process is $P_{DD}^{g_{\text{eff}}}(t) = \sin^2(2g_{\text{eff}}t)$ (see Eq. 8.9). Performing a second-order Taylor expansion around $t = 0$, the population $P_{DD}^{g_{\text{eff}}}(t)$ can be approximated by

$$p_{DD}^{g_{\text{eff}}}(t) \approx 4(g_{\text{eff}}t)^2 = 4(g\sqrt{2}t)^2$$

for $t \ll 1/g$. In a similar analysis but assuming now that the enhancement is not present ($g_{\text{eff}} = g$), the population of the state $|DD\rangle$ can be approximated by

$$P_{DD}^g(t) \approx 4(gt)^2.$$

As the ratio $P_{DD}^{g_{\text{eff}}}(t)/P_{DD}^g(t) = 2$, the state $|DD\rangle$ is populated twice as fast when the enhancement is present, doubling the probability of generating a cavity photon. In the case that $\kappa \gg g$, photons typically leave the cavity before they are reabsorbed by the ions. Thus, the probability to generate and detect a photon from $|\Psi_{\text{super}}\rangle$ for $t \ll 1/g$ is expected to be twice as high as compared to the case in which the enhancement is not present.

In the case that the state $|\Psi_{\text{sub}}\rangle$ is prepared, the coupling to the cavity vanishes ($g_{\text{eff}} = 0$). The state $|DD\rangle$ is not populated, and therefore no photon is expected to be generated and detected.

In case that $\gamma_{\text{eff}} \neq 0$, there is off-resonant excitation to the $4^2P_{3/2}$ manifold. From the $4^2P_{3/2}$ manifold, the ion decays back to the $4^2S_{1/2}$ manifold, emitting a distinguishable photon in free space. In such a case, the entangled states $|\Psi_{\text{super}}\rangle$ and $|\Psi_{\text{sub}}\rangle$ are projected to $|SD\rangle$ or $|DS\rangle$, and neither suppression nor enhancement in the coupling is present any longer. As for our system, in which $\gamma_{\text{eff}} \lesssim g$, we expect this effect to have a small but non-negligible influence on the measured results.

8.3 Results ¹¹

We now determine the probability to generate and detect a photon for a range of phases φ . The experimental sequence starts with 1 ms of Doppler cooling. The ions are then optically pumped to $|S\rangle$, followed by 1.3 ms of sideband cooling on the axial center-of-mass mode (see

¹¹The text in this section and its argumentation informations follow Ref. [46]

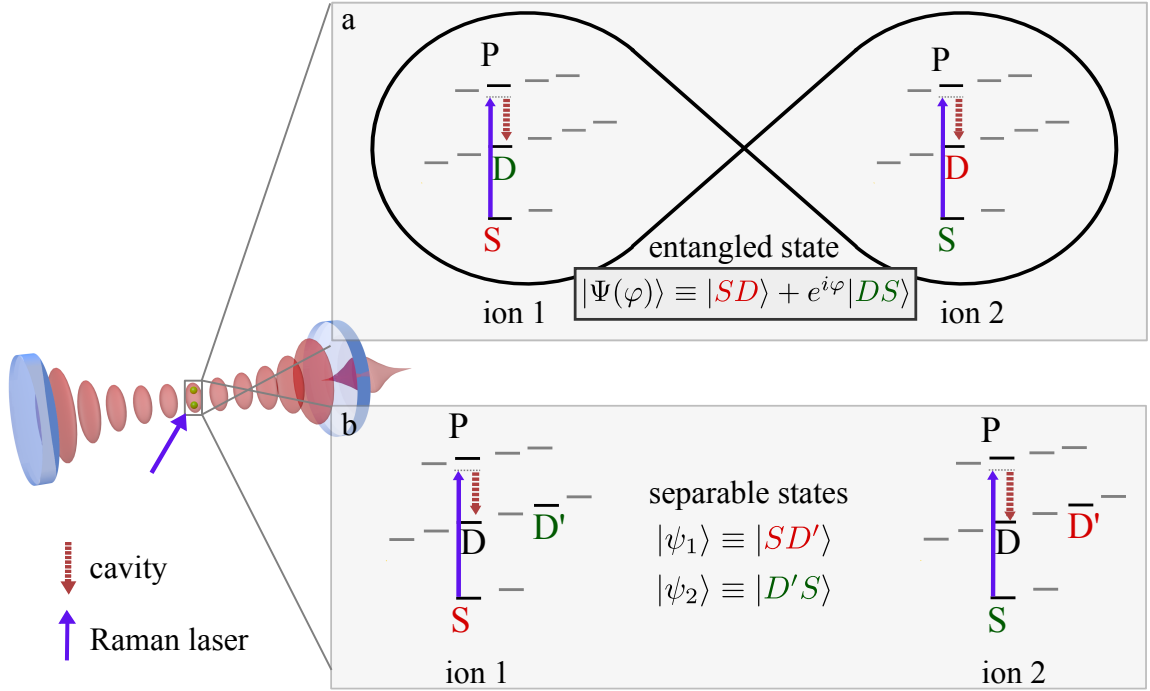


Figure 30: (a) The two ions are prepared in an entangled state $|\Psi(\varphi)\rangle \equiv (|S\rangle|D\rangle + e^{i\varphi}|D\rangle|S\rangle)/\sqrt{2}$ for various values of φ . (b) The two ions are prepared in separable state $|\psi_1\rangle = |SD'\rangle$ or state $|\psi_2\rangle = |D'S\rangle$. (a,b) The global beam then drives a Raman transition between $|S\rangle$ and $|D\rangle$, generating a single cavity photon for each ion in $|S\rangle$. Since $|D'\rangle$ is decoupled from the cavity interaction, both $|\psi_1\rangle$ and $|\psi_2\rangle$ in (b) represent a single ion interacting with the cavity.

Section 5.2). Next, global and addressing 729 nm pulses generate the state $|\Psi(\varphi)\rangle$ (See Section 5.9). In the last step, the cavity-mediated Raman transition $|S\rangle \rightarrow |D\rangle$ is driven for $55 \mu\text{s}$ and photons are detected (see Fig. 30a).

In order to determine whether we achieve enhancement and suppression of the cavity coupling with respect to the single-ion rate g , we carry out a reference measurement. For this single-ion case, one of the two ions is hidden in a state $|D'\rangle \equiv |D_{3/2}\rangle$ that is decoupled from the Raman process. Thus, the initial state is $|\psi_1\rangle \equiv |S\rangle|D'\rangle$ or $|\psi_2\rangle \equiv |D'\rangle|S\rangle$ (see Fig. 30b). The state $|\psi_1\rangle$ is generated by applying a π -pulse on the $|S\rangle \leftrightarrow |D'\rangle$ transition using the addressing 729 nm beam. For generating $|\psi_2\rangle$, a π pulse using the global 729 nm beam on the same transitions is applied after preparing $|\psi_1\rangle$.

For the states $|\Psi(\varphi)\rangle$, we calculate $\eta(\varphi)$, the probability to detect a photon in the first $6 \mu\text{s}$ of the Raman process. The time is chosen such that $6 \mu\text{s} < 1/(2\pi \times g) = 1/(2\pi \times 18 \text{ kHz}) \approx 9 \mu\text{s}$ in order to be able to measure the enhancement predicted in the previous section. For the single-ion cases, we calculate η_ψ , the average value of the photon detection probability for $|\psi_1\rangle$ and $|\psi_2\rangle$ in the same time window. Fig. 31 shows the ratio $r(\varphi) = \eta(\varphi)/\eta_\psi$ as the phase φ is varied. For $\varphi = 0.68\pi$, the experimentally determined minimum, the ratio is 0.22(9): photon

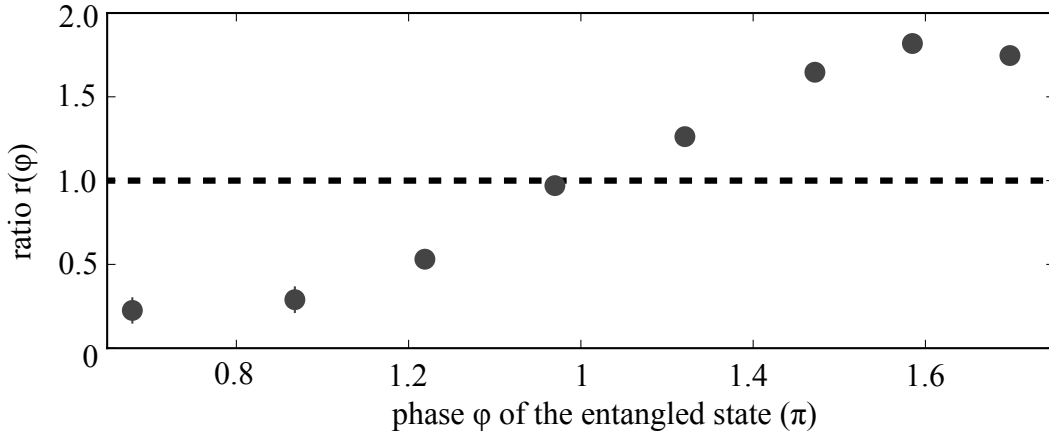


Figure 31: Ratio $r(\varphi)$ of the probability to detect a photon for $|\Psi(\varphi)\rangle$ to that of $|\psi_1\rangle$ as a function of the phase φ for the first 6 μs of the Raman process. The reference single-ion case is shown as a dashed horizontal line. Error bars are calculated propagating the error in the probabilities to detect a photon, the error of which are calculated assuming Poissonian statistics. The figure has been taken from Ref. [46].

generation is strongly suppressed. We therefore identify $|\Psi(\varphi = 0.68\pi)\rangle$ with $|\Psi_{\text{sub}}\rangle$. As φ is increased, the ratio approaches one, then enters the superradiant regime. A maximum value of $r(\varphi)$ is found for $\varphi = 1.58\pi$. For the corresponding state, identified with $|\Psi_{\text{super}}\rangle$, the probability to detect a photon is 1.84(4), close to its maximum value of two, thus demonstrating strong enhancement in photon generation.

Note that the phase difference between $|\Psi_{\text{super}}\rangle$ and $|\Psi_{\text{sub}}\rangle$ is 0.9π . Ideally, the difference should be exactly π (see Eq. 8.12). During the time in which the data has been taken, we first found the phase $\varphi = 1.58\pi$ that maximized the probability to detect a photon, then we took more data using the phases shown in Fig. 31. Later on, when we were analyzing the results, we realized that we were not careful enough to take data for the phase $\alpha = 1.58\pi + \pi$. This phase would have corresponded to the phase that, ideally, would have minimized the probability to detect a photon.

For these states $|\Psi_{\text{sub}}\rangle$ and $|\Psi_{\text{super}}\rangle$, we now analyze the temporal photon shapes at the detector (Fig. 32). The temporal shapes corresponding to $|\psi_1\rangle$ and $|\psi_2\rangle$ are considered as a reference; from their overlap, we find the coupling strengths of the two ions, g_{PD}^1 and g_{PD}^2 , to be within 10% of one another. This value is consistent with the phase difference of 0.9π between the two ions with respect to the standing wave measured in Chapter 6. As seen in Eq. 8.10, an equal coupling strength of the ions to the cavity is required to perform the experiment described in this chapter. Photons generated from $|\Psi_{\text{super}}\rangle$ exhibit a steeper initial slope than the single-ion case, while $|\Psi_{\text{sub}}\rangle$ has a flatter slope. The photon shapes are consistent with enhanced and suppressed coupling to the cavity and are in good agreement with simulations.

The simulations are based on numerical integration of the master equation and include imperfect preparation of the initial state and off-resonant excitation to the $3^2D_{5/2}$. These effects

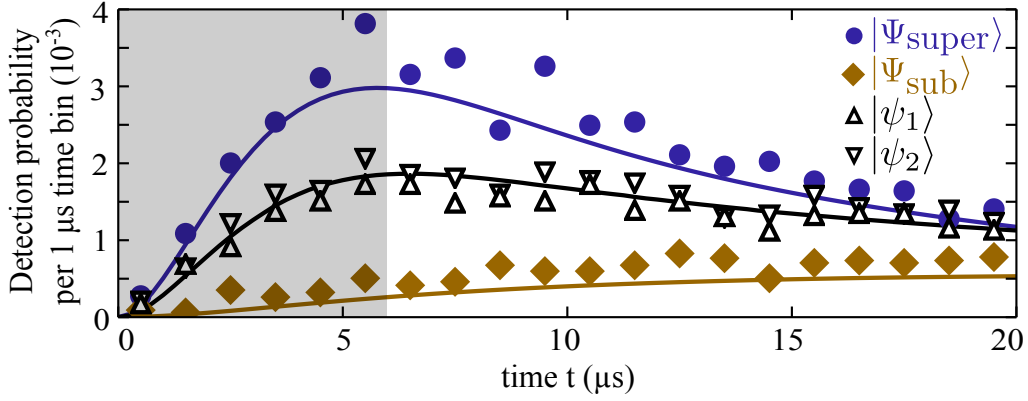


Figure 32: Temporal shape of the photon at the cavity output as a function of detection time t , for the entangled states $|\Psi_{\text{super}}\rangle$ (circles) and $|\Psi_{\text{sub}}\rangle$ (diamonds) and the single-ion cases $|\psi_1\rangle$ and $|\psi_2\rangle$ (up and down triangles, respectively). The temporal photon shapes are calculated by normalizing the detected photon counts per $1 \mu\text{s}$ time bin by the number of photon generation attempts. Data are shown until $20 \mu\text{s}$, the time scale for which enhancement and suppression are most prominent. Lines are simulations. The shaded area represents the time window used in Fig. 31. Error bars represent Poissonian statistics and are mostly smaller than the plot symbols. The figure has been taken from Ref. [46].

account for the small but nonzero probability to generate photons from $|\Psi_{\text{sub}}\rangle$. The imperfect preparation has a small influence on the results, as in at least $(95 \pm 2)\%$ of the attempts, the state $|\Psi_{\text{sub}}\rangle$ is prepared. Assuming that in 5% of the attempts, a state that produces a photon is generated instead, the ratio should be smaller than 0.05 . However, the measured ratio of $0.22(9)$ is more than four times this amount. Off-resonant excitation to the $3^2D_{5/2}$ is mainly responsible for the discrepancy. The rate at which off-resonant excitation happens is constant; therefore, the probability to populate $|\psi_1\rangle$ or $|\psi_2\rangle$, states that produce a photon, increases with the duration of the experiment.

For $|\Psi_{\text{super}}\rangle$, imperfect preparation of the initial state and off-resonant excitation reduces the photon generation probability by about 10% for the first $6 \mu\text{s}$ of the process. Note that the maximum value of two in the enhancement of the probability to detect a photon is only valid for times close to zero (see the discussion in Section 8.2.1). For longer times, the value of the enhancement is expected to decrease. In particular, for a time scale much longer than $1/g$, the states $|\psi_1\rangle$, $|\psi_2\rangle$ and $|\Psi_{\text{super}}\rangle$ have a similar probability of about 80% , which is obtained by simulations, to generate a photon in the cavity; therefore, enhancement is not expected.

We have demonstrated the generation of sub- and superradiant states of two ions by showing an increase and decrease in the probabilities to detect a photon compared with the single-ion case. It is reasonable to ask whether the increased probability of generating a photon is related not to superradiance but simply to the fact that two ions are used. The assumption that each ion generates a photon would then explain the measured results. In the next section, we will see that the two-ion crystal in an entangled state generates single photons, demonstrating that the

measured enhancement is related to the superradiant nature of the state, and not to the generation of two photons.

8.4 Two-ion crystal as a single photon source

In 2004, Keller et al. showed the continuous generation of single photons by means of a cavity-mediated Raman transition using a $^{40}\text{Ca}^+$ ion [84]. There, the cavity coupled the $4^2S_{1/2}$ and the $3^2D_{3/2}$ manifolds, and the Raman beam coupled the $4^2S_{1/2}$ and the $4^2P_{1/2}$ manifolds. However, in the experiment presented in Ref. [84], the Zeeman sublevels of the $^{40}\text{Ca}^+$ ion had not been resolved. Helena Barros, a former doctoral student working with this setup, explored the interaction between the optical cavity and a single trapped $^{40}\text{Ca}^+$ ion considering the Zeeman sublevels of the ion [91]. In the course of her work, she measured that one ion in a state $|S\rangle$ produces a single photon when a Raman transition between $|S\rangle$ and $|D\rangle$ is driven [17].

In this section, we show that two ions prepared in the entangled state $|\Psi(\phi)\rangle$ produce a single photon when a Raman transition is driven. In order to show that the two ions produce a single photon, we estimate the number of expected two-photon detection events based on independent calibrations and then compare the expected values with our measurement.

In the experiments presented in this chapter and in Chapter 9, we consider two ions in the entangled state $|\Psi(\phi)\rangle$, for which the probability to find one ion in $|S\rangle$ is one. When a Raman transition is driven between $|S\rangle$ and $|D\rangle$, the entangled state $|\Psi(\phi)\rangle$ is transferred to $|D\rangle|D\rangle$ and a single photon is expected. However, imperfect preparation of $|\Psi(\phi)\rangle$ leaves some population in $|S\rangle|S\rangle$, resulting in the generation of two photons.

In order to estimate the number of two-photon detection events, we consider detector dark counts and imperfect preparation of the ions' state. The following four events are relevant and contribute to two-photon detections:

1. State $|S\rangle|S\rangle$ is generated; two photons are produced and detected.
2. State $|S\rangle|S\rangle$ is generated; two photons are produced, one is lost and the other is detected together with a dark count.
3. State $|\Psi(\phi)\rangle$ is generated; one photon is produced and is detected together with a dark count.
4. Two darks count are detected.

State tomography reveals that in $(3 \pm 2)\%$ of attempts to generate $|\Psi(\phi)\rangle$, the state $|S\rangle|S\rangle$ is prepared instead. The probability to detect one photon during the $55 \mu\text{s}$ duration of the Raman process is $(5.4 \pm 0.3)\%$, which is mainly limited by cavity absorption and detector efficiencies [44]. Detector dark count rates are $(3.2 \pm 0.1) \text{ s}^{-1}$ and $(3.8 \pm 0.1) \text{ s}^{-1}$ for the two

avalanche photodiodes (see Section 4.4) for a characterization of the avalanche photodiodes). With these values, we expect one two-photon event in $(8.2 \pm 0.8) \times 10^3$ attempts to generate a single photon.

To measure two-photon events, we generate $(|S\rangle|D\rangle + |D\rangle|S\rangle)/\sqrt{2}$ and $(|S'\rangle|D\rangle + |D\rangle|S'\rangle)/\sqrt{2}$ and drive a cavity-mediated Raman transition such that a horizontally or a vertically polarized photon is generated. Photons leaving the cavity cross a half-wave plate aligned such that 50% of the light is reflected and 50% transmitted by a polarizing beam splitter (see Fig. 29). Photons are detected by the two avalanche photodiodes at each beam-splitter output and the second-order correlation function $g^{(2)}(0)$ is calculated. After 223,106 attempts to generate photons, 28 two-photon events were measured, and 27 ± 3 two-photon events were expected from the considerations above. The observed number of two-photon detection events are thus consistent with single-photon generation.

8.5 Conclusions

Here, we have been able to tune the effective coupling strength of the two-ion crystal to the mode of the optical cavity. In particular, we have demonstrated the creation of sub- and superradiant states of two ions inside the optical cavity. The subradiant state has been measured to have a maximum suppression of 78(9)% in the probability to generate a single photon in the cavity compared with the single ion case. In contrast, the superradiant state has been measured to have a maximum enhancement of 84(4)% in the probability to generate a cavity photon, also compared with the single ion case.

A similar experiment using ions in free space showed a suppression of 1.2(9)% and an enhancement of 1.5(8)% in the excited-state lifetime, mainly limited by the fact that the ion-ion separation was comparable to the wavelength of the radiated field [41]. In our experiment, the spatial delocalization of the photons inside the cavity mode provided the photon indistinguishability required to observe sub- and superradiance, even in the case that the ion-ion separation is much larger than the wavelength of the radiated field.

We emphasize two advantages of using ions in this experiment: first, that as seen in Chapter 6, the coupling strength of each ion to the cavity can be precisely controlled, and second, that the universal set of gate operations described in Chapter 5 allows preparation of a range of states, from sub- to superradiant. By tuning over this range, one could selectively turn off and on the coupling of logical qubits to the cavity. As an example, a scheme in which two quantum computers share quantum information via a direct exchange of photons is described in Fig. 33. In such a scheme, all the ions are used to perform calculations, while a subset of two ions, which are coupled to the mode of an optical cavity, are responsible of the exchange of information. After a particular calculation has been performed, these two ions are prepared in an entangled state, and then, the information is encoded in the two-ion crystal. Finally, after performing a state transfer process, the information will or will not be transferred to the remote

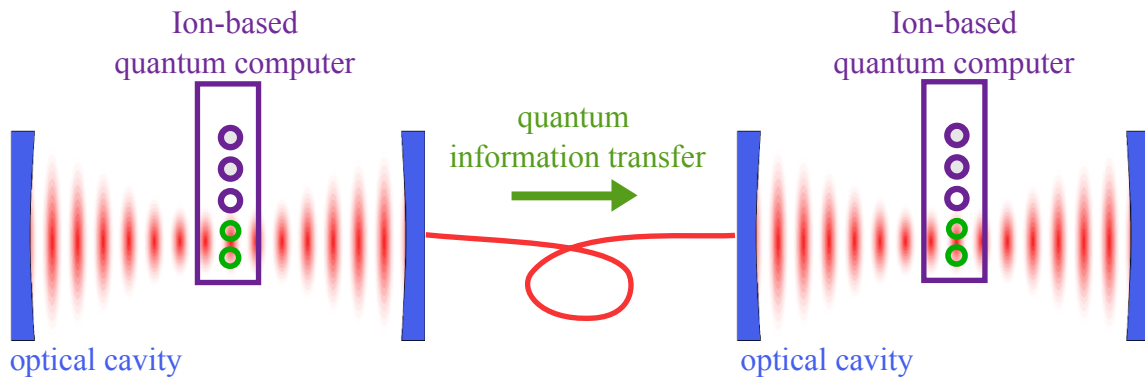


Figure 33: Proposed scheme in which two quantum computers can be used to selectively share quantum information via a direct exchange of photons. A subset of two ions prepared in an entangled state are coupled to the mode of an optical cavity. Depending on the phase of the entangled state, that is, if ions are in the superradiant or subradiant state, the information will be transferred to the other two remote ions or will remain.

ions depending on the phase of the entangled state, that is, if ions are in the superradiant or subradiant state,

The scheme described in Fig. 33 presents an additional advantage. In the case that the ions are prepared in the superradiant state, not only is the coupling turned on, but also the fidelity of the process that transfers the information onto a single photon is enhanced compared to the fidelity of a similar process that uses a single ion. This enhancement is shown next in Chapter 9.

9 Enhanced ion-photon state mapping

In Chapter 8, we have shown the creation of sub- and superradiant states of two ions in the optical cavity. In particular, we have demonstrated that the superradiant state exhibits an enhanced coupling strength to the mode of the optical cavity. In this chapter, a direct application of such an enhanced coupling strength is described. We show the implementation of an enhanced version of cavity-based quantum information transfer between matter and light. To implement the protocol, information is encoded in the electronic state of two ions in a superradiant state and transferred to the polarization degree of freedom of a single photon. We compare the efficiency and fidelity of the process with those of the case in which the information is encoded in a single ion, and we show that both efficiency and fidelity are enhanced. The results related to the enhancement in both the efficiency and fidelity have been published in Ref. [46].

9.1 Introduction

In the context of quantum networks [3, 129], we can distinguish between two approaches for the implementation of quantum interfaces between light and matter: the deterministic and the probabilistic approach. The deterministic approach assumes that given a certain process, the probability of success approaches one, whereas in the probabilistic approach, the probability of success is intrinsically limited.

Superradiance has already been employed to improve the performance of a probabilistic quantum interface [130, 131]. In the protocol proposed by Duan, Lukin, Cirac and Zoller for heralded remote entanglement (the DLCZ protocol), efficient retrieval of photons stored in an atomic ensemble is based on superradiance [130]. A weak incident pulse of light generates a symmetric state of N atoms in which only one atom is excited. The state will then decay by emitting a photon, which is preferably emitted in the same mode as that of the incident light [35]. In such a way, the collection efficiency of the emitted photons has been significantly increased [26].

In Ref. [2], the idea of direct transmission of quantum information between two remote deterministic interfaces is proposed. The protocol considers two deterministic quantum interfaces, each one consisting of an atom coupled to a single mode of an optical cavity. The basic idea is that via a Raman transition, the internal state of an atom in one cavity is transferred to a photon. The photon leaks out of the cavity and is directed along a transmission line to the other interface. Subsequently, the photon enters the cavity, and the state of the photon is transferred to the second atom. Near-unit efficiency in the quantum transmission process between the distant atoms is only possible when both atoms are strongly coupled to the optical cavities [2].

As seen in Chapter 8, the superradiant state has a coupling rate to the cavity that is enhanced with respect to the single-qubit rate. In Ref. [36], Lamata et al. study how this effect can be used to enhance the performance of a quantum interface that would allow the implementation of the

protocol described in Ref. [2] with high efficiency, relaxing the technical requirements for strong coupling between light and matter. In the proposal of Lamata, the enhancement in quantum state transfer between a single ion and a single photon is achieved by using a crystal of N ions. A qubit of information is encoded across the crystal in a superradiant state and subsequently transferred to a photon. The performance of the quantum interface is thus enhanced as the coupling rate of the N -ion crystal to the mode of the cavity is increased to $g\sqrt{N}$, where g is the single-ion coupling rate.

In the Section 9.2, we first outline the original proposal of Ref. [36]. Subsequently, in the Section 9.3 we present a modified version of the protocol, and finally, in Section 9.4 we present and analyze our results after the implementation of this modified version using a two-ion crystal.

9.2 Ion-crystal transducer using the Fock state basis

In Ref. [36], Lamata et al. focus their study on the development of efficient techniques to perform photonic gates mediated by ions, with the purpose of contributing to the field of optical quantum computing [64]. They describe an enhanced process to map the state of a photon onto a crystal of ions. As the process is coherent and thus reversible, we focus our analysis on the reverse process, the mapping of the state of a crystal of ions onto a single photon.

The protocol presented in Ref. [36] assumes N two-level atoms with ground and excited states $|\downarrow\rangle$ and $|\uparrow\rangle$, interacting with an optical cavity that is on resonance with the atomic transition. In Step I, a qubit of information defined by two angles α and β is encoded in one of the N ions:

$$|\phi_0\rangle = |0_{\text{pn}}\rangle |0_{\text{ph}}\rangle \left[\cos(\alpha) |\uparrow_1\rangle + e^{i\beta} \sin(\alpha) |\downarrow_1\rangle \right] |\downarrow_2 \dots \downarrow_N\rangle / \sqrt{2},$$

where $|0_{\text{pn}}\rangle$ stands for zero phonons in one of the vibrational modes of the crystal, and $|0_{\text{ph}}\rangle$ stands for the cavity vacuum. In Step II, the single-ion excitation is mapped onto a collective excitation of the ions. To perform the mapping, the single-ion excitation is first transferred to a single phonon by driving the blue-sideband transition $|0_{\text{pn}}\rangle |\uparrow\rangle \rightarrow |1_{\text{pn}}\rangle |\downarrow\rangle$. Subsequently, the phonon is transferred to a collective excitation of the ions by driving the transition $|1_{\text{pn}}\rangle |\downarrow_1 \dots \downarrow_N\rangle \rightarrow |0_{\text{pn}}\rangle |\Psi_{\text{Dicke}}\rangle$ where $|\Psi_{\text{Dicke}}\rangle = \frac{1}{\sqrt{N}} \sum_i |\downarrow_1 \dots \uparrow_i \dots \downarrow_N\rangle$ is the first state in the superradiant cascade described by Dicke [35]. The state $|\Psi_{\text{Dicke}}\rangle$ has a coupling strength to the cavity that is enhanced from the single-qubit rate g to the effective rate $g\sqrt{N}$. Step II is thus equivalent to the mapping $|\phi_0\rangle \mapsto |\phi_1\rangle$, where:

$$|\phi_1\rangle = |0_{\text{pn}}\rangle |0_{\text{ph}}\rangle \left[\cos(\alpha) |\Psi_{\text{Dicke}}\rangle + e^{i\beta} \sin(\alpha) |\downarrow_1 \dots \downarrow_N\rangle \right] / \sqrt{2}.$$

Finally, in Step III, a process is driven that generates a cavity photon if an ion is in $|\uparrow\rangle$, that is, the mapping $|\phi_1\rangle \mapsto |\phi_2\rangle$ is implemented, where:

$$|\phi_2\rangle = \left[\cos(\alpha) |1_{\text{ph}}\rangle + e^{i\beta} \sin(\alpha) |0_{\text{ph}}\rangle \right] |0_{\text{pn}}\rangle |\downarrow_1 \dots \downarrow_N\rangle / \sqrt{2}.$$

As a result, the qubit originally encoded in the ground and excited states of a single ion is transferred to a superposition of the first two Fock states corresponding to the number of photons in the mode of the cavity.

In Ref. [36], the mapping process is studied as function of the number of ions N and for different values of the single-ion coupling rate g . Lamata et al. show that the process benefits from the enhanced effective coupling rate to the optical cavity that the Dicke state $|\Psi_{\text{Dicke}}\rangle$ exhibits.

9.3 Ion-crystal transducer using the polarization state basis

Here we propose a modified version of the protocol described above. Instead of encoding the qubit in the Fock state basis, we use the polarization degree of freedom of a single photon, resulting in a more robust protocol to photon loss. For example, consider the implementation of both protocols, and assume that the probability of losing the photons is the same for both implementations. The loss can be attributed, for example, to absorption in optical fibers or absorption in the mirrors of the cavity. Using the Fock state basis, when a photon is lost, the state $|1_{\text{ph}}\rangle$ flips to $|0_{\text{ph}}\rangle$, corrupting the transfer. In contrast, using the polarization state basis, bit flips in the polarization state are strongly suppressed as long as optical elements are precisely aligned.

Assume that the excited state $|\uparrow\rangle$ is doubly degenerate and that it can be split into $|\uparrow^a\rangle$ and $|\uparrow^b\rangle$. In Step I, the qubit of information is encoded in the states $|\uparrow^a\rangle$ and $|\uparrow^b\rangle$ of one of the N ions:

$$|\phi_0\rangle = |0_{\text{pn}}^n\rangle |0_{\text{pn}}^m\rangle |0_{\text{ph}}\rangle \left[\cos(\alpha) |\uparrow_1^a\rangle + e^{i\beta} \sin(\alpha) |\uparrow_1^b\rangle \right] |\downarrow_2 \dots \downarrow_N\rangle / \sqrt{2}, \quad (9.1)$$

where $|0_{\text{pn}}^n\rangle$ and $|0_{\text{pn}}^m\rangle$ stand for zero phonons in two vibrational modes n and m (i.e., common axial and common radial modes, or common and breathing axial modes, etc.). In Step II, as before, the single-ion excitation is mapped onto a collective excitation of the ions, but now the procedure is different. To perform the mapping, first the single-ion excitation is coherently mapped onto a superposition of a single phonon in two vibrational modes n and m by simultaneously driving the blue-sideband transitions

$$\begin{aligned} |0_{\text{pn}}^n\rangle |\uparrow^a\rangle &\rightarrow |1_{\text{pn}}^n\rangle |\downarrow\rangle \\ |0_{\text{pn}}^m\rangle |\uparrow^b\rangle &\rightarrow |1_{\text{pn}}^m\rangle |\downarrow\rangle. \end{aligned}$$

Subsequently, the superposition in the vibrational modes is mapped onto the collective excitation of the ions by simultaneously driving the transitions

$$\begin{aligned} |1_{\text{pn}}^n\rangle |\downarrow_1 \dots \downarrow_N\rangle &\rightarrow |0_{\text{pn}}^n\rangle |\Psi_{\text{Dicke}}^a\rangle \\ |1_{\text{pn}}^m\rangle |\downarrow_1 \dots \downarrow_N\rangle &\rightarrow |0_{\text{pn}}^m\rangle |\Psi_{\text{Dicke}}^b\rangle \end{aligned}$$

where the states $|\Psi_{\text{Dicke}}^k\rangle = \frac{1}{\sqrt{N}} \sum_i^N |\downarrow_1 \dots \uparrow_i^k \dots \downarrow_N\rangle$ are of the form of Dicke states with enhanced coupling rate given by $g\sqrt{N}$ [35]. After Step II, $|\phi_0\rangle \mapsto |\phi_1\rangle$ where:

$$|\phi_1\rangle = |0_{\text{pn}}^n\rangle |0_{\text{pn}}^m\rangle |0_{\text{ph}}\rangle \left[\cos(\alpha) |\Psi_{\text{Dicke}}^a\rangle + e^{i\beta} \sin(\alpha) |\Psi_{\text{Dicke}}^b\rangle \right] / \sqrt{2}. \quad (9.2)$$

Finally, in Step III, a process that generates one photon is driven. In this case, the photon polarization depends on the excited state of the ion, that is $|0_{\text{ph}}\rangle |\Psi_{\text{Dicke}}^a\rangle \mapsto |1_{\text{ph}}^H\rangle |\downarrow\rangle$ and $|0_{\text{ph}}\rangle |\Psi_{\text{Dicke}}^b\rangle \mapsto |1_{\text{ph}}^V\rangle |\downarrow\rangle$, where H and V indicate the polarization states of the photon. After Step III, $|\phi_1\rangle \mapsto |\phi_2\rangle$ where:

$$|\phi_2\rangle = |0_{\text{pn}}^a\rangle |0_{\text{pn}}^b\rangle \left[\cos(\alpha) |1_{\text{ph}}^H\rangle + e^{i\beta} \sin(\alpha) |1_{\text{ph}}^V\rangle \right] |\downarrow_1 \dots \downarrow_N\rangle / \sqrt{2}.$$

As a result, the qubit originally encoded in the two states of a single ion is transferred to a superposition in the polarization degree of freedom of a single cavity photon.

As in the original proposal, this process benefits from the enhanced effective coupling rate to the cavity that the states $|\Psi_{\text{Dicke}}^k\rangle$ exhibit. Finally, as discussed at the beginning of this section, we point out that this protocol is robust under photon losses due to the use of the polarization state of a photon.

9.4 Implementation of the ion-crystal transducer in our setup

The experiment described in this chapter focuses on the implementation of Step III of the protocol described in Section 9.3 using a two-ion crystal. We study the enhancement in the state transfer process from a qubit stored in a superradiant state to a single photon, comparing the fidelity and efficiency of the process with that of the case where the qubit is stored in a single ion.

The experimental configuration described in Chapter 8 is used to implement this protocol (See Fig. 29). In Chapter 8.3 we described the creation of the superradiant state $|\Psi_{\text{Super}}\rangle = |SD\rangle + e^{-i0.58\pi} |DS\rangle / \sqrt{2}$ that exhibits an effective coupling rate of $g\sqrt{2}$ to the mode of the optical cavity. In order to follow the proposal introduced in Section 9.3, we first identify the excited state of the ion as the $|S\rangle$ state. The identification is based on the fact that after a Raman process between $|S\rangle$ and $|D\rangle$ is driven, a cavity photon is generated only if the ion is in the ‘‘excited’’ $|S\rangle$ state (see Section 3.1). We split the excited state of the effective two-level system $|S\rangle$ into $|S\rangle \equiv |S_{-1/2}\rangle$ and $|S'\rangle \equiv |S_{+1/2}\rangle$. Two orthogonal superradiant states can be identified:

$$\begin{aligned} |S\rangle &\equiv (|SD\rangle + e^{-0.58i\pi} |DS\rangle) / \sqrt{2} \\ |S'\rangle &\equiv (|S'D\rangle + e^{-0.58i\pi} |DS'\rangle) / \sqrt{2}. \end{aligned}$$

Identifying $|S\rangle \equiv |\uparrow^a\rangle$, $|S'\rangle \equiv |\uparrow^b\rangle$ and $|D\rangle \equiv |\downarrow\rangle$, the states $|S\rangle$ and $|S'\rangle$ are therefore the equivalent of the Dicke states $|\Psi_{\text{Dicke}}^{a,b}\rangle$ for $N = 2$.

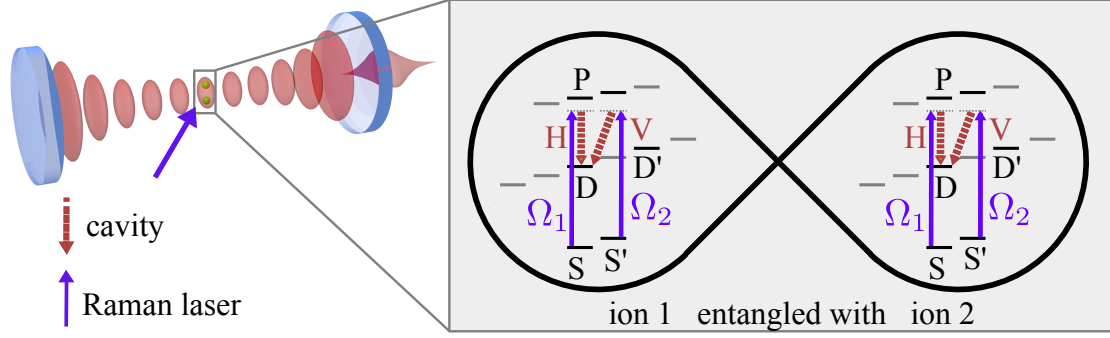


Figure 34: A bichromatic Raman process driven by a bichromatic Raman beam with Rabi frequencies Ω_1 and Ω_2 maps a superposition of $|S\rangle$ and $|S'\rangle$ onto a superposition of single-photon polarization states $|H\rangle$ and $|V\rangle$. The superposition is initially encoded either in two entangled ions or in a single ion, with the other ion decoupled in $|D'\rangle$.

The implementation of Step III is based on the ion-photon state mapping described in Refs. [31, 76]. We use a phase-stable bichromatic Raman process with Rabi frequencies Ω_1 and Ω_2 that coherently transfers $|S\rangle$ to $|D\rangle$, producing a horizontally polarized photon $|H\rangle$, and $|S'\rangle$ to $|D\rangle$, producing a vertically polarized photon $|V\rangle$ (see Fig. 34). Applying such a process to the case of ions in $|S\rangle$ or $|S'\rangle$ results in the generation of a single photon with polarization states $|H\rangle$ or $|V\rangle$, since in $|S\rangle$ and $|S'\rangle$ only one ion is in a photon-generating state $|S\rangle$ or $|S'\rangle$ (see Section 8.4).

Assume that a qubit of information defined by the angles α and β is encoded as a superposition of the two orthogonal superradiant states $|S\rangle$ and $|S'\rangle$:

$$\cos(\alpha) |S\rangle + e^{i\beta} \sin(\alpha) |S'\rangle. \quad (9.3)$$

This superposition is the analogue of the state defined in Eq. 9.2, the result of Step II. The mapping process, that is, Step III, can be represented as:

$$\begin{aligned} &|0\rangle \left[\cos(\alpha) |S\rangle + \sin(\alpha) e^{i\beta} |S'\rangle \right] / \sqrt{2} \\ &\mapsto \left[\cos(\alpha) |H\rangle + e^{i\beta} \sin(\alpha) |V\rangle \right] |DD\rangle / \sqrt{2}, \end{aligned} \quad (9.4)$$

for which the qubit encoded as a superposition of the two superradiant states $|S\rangle$ and $|S'\rangle$ inside an empty cavity $|0\rangle$ is transferred to a superposition of the polarization states $|H\rangle$ and $|V\rangle$ of a single cavity photon.

9.5 Result of the implementation of the ion-crystal transducer

In order to characterize the mapping represented in Eq. 9.4, we extract the fidelity of the process after implementing process tomography. From the process tomography, we extract the process matrix χ , which describes a general transformation from the input density matrix ρ_{in} to the corresponding output density matrix ρ_{out} :

$$\rho_{\text{out}} = \sum_{i,j} \chi_{ij} \sigma_i \rho_{\text{in}} \sigma_j$$

where $\sigma_i \in \{\mathbb{1}, \sigma_x, \sigma_y, \sigma_z\}$ are the Pauli operators [76, 132]. As the target mapping corresponds to the identity operation, the process fidelity is given by the matrix entry χ_{00} .

In order to perform a process tomography, as in Chapter 8, the experimental sequence starts with 1 ms of Doppler cooling, then optical pumping to the $|S\rangle$ state, followed of 1.2 ms of sideband cooling on the axial center-of-mass mode. Subsequently, the two ions are prepared in one of the four orthogonal input states $|S\rangle$, $|S'\rangle$, $|S - S'\rangle \equiv (|S\rangle - |S'\rangle)/\sqrt{2}$ and $|S + iS'\rangle \equiv (|S\rangle + i|S'\rangle)/\sqrt{2}$. Finally, the Raman transition is driven, and for each input state, we measure the polarization state of the output photon via state tomography, using three measurements in orthogonal bases. This set of measurements allows χ to be reconstructed via the maximum likelihood method [133].

The four input states used to reconstruct χ are created as follows. For the state $|S\rangle$, the two ions are prepared in the superradiant state

$$|S\rangle \equiv (|SD\rangle + e^{-i0.58\pi} |DS\rangle)/\sqrt{2}$$

following the steps described in Section 8.3. For the state $|S'\rangle$, after the creation of $|S\rangle$, the state $|S\rangle$ is mapped onto $|S'\rangle$ by applying two global π -pulses, first on the $|S\rangle \leftrightarrow |D'\rangle$ transition and subsequently on the $|D'\rangle \leftrightarrow |S'\rangle$ transition, where $|D'\rangle \equiv |D_{3/2}\rangle$. Therefore after the two π -pulses:

$$|S\rangle \mapsto |S'\rangle \equiv (|S'D\rangle + e^{-i0.58\pi} |DS'\rangle)/\sqrt{2}.$$

For the remaining two states $|S - S'\rangle$ and $|S + iS'\rangle$, after the creation of $|S\rangle$, we apply a global $\pi/2$ -rotation on the $|S\rangle \leftrightarrow |D'\rangle$ transition with a relative phase β with respect to the last $\pi/2$ -rotation implemented to create $|S\rangle$:

$$|S\rangle \rightarrow \left[(|S\rangle + e^{i\beta} |D'\rangle) |D\rangle + e^{-i0.58\pi} |D\rangle (|S\rangle + e^{i\beta} |D'\rangle) \right] / \sqrt{4}.$$

Finally, the state $|D'\rangle$ is mapped onto $|S'\rangle$ by applying a π -pulse on the $|D'\rangle \leftrightarrow |S'\rangle$ transition:

$$\rightarrow \left[(|S\rangle + e^{i\beta} |S'\rangle) |D\rangle + e^{-i0.58\pi} |D\rangle (|S\rangle + e^{i\beta} |S'\rangle) \right] / \sqrt{4}. \quad (9.5)$$

After distributing and regrouping terms, Eq. 9.5 can be written as:

$$\begin{aligned} & \left[(|SD\rangle + e^{i\beta}|S'D\rangle) + e^{-i0.58\pi}(|DS\rangle + e^{i\beta}|DS'\rangle) \right] / \sqrt{4} = \\ & = \left[(|SD\rangle + e^{-i0.58\pi}|DS\rangle) + e^{i\beta}(|S'D\rangle + e^{-i0.58\pi}|DS'\rangle) \right] / \sqrt{4} = \\ & = (|S\rangle + e^{i\beta}|S'\rangle) / \sqrt{2}. \end{aligned}$$

The states $|S - S'\rangle$ and $|S + iS'\rangle$ are thus created when β is set to π and $\pi/2$, respectively.

In order to reconstruct the polarization state of the output photon for each of the four input states, we measure the polarization in three orthogonal bases. The bases are horizontal/vertical (H/V), diagonal/anti-diagonal (D/A) and right-/left-circular (R/L). Labeling $|H\rangle$ and $|V\rangle$ the polarization eigenstates for the (H/V) basis, the eigenstates in the (D/A) and (R/L) bases are defined to be

$$\begin{aligned} |L\rangle &\equiv (|H\rangle - i|V\rangle) / \sqrt{2} & |R\rangle &\equiv (|H\rangle + i|V\rangle) / \sqrt{2} \\ |D\rangle &\equiv (|H\rangle + |V\rangle) / \sqrt{2} & |A\rangle &\equiv (|H\rangle - |V\rangle) / \sqrt{2}. \end{aligned}$$

A polarization measurement in a particular basis is obtained by averaging the results measured in two data sets in order to compensate for unequal detection efficiencies of the avalanche photodiodes (APDs) and imbalanced losses in the optical path (see [76] and Section 4.4). For the first data set, the polarization of the photon is measured in the basis (H, V), (D, A) or (R, L). In the second data set, the bases are inverted and the polarization is measured in the basis (V, H), (A, D) or (L, R). In this case, the notation (X, Y) indicates that X -polarized photons are detected by APD1 and Y -polarized photons are detected by APD2. The bases are determined by the angles of the half- and quarter-wave plates at the output of the optical cavity (see Table 3 and Fig. 29).

(APD1, APD2)	$\lambda/2$ angle (deg)	$\lambda/4$ angle (deg)
(H, V)	0	0
(D, A)	22.5	0
(R, L)	0	45
(V, H)	45	0
(A, D)	-22.5	0
(L, R)	0	-45

Table 3: Angles of the half- and quarter-wave plates that set the basis of the polarization measurement.

A requirement for ion-photon state mapping is the temporal overlap of orthogonally polarized photons generated by ions in states $|S\rangle$ and $|S'\rangle$ [31]. If the overlap is not perfect, superposition states of $|S\rangle$ and $|S'\rangle$ are not correctly mapped onto superpositions of the polarization states $|H\rangle$ and $|V\rangle$ at all times after the mapping starts. For example, assume that after

a time t after the bichromatic Raman process described in Ref. 9.4 starts, it is twice as likely that a horizontally polarized photon has arrived at the detector than that a vertically polarized one has arrived. In such a case, the superposition state $(|S\rangle + |S'\rangle)/\sqrt{2}$ is incorrectly mapped onto $(\frac{4}{3}|H\rangle + \frac{2}{3}|V\rangle)/\sqrt{2}$ as the probability to detect an horizontally polarized photon is twice the probability to detect a vertically polarized photon.

Overlap of orthogonally polarized photons is achieved when $g_1 = g_2$, where g_1 and g_2 are the effective Rabi frequencies given by Eq. 3.13;

$$1 := \frac{g_1}{g_2} = \frac{\xi_{SD} \Omega_1}{\xi_{S'D} \Omega_2} = \frac{1 \Omega_1}{2 \Omega_2} \Rightarrow \Omega_1 = 2 \Omega_2. \quad (9.6)$$

In this experiment, the Rabi frequencies are set to $\Omega_1 = 19$ and $\Omega_2 = 9.5$ MHz. Therefore, $g_1 = g_2 = 12$ kHz and $\gamma_{eff} = 7.5$ kHz.

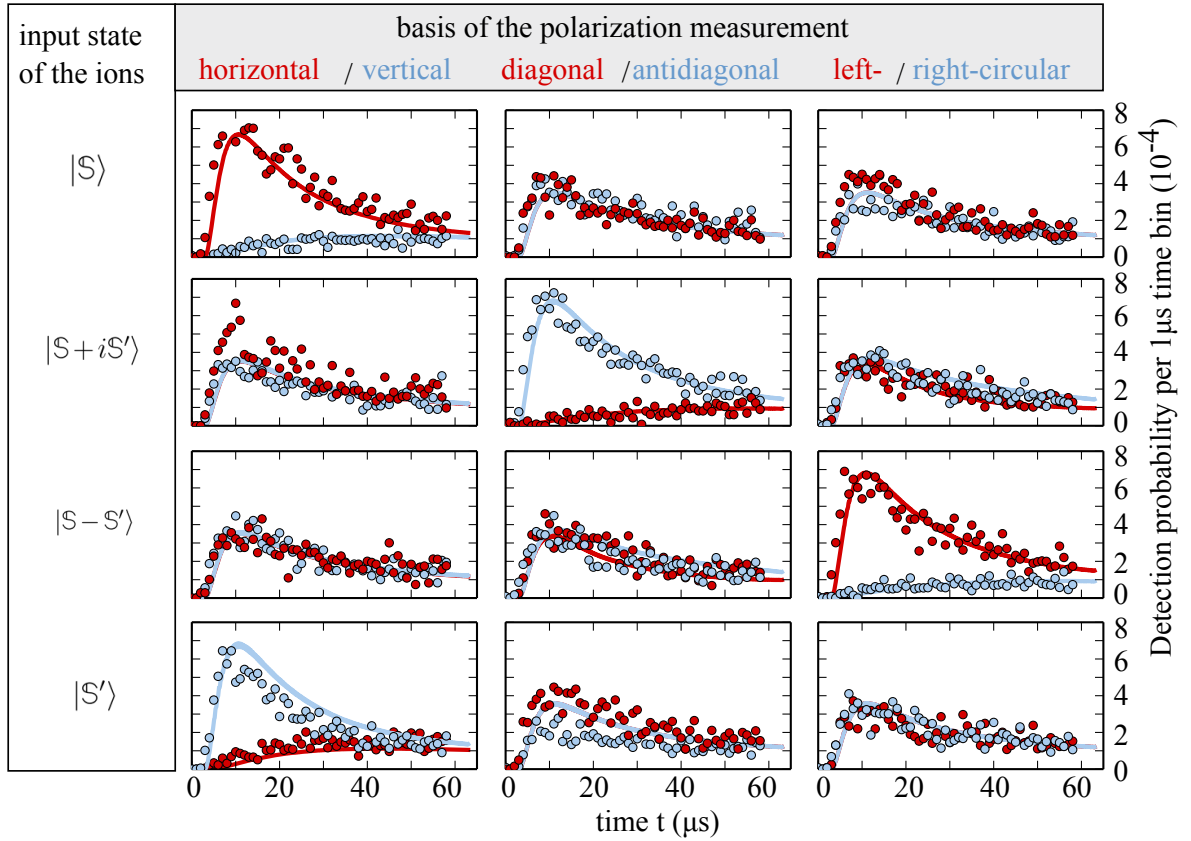


Figure 35: Temporal shape of the generated photon for each of four input states (see text for definitions) measured in the three orthogonal bases H/V , D/A and R/L as function of the detection time t . Lines are simulations.

Fig. 35 shows the temporal shape of generated photons for each input state measured in the three orthogonal bases H/V , D/A and R/L as a function of the detection time t . Early in the process, that is, for times shorter than $1/\gamma_{eff} = 1/(2\pi \times 7.5 \text{ kHz}) \sim 20 \mu\text{s}$, generated photons are horizontally $|H\rangle$ and vertically $|V\rangle$ polarized for input states $|S\rangle$ and $|S'\rangle$ as described by

Eq. 9.4. For the same period of time and for the input state $|\mathbb{S} + i\mathbb{S}'\rangle$, the process generates photons which are $|A\rangle$ polarized. For the last input state, $|\mathbb{S} - \mathbb{S}'\rangle$, photons which are $|L\rangle$ polarized are generated. As the length of the detection window is increased, the probability for off-resonant excitation to the $4^2P_{3/2}$ -manifold increases. If such an event happens during the Raman process, the initial state is randomly projected onto $|SD\rangle$ or $|S'D\rangle$, and the polarization of the photon is either $|H\rangle$ or $|V\rangle$, regardless of the initial superposition [31].

Lines on Fig. 35 are simulations that take into account detector dark counts, imperfect state initialization, different coupling strengths of the ions to the cavity and magnetic field fluctuations. The simulations, which have no free parameters, calculate the cavity field, which after being multiplied by the cavity decay κ and the detection path efficiency, result in the simulated detection probability. For simulations shown in Fig. 35, we have used a path detection efficiency of 8(1)%, the average of the detection path efficiency of the two channels given by Eq. 4.1. The simulations are in good agreement with the data.

For comparison, as in Section 8, we carry out reference measurements in which superradiant enhancement is not present. In this case, the qubit defined by α and β is encoded in one ion while the other remains hidden in the state $|D'\rangle$, which is not coupled to the Raman process. The mapping process is then given by

$$\begin{aligned} |0\rangle \left[\cos(\alpha) |S\rangle + \sin(\alpha) e^{i\beta} |S'\rangle \right] |D'\rangle / \sqrt{2} \\ \mapsto \left[\cos(\alpha) |H\rangle + e^{i\beta} \sin(\alpha) |V\rangle \right] |DD'\rangle. \end{aligned} \quad (9.7)$$

The process is characterized by calculating the fidelity χ_{00} as described above, but with the four orthogonal input states $|SD'\rangle$, $|S'D'\rangle$, $(|S\rangle - |S'\rangle) |D'\rangle / \sqrt{2}$ and $(|S\rangle + i|S'\rangle) |D'\rangle / \sqrt{2}$.

We now compare the process fidelity χ_{00} of the mapping process described by Eq. 9.4, the ‘‘superradiant case’’, with the mapping process described by Eq. 9.7, the ‘‘single-ion case’’. Fig. 36a shows the process fidelity χ_{00} for both cases as a function of the length of the photon detection time window. Not only is the fidelity of the superradiant case higher for all data points, but the improvement over the single-ion case also increases with the length of the detection window. For a detection time window of 6 μs , the fidelity of the superradiant case is 93.3(3)% while for the single-ion case it is 90.9(5)%, indicating that in both cases the logical qubit is correctly mapped onto photon polarization with very high probability. A maximum value of 96.0(3)% is found for the superradiant case considering photons detected between 2 and 4 μs (See Fig. 36c). Lines on Fig. 36a are simulations, which are in good agreement with the data.

As the length of the detection window is increased, χ_{00} decreases for both cases because the probability for off-resonant excitation to the $4^2P_{3/2}$ -manifold increases with time. As seen in Fig. 35, if such an event happens during the Raman process, the initial state is randomly mapped onto either $|H\rangle$ or $|V\rangle$, regardless of the information in the initial superposition. However, while the probability for scattering is the same for both states, photons are produced earlier

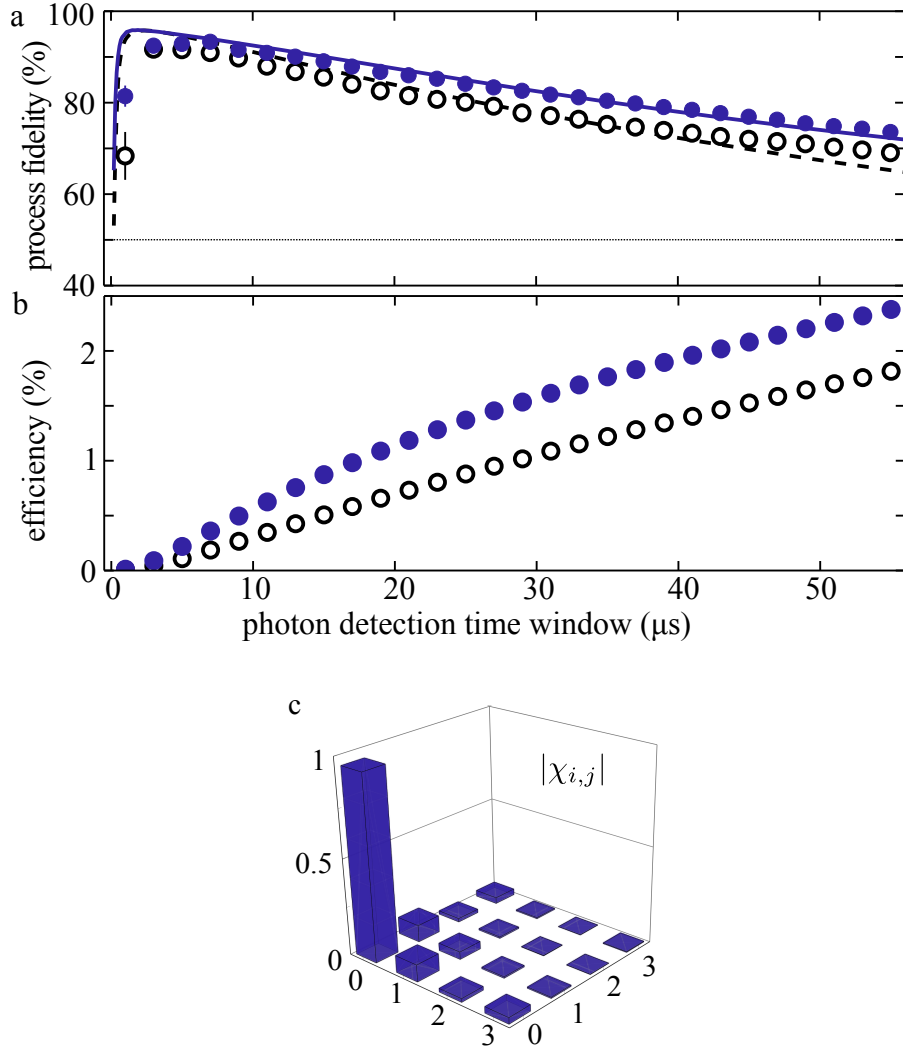


Figure 36: (a) Process fidelity for the superradiant case (filled blue circles) and for the single-ion case (open black circles) as a function of the length of the photon detection time window. Lines are simulations (continuous line: two entangled ions; dashed line: single-ion case). Error bars are derived from non-parametric bootstrapping. (b) Cumulative process efficiency for the superradiant case (filled blue circles) and for the single-ion case (open black circles) as a function of the photon detection time window. Error bars represent Poissonian statistics and are smaller than the plot symbols. (c) Absolute value of the process matrix χ_{ij} for the superradiant case reconstructed from photons detected between 2 and 4 μs , yielding the maximum process fidelity $|\chi_{00}| = 96.0(3)\%$. The figure has been taken from Ref. [46].

from the superradiant case because of the enhanced effective coupling. Thus, the improvement in the fidelity stems from an increased probability to generate a photon before scattering occurs. After $55 \mu\text{s}$, we find $\chi_{00} = 73.4(3)\%$ for the superradiant case in comparison with $68.7(2)\%$ for the single ion case.

We also investigate the cumulative process efficiency $\varepsilon(t)$, defined as the probability to detect a photon before time t (Fig. 36c). For $t = 6 \mu\text{s}$, the process efficiency for the superradiant case is $\varepsilon_s(t) = 0.33(1)\%$, while for single-ion case it is $\varepsilon_{\text{one}}(t) = 0.17(1)\%$, corresponding to a ratio $\varepsilon_s/\varepsilon_{\text{one}}$ of $1.94(13)$. The ratio decreases monotonically with t , and by $t = 55 \mu\text{s}$, it is $1.34(5)$. As discussed in Section 8.2.1, the enhanced coupling modifies the temporal shape of the photons early in the process. Therefore, for $t \approx 0$, the maximum ratio is expected to be two. For longer times, that is, $t \gg (g_{(1,2)}, \gamma_{\text{eff}}, \kappa)$, the probability that a photon is generated in both the single-ion and the superradiant case is expected to approach one. Therefore, for that time scale, the ratio is also expected to approach one.

9.6 Towards the enhanced reading process of a quantum memory

In the previous section, we have shown the implementation of Step III of the protocol described in Section 9.3, that is, the mapping of a qubit encoded in the superradiant state of a two-ion crystal onto a polarization degree of freedom of a single photon. In order to write the qubit in the superradiant state, we have not followed Steps I and II of the proposal. As a further project, it might be interesting to show the implementation of the whole protocol, that is, from Step I to the Step III. Such an experiment would demonstrate that collective effects can be used to enhance the reading process of a quantum memory, that is, the process of mapping the state of a single ion onto a single photon. In this section we discuss a possible sequence in order to perform Steps I and II in our setup.

Possible implementation of Step I

Assume that the addressing beam is aligned to the first ion. After optical pumping to the $|SS\rangle$ state, a qubit can be written on the first ion by applying a $\pi/2$ rotation on the $|S\rangle \leftrightarrow |D\rangle$ transition, an AC-Stark shift gate (see Section 5.9), and a second $\pi/2$ rotation on the same transition. As a result, the ions are in the state

$$(\sin(\alpha) |S\rangle + e^{i\beta} \cos(\alpha) |D\rangle) \otimes |D\rangle / \sqrt{2}, \quad (9.8)$$

in which the phase α is determined by the duration of the AC-Stark shift gate pulse, and β is determined by the relative phase between the two $\pi/2$ pulses.

Then, one needs to transfer the population of the state $|D\rangle$ of the first ion to the state $|S'\rangle$. We note that the addressing beam and the global beam are not phase stable; therefore, the addressing beam cannot be used for such a mapping. Otherwise, a random phase will be

introduced in the superposition, leading to decoherence. Such an operation is possible by first performing a π pulse on the $|D\rangle \leftrightarrow |S'\rangle$ transition using the addressing beam, but now aligned so that it interacts with the second ion. In such a case the random phase is global and does not play a role:

$$(\sin(\alpha) |S\rangle + e^{i\beta} \cos(\alpha) |D\rangle) \otimes |S'\rangle / \sqrt{2}. \quad (9.9)$$

Finally, a global π pulse on the $|D\rangle \leftrightarrow |S'\rangle$ transition generates the analogue of the state described in Eq. 9.1:

$$(\sin(\alpha) |S\rangle + e^{i\beta} \cos(\alpha) |S'\rangle) \otimes |D\rangle / \sqrt{2}. \quad (9.10)$$

Possible implementation of Step II

For Step II, two vibrational modes in the ground state are required. In Ref. [44] we reported that the axial and the radial modes can be cooled to the motional ground state.

Two processes that address the vibrational modes are involved in this step. The first one, a mapping process, is implemented only on the ion that contains the qubit. The mapping corresponds to a bichromatic blue-sideband transition

$$|0_r\rangle |S\rangle \leftrightarrow |1_r\rangle |D\rangle \quad \text{and} \quad |0_a\rangle |S'\rangle \leftrightarrow |1_a\rangle |D\rangle, \quad (9.11)$$

where $|1_{a,r}\rangle$ and $|0_{a,r}\rangle$ denote the phonon state of the axial and the radial vibrational modes. To perform the mapping using the global beam, one first needs to hide the second ion in a state $|D'\rangle$. The hiding can be performed by applying two consecutive π pulses using the addressing beam, first on the $|D\rangle \leftrightarrow |S'\rangle$ transition, and subsequently on the $|S'\rangle \leftrightarrow |D'\rangle$ transition,

$$|0_r 0_a\rangle (\sin(\alpha) |S\rangle + e^{i\beta} \cos(\alpha) |S'\rangle) |D'\rangle / \sqrt{2}. \quad (9.12)$$

After the first mapping, the system is in the state

$$(\sin(\alpha) |1_r 0_a\rangle + e^{i\beta} \cos(\alpha) |0_r 1_a\rangle) |DD'\rangle / \sqrt{2}. \quad (9.13)$$

Finally, we need to transfer the population of the state $|D'\rangle$ of the second ion back to the state $|D\rangle$. Again, two consecutive π pulses using the addressing beam, first on the $|D\rangle \leftrightarrow |S'\rangle$ transition, and subsequently on the $|S'\rangle \leftrightarrow |D'\rangle$ transition leave the system in the state

$$(\sin(\alpha) |1_r\rangle + e^{i\beta} \cos(\alpha) |1_a\rangle) |DD\rangle / \sqrt{2}. \quad (9.14)$$

The second process of Step II that address the vibrational modes corresponds to a $\pi/2$ pulse on the same bichromatic blue-sideband transition previously described (Eq. 9.11). The rotation is now applied to both ions, leaving the system in the analogous state to the one described in Eq. 9.2

$$\begin{aligned} & \left[(\sin(\alpha) |S\rangle + e^{i\beta} \cos(\alpha) |S'\rangle) |D\rangle + |D\rangle (\sin(\alpha) |S\rangle + e^{i\beta} \cos(\alpha) |S'\rangle) \right] / \sqrt{4} = \\ & = \left[\cos(\alpha) |\Psi_{\text{Dicke}}^a\rangle + e^{i\beta} \sin(\alpha) |\Psi_{\text{Dicke}}^b\rangle \right] / \sqrt{2} \end{aligned}$$

Finally, Step III as it has been performed in Section 9.5 can be implemented.

Consideration for the implementation of Steps I and II

Currently, such a procedure cannot be implemented in our setup as the position of the addressing beam cannot be shifted during the execution of a single experimental sequence. Modifications to the setup that would overcome such a limitation are discussed in Section 4.5.

Note that another combination of transitions might exist that, when applied, would produce the same states with the use of fewer pulses, or even without the necessity of changing the position of the addressing beam. In the proposed sequences, the duration of all 729 nm pulses is expected to be less than $50 \mu\text{s}$, one order of magnitude smaller than the coherence time for information stored in the $|S_{1/2}\rangle - |D_{1/2}\rangle$ qubit.

For the bichromatic mapping process required in Step II, the Rabi frequency of each transition should be the same. The Rabi frequencies are given by the power of the 729 nm beam and the Lamb-Dicke factors (see Section 5.8 for a discussion related to the Lamb-Dicke factors). Experimentally, one could adjust the power of each frequency component of the bichromatic beam so that the intensity difference matches the difference between Lamb-Dicke factors.

9.7 Conclusions

In Chapter 8, we show the creation of a superradiant state of two ions coupled to the optical cavity. In this chapter, we demonstrated that the superradiant state can be used to enhance the performance of a deterministic quantum interface that would allow the direct transmission of quantum information between two remote interfaces [2]. Using the superradiant state of two ions coupled to the optical cavity, we have enhanced the fidelity and efficiency of the quantum state transfer process. The enhancement in the fidelity and efficiency of the process can be understood in terms of a stronger effective ion–cavity coupling.

Further improvements are thus expected by encoding the logical qubit across more physical qubits. As discussed in Section 6.4, the geometry of our setup sets a limit on the number of ions that could be coupled to the optical cavity, so in practice, one would need a different setup, ideally with the cavity axis parallel to the trap axis. A planar microfabricated trap has been constructed at MIT in which it is expected that 1000 ions can be coupled to the cavity [134].

Maximum enhancement would be achieved by encoding not just one but $N/2$ excitations in a symmetrized N -ion state. The cooperative emission rate would then be $g\sqrt{\frac{N}{2}(\frac{N}{2} + 1)}$, which scales with N for large N , as observed in atomic ensembles [38–40]. However, it remains an open question how to transfer quantum information between such states and single photons, as required for a quantum transducer [36].

10 Summary and Outlook

The results presented in this thesis work contribute to the development of quantum networks and distributed quantum computing [2–4], first because we demonstrate a protocol that can be extended to generate entanglement of ion-based quantum computers using cavity-based quantum interfaces [45], and second because we show that collective effects can be used to enhance the performance of a cavity-based interface [36, 46].

The experiments described in this thesis have been performed using two trapped ions inside an optical cavity. First, it was necessary to develop a procedure to control the coupling strength of each ion to the cavity. We demonstrated two configurations: in the first one, the two ions were equally and near-maximally coupled; in the second, one ion was maximally coupled while the other was decoupled. This achievement was possible due to, first, the small spatial localization of a Doppler-cooled ion as compared to a quarter-wavelength of the cavity field [76], and second, the capability to displace the cavity with respect to the ions with a resolution on the order of tens of nanometers.

Using the configuration in which the two ions were equally and maximally coupled to the cavity, we entangled the ions using the cavity. The entanglement generation using this protocol is efficient and heralded, and as the protocol does not rely on the fact that the ions are located in the same ion trap, it can be extended to generate entangle remote ions. Two remote ions have been entangled by means of heralded quantum interfaces [14, 23]; however, entanglement of remote ions interacting with cavities, remains a goal for the community.

To show enhancement in the performance of a cavity-based interface, we integrated a set of tools that allowed us to carry out quantum logic operations: The Mølmer–Sørensen gate and the AC-Stark shift gate. This experiment required a tunable entangled state of two ions inside the optical cavity. While the generation of the entanglement could have been mediated by the optical cavity, the Mølmer–Sørensen gate offered higher repetition rates and deterministic entanglement with a fidelity of 95(2)%. The implementation of the Mølmer–Sørensen gate and the AC-Stark shift gate in our setup allowed us to generate any desired two-ion state.

Along the path to improve the cavity-based quantum interface, we explored two fundamental quantum optics effects: subradiance and superradiance [35]. These effects have been widely studied in ensembles of atoms [37–40] and artificial qubits [135, 136], but so far, only one key experiment has explored a configuration using two atoms. Using a two-ion system and a high-numerical-aperture lens, DeVoe et al. showed a suppression of 1.2(9)% and an enhancement of 1.5(8)% in the excited-state lifetime, mainly limited by the fact that the ion–ion separation was on the order of the wavelength of the radiated field [41]. Here, we created sub- and superradiant states of two ions coupled to the optical cavity. The optical cavity provided the photon indistinguishability required to observe sub- and superradiance, even though the ion–ion separation is much larger than the wavelength of the radiated field. We measured a maximum suppression of 78(9)% in the probability of generating a single photon in the cavity compared with the

single-ion case, and a maximum enhancement of $84(4)\%$, also compared with the single ion case.

A two-ion intracavity superradiant state was the first step towards the demonstration that collective effects can be used to enhance the performance of a cavity-based quantum interface [36]. For this demonstration, we have encoded a single logical qubit of information in the superradiant state and transferred it to a single photon. We compared the efficiency and fidelity of this process with the efficiency and fidelity of single-ion state transfer and we have shown that both were enhanced.

The current setup is well-suited for many key experiments in quantum information science. In this thesis, we have shown the implementation of one of three steps in the ion-crystal transducer protocol [36]. I suggest the implementation of the full protocol, which would correspond to an enhanced reading process of a quantum memory (Section 9.6). Another key experiment is the generation of entanglement of two ions using a dissipative process [118]. In the proposed experiment, the dissipative channel is the optical cavity, through which the superradiant component of the separable state dissipates leaving the two ions in the subradiant state, which is decoupled from the channel. Finally, also using two ions, we plan to generate a two-dimensional cluster state of photons, a state which is the universal source of measurement-based quantum computation [105, 137].

Our setup would allow us to couple four ions to the optical cavity with an estimated reduction of 30% in the coupling strength for the two outer ions of the string (Section 6.4). Four ions can be used to further increase the performance of the quantum interface using the ion-state mapping protocol, as it has been done in (Section 9). Additionally, also using four ions, two pairs of ions can each be prepared in a superradiant state. Then, the two superradiant states can be entangled with one another via the cavity using the heralded protocol described in Chapter 7. In such a way, an increased fidelity of the entangled state is expected due to the enhanced coupling strength that each superradiant state exhibits.

Currently, a second interface is being constructed [80]. The new setup consists of to a fiber-based optical cavity integrated with an ion trap. The system is expected to operate in the strong-coupling regime, allowing the investigation of novel effects in an ion-cavity system, such as the vacuum Rabi splitting [67], photon blockade [68], gates between photons and ions [69, 70] and cavity cooling [71].

By connecting the two setups, we would realize a quantum network. In order to perform the interconnection using photons efficiently, the temporal waveform of the photons generated in both setups should be as similar as possible. The temporal waveform is determined by the intensity of the Raman beam, the cavity decay rate, the detuning of the Raman transition, and the ion-cavity coupling strength. As the setups are intended to access different parameter regimes, it might not be trivial to match the photon shape. In order to do this, we could vary the intensity

of the Raman beam during the process [84]. Additionally, effective coupling strength of the current setup can be enhanced by means of collective effects as shown in this thesis work.

Once photons generated in both setups are indistinguishable, the two-ion entanglement protocol presented in this thesis can be extended to generate entanglement between two ions, each of which is located in one of the cavities. An alternative approach to entanglement generation is via the direct transmission of information between the two ions using photons [2, 21]. Ion-photon state mapping, the building block of such a protocol, has been implemented in our setup [31]; the reverse process, however, has not. In order to do that, ion-photon state mapping could be performed twice in a row: first, to map the state of the ion onto a photon, second, to map the state of the photon back onto the ion. In between the two processes, one would need to delay the photon for $5 - 10 \mu\text{s}$ due to the temporal extension of the photon wavepacket. Such a delay can be performed using $1,500 - 3,000$ meters of optical fiber. Note that the qubit encoded in the polarization degree of freedom of the photon should be preserved. After the photons leave the cavity; they can be split according to polarization, coupled to polarization-maintaining fibers, and recombined before being injected back into the cavity.

Once entanglement between two remote ions is demonstrated, one could build an ion-based quantum network (Fig. 25). Such ion-based quantum networks can be used to distribute, for the first time, a quantum calculation or a quantum simulation.

Journal publications

The work of this thesis resulted in the following publications:

- **B. Casabone**, K. Friebe, B. Brandstätter, K. Schüppert, R. Blatt, T. E. Northup.
“Enhanced quantum interface with collective ion-cavity coupling”
Phys. Rev. Lett. 114, 023602 (2015)
- B. Brandstätter, A. McClung, K. Schüppert, **B. Casabone**, K. Friebe, A. Stute, P. O. Schmidt, C. Deutsch, J. Reichel, R. Blatt, T. E. Northup.
“Integrated fiber-mirror ion trap for strong ion-cavity coupling”
Rev. Sci. Instrum. 84, 123104 (2013)
- **B. Casabone**, A. Stute, K. Friebe, B. Brandstätter, K. Schüppert, R. Blatt, T. E. Northup.
“Heralded entanglement of two ions in an optical cavity”
Phys. Rev. Lett. 111, 100505 (2013)
- A. Stute, **B. Casabone**, B. Brandstätter, K. Friebe, T. E. Northup, R. Blatt.
“Quantum-state transfer from an ion to a photon”
Nature Photon. 7, 219 (2013)
- A. Stute, **B. Casabone**, P. Schindler, T. Monz, P. O. Schmidt, B. Brandstätter, T. E. Northup, R. Blatt.
“Tunable ion-photon entanglement in an optical cavity”
Nature 485, 482 (2012)
- A. Stute, **B. Casabone**, B. Brandstätter, D. Habicher, H. G. Barros, P. O. Schmidt, T. E. Northup, R. Blatt.
“Toward an ion-photon quantum interface in an optical cavity”
Appl. Phys. B 107, 1145 (2012)

References

- [1] D. P. DiVincenzo. The physical implementation of quantum computation. *Fortschr. Phys.*, 48:771–783, 2000.
- [2] J. I. Cirac, P. Zoller, H. J. Kimble, and H. Mabuchi. Quantum state transfer and entanglement distribution among distant nodes in a quantum network. *Phys. Rev. Lett.*, 78:3221–3224, 1997.
- [3] H. J. Kimble. The quantum internet. *Nature*, 453(7198):1023–1030, 2008.
- [4] T. E. Northup and R. Blatt. Quantum information transfer using photons. *Nature Photonics*, 8(5):356–363, 2014.
- [5] Immanuel Bloch. Ultracold quantum gases in optical lattices. *Nature Physics*, 1(1):23–30, 2005.
- [6] Immanuel Bloch, Jean Dalibard, and Sylvain Nascimbène. Quantum simulations with ultracold quantum gases. *Nature Physics*, 8(4):267–276, 2012.
- [7] K. Kim, M.S. Chang, S. Korenblit, R. Islam, EE Edwards, JK Freericks, G.D. Lin, L.M. Duan, and C. Monroe. Quantum simulation of frustrated Ising spins with trapped ions. *Nature*, 465(7298):590–593, 2010.
- [8] R. Gerritsma, G. Kirchmair, F. Zähringer, E. Solano, R. Blatt, and C. F. Roos. Quantum simulation of the Dirac equation. *Nature*, 463(7277):68–71, 2010.
- [9] B. P. Lanyon, C. Hempel, D. Nigg, M. Müller, R. Gerritsma, F. Zähringer, P. Schindler, J. T. Barreiro, M. Rambach, G. Kirchmair, et al. Universal digital quantum simulation with trapped ions. *Science*, 334(6052):57–61, 2011.
- [10] R. J. Schoelkopf and S. M. Girvin. Wiring up quantum systems. *Nature*, 451(7179):664–669, 2008.
- [11] Emanuel Knill, Raymond Laflamme, and Gerald J Milburn. A scheme for efficient quantum computation with linear optics. *Nature*, 409(6816):46–52, 2001.
- [12] B. B. Blinov, D. L. Moehring, L. M. Duan, and C. Monroe. Observation of entanglement between a single trapped atom and a single photon. *Nature*, 428:153–157, 2004.
- [13] Jürgen Volz, Markus Weber, Daniel Schlenk, Wenjamin Rosenfeld, Johannes Vrana, Karen Saucke, Christian Kurtsiefer, and Harald Weinfurter. Observation of entanglement of a single photon with a trapped atom. *Phys. Rev. Lett.*, 96(3):030404, 2006.

- [14] D. Hucul, I. V. Inlek, G. Vittorini, C. Crocker, S. Debnath, S. M. Clark, and C. Monroe. Modular entanglement of atomic qubits using photons and phonons. *Nature Physics*, 11:37–42, 2014.
- [15] T. Wilk, S. C. Webster, A. Kuhn, and G. Rempe. Single-atom single-photon quantum interface. *Science*, 317:488–490, 2007.
- [16] J. McKeever, A. Boca, A. D. Boozer, R. Miller, J. R. Buck, A. Kuzmich, and H. J. Kimble. Deterministic generation of single photons from one atom trapped in a cavity. *Science*, 303:1992–1994, 2004.
- [17] H. G. Barros, A. Stute, T. E. Northup, C. Russo, P. O. Schmidt, and R. Blatt. Deterministic single-photon source from a single ion. *New J. Phys.*, 11(10):103004, 2009.
- [18] C. Cabrillo, J. I. Cirac, P. García-Fernández, and P. Zoller. Creation of entangled states of distant atoms by interference. *Phys. Rev. A*, 59(2):1025–1033, February 1999.
- [19] L.-M. Duan and H. J. Kimble. Efficient engineering of multiatom entanglement through single-photon detections. *Phys. Rev. Lett.*, 90:253601, 2003.
- [20] Christoph Simon and William T. M. Irvine. Robust long-distance entanglement and a loophole-free Bell test with ions and photons. *Phys. Rev. Lett.*, 91(11):110405, September 2003.
- [21] S. Ritter, C. Nölleke, C. Hahn, A. Reiserer, A. Neuzner, M. Uphoff, M. Mücke, E. Figueroa, J. Bochmann, and G. Rempe. An elementary quantum network of single atoms in optical cavities. *Nature*, 484:195–200, 2012.
- [22] S. Olmschenk, D. N. Matsukevich, P. Maunz, D. Hayes, L.-M. Duan, and C. Monroe. Quantum teleportation between distant matter qubits. *Science*, 323(5913):486–489, 2009.
- [23] D. L. Moehring, P. Maunz, S. Olmschenk, K. C. Younge, D. N. Matsukevich, L. M. Duan, and C. Monroe. Entanglement of single-atom quantum bits at a distance. *Nature*, 449(7158):68–71, 2007.
- [24] Julian Hofmann, Michael Krug, Norbert Ortengel, Lea Gérard, Markus Weber, Wenjamin Rosenfeld, and Harald Weinfurter. Heralded entanglement between widely separated atoms. *Science*, 337(6090):72–75, 2012.
- [25] M. Lettner, M. Mücke, S. Riedl, C. Vo, C. Hahn, S. Baur, J. Bochmann, S. Ritter, S. Dürr, and G. Rempe. Remote entanglement between a single atom and a Bose-Einstein condensate. *Phys. Rev. Lett.*, 106(21):210503, May 2011.

- [26] C. W. Chou, H. de Riedmatten, D. Felinto, S. V. Polyakov, S. J. van Enk, and H. J. Kimble. Measurement-induced entanglement for excitation stored in remote atomic ensembles. *Nature*, 438:828–832, 2005.
- [27] D. N. Matsukevich, Thierry Chaneliere, S. D. Jenkins, S. Y. Lan, T. A. B. Kennedy, and Alex Kuzmich. Entanglement of remote atomic qubits. *Physical review letters*, 96(3):030405, 2006.
- [28] H. Häffner, C.F. Roos, and R. Blatt. Quantum computing with trapped ions. *Phys. Rep.*, 469(4):155–203, 2008.
- [29] Carlos Manuel Russo. *Photon statistics of a single ion coupled to a high-finesse cavity*. PhD thesis, Leopold-Franzens-Universität Innsbruck, October 2008.
- [30] A. Stute, B. Casabone, P. Schindler, T. Monz, P. O. Schmidt, B. Brandstätter, T. E. Northup, and R. Blatt. Tunable ion-photon entanglement in an optical cavity. *Nature*, 485(7399):482–485, 2012.
- [31] A. Stute, B. Casabone, B. Brandstätter, K. Friebe, T. E. Northup, and R. Blatt. Quantum-state transfer from an ion to a photon. *Nature Photon.*, 7:219–222, 2013.
- [32] E. Hagley, X. Maître, G. Nogues, C. Wunderlich, M. Brune, J. M. Raimond, and S. Haroche. Generation of einstein-podolsky-rosen pairs of atoms. *Phys. Rev. Lett.*, 79(1):1–5, July 1997.
- [33] S. Osnaghi, P. Bertet, A. Auffeves, P. Maioli, M. Brune, J. M. Raimond, and S. Haroche. Coherent control of an atomic collision in a cavity. *Phys. Rev. Lett.*, 87(3):037902, June 2001.
- [34] B. U. Brandstätter. *Integration of fiber mirrors and ion traps for a high-fidelity quantum interface*. PhD thesis, Leopold-Franzens-Universität Innsbruck, 2013.
- [35] R. H. Dicke. Coherence in spontaneous radiation processes. *Phys. Rev.*, 93(1):99–110, January 1954.
- [36] L. Lamata, D. R. Leibbrandt, I. L. Chuang, J. I. Cirac, M. D. Lukin, V. Vuletić, and S. F. Yelin. Ion crystal transducer for strong coupling between single ions and single photons. *Phys. Rev. Lett.*, 107:030501, July 2011.
- [37] Michael Scheibner, Thomas Schmidt, Lukas Worschech, Alfred Forchel, Gerd Bacher, Thorsten Passow, and Detlef Hommel. Superradiance of quantum dots. *Nature Physics*, 3(2):106–110, 2007.

- [38] K. Baumann, C. Guerlin, F. Brennecke, and T. Esslinger. Dicke quantum phase transition with a superfluid gas in an optical cavity. *Nature*, 464(7293):1301–1306, 2010.
- [39] Markus P. Baden, Kyle J. Arnold, Arne L. Grimsmo, Scott Parkins, and Murray D. Barrett. Realization of the Dicke model using cavity-assisted Raman transitions. 2014.
- [40] Justin G. Bohnet, Zilong Chen, Joshua M. Weiner, Dominic Meiser, Murray J. Holland, and James K. Thompson. A steady-state superradiant laser with less than one intracavity photon. *Nature*, 484(7392):78–81, 2012.
- [41] R. G. DeVoe and R. G. Brewer. Observation of superradiant and subradiant spontaneous emission of two trapped ions. *Phys. Rev. Lett.*, 76(12):2049–2052, March 1996.
- [42] C. Russo, H. G. Barros, A. Stute, F. Dubin, E. S. Phillips, T. Monz, T. E. Northup, C. Becher, T. Salzburger, H. Ritsch, P. O. Schmidt, and R. Blatt. Raman spectroscopy of a single ion coupled to a high-finesse cavity. *Appl. Phys. B*, 95(2):205–212, 05 2009.
- [43] F. Dubin, C. Russo, H.G. Barros, A. Stute, C. Becher, P.O. Schmidt, and R. Blatt. Quantum to classical transition in a single-ion laser. *Nat. Phys.*, 6(5):350–353, 2010.
- [44] A. Stute, B. Casabone, B. Brandstätter, D. Habicher, P. O. Schmidt, T. E. Northup, and R. Blatt. Toward an ion-photon quantum interface in an optical cavity. *Appl. Phys. B*, 107(4):1145–1157, 2012.
- [45] B. Casabone, A. Stute, K. Friebe, B. Brandstätter, K. Schüppert, R. Blatt, and T. E. Northup. Heralded entanglement of two ions in an optical cavity. *Physical Review Letters*, 111(10):100505, 2013.
- [46] B. Casabone, K. Friebe, B. Brandstätter, K. Schüppert, R. Blatt, and T. E. Northup. Enhanced quantum interface with collective ion-cavity coupling. *Physical Review Letters*, 114(2):023602, 2015.
- [47] Rainer Blatt and David Wineland. Entangled states of trapped atomic ions. *Nature*, 453(7198):1008–1015, 06 2008.
- [48] J. Benhelm, G. Kirchmair, R. Gerritsma, F. Zähringer, T. Monz, P. Schindler, M. Chwalla, W. Hänsel, M. Hennrich, C. F. Roos, et al. Ca⁺ quantum bits for quantum information processing. *Physica Scripta*, 2009(T137):014008, 2009.
- [49] S. Gulde, D. Rotter, P. Barton, F. Schmidt-Kaler, R. Blatt, and W. Hogervorst. Simple and efficient photo-ionization loading of ions for precision ion-trapping experiments. *Appl. Phys. B*, 73(8):861–863, 2001.

- [50] Wolfgang Paul, Otto Osberghaus, and Erhardt Fischer. Ein ionenkäfig. Technical Report 415, 1958.
- [51] D. Wineland and H. G. Dehmelt. Proposed $10^{14} d\nu < \nu$ laser fluorescence spectroscopy on Ti^+ mono-ion oscillator III (spontaneous quantum jumps). *Bull. Am. Phys. Soc.*, 20(637), 1975.
- [52] T.W. Hänsch and A.L. Schawlow. Cooling of gases by laser radiation. *Optics Communications*, 13(1):68 – 69, 1975.
- [53] D. Leibfried, R. Blatt, C. Monroe, and D. Wineland. Quantum dynamics of single trapped ions. *Rev. Mod. Phys.*, 75:281–324, 2003.
- [54] Florian Mintert and Christof Wunderlich. Ion-trap quantum logic using long-wavelength radiation. *Phys. Rev. Lett.*, 87:257904, Nov 2001.
- [55] Jian Jin and D. A. Church. Precision lifetimes for the Ca^+ $4p^2P$ levels: Experiment challenges theory at the 1% level. *Phys. Rev. Lett.*, 70(21):3213–3216, May 1993.
- [56] D.F.V. James. Quantum dynamics of cold trapped ions with application to quantum computation. *Appl. Phys. B*, 66(2):181–190, 1998.
- [57] P. A. Barton, C. J. S. Donald, D. M. Lucas, D. A. Stevens, A. M. Steane, and D. N. Stacey. Measurement of the lifetime of the $3d^2D_{5/2}$ state in $^{40}\text{Ca}^+$. *Phys. Rev. A*, 62(3):032503, August 2000.
- [58] J. I. Cirac and P. Zoller. Quantum computations with cold trapped ions. *Phys. Rev. Lett.*, 74(20):4091–4094, May 1995.
- [59] F. Schmidt-Kaler, H. Häffner, M. Riebe, S. Gulde, G. P. T. Lancaster, T. Deuschle, C. Becher, C. F. Roos, J. Eschner, and R. Blatt. Realization of the Cirac-Zoller controlled-NOT quantum gate. *Nature*, 422:408–411, 2003.
- [60] Anders Sørensen and Klaus Mølmer. Quantum computation with ions in thermal motion. *Phys. Rev. Lett.*, 82:1971–1974, March 1999.
- [61] J. Benhelm, G. Kirchmair, C. F. Roos, and R. Blatt. Towards fault-tolerant quantum computing with trapped ions. *Nat. Phys.*, 4:463–466, 2008.
- [62] M. Chwalla, J. Benhelm, K. Kim, G. Kirchmair, T. Monz, M. Riebe, P. Schindler, A. S. Villar, W. Hänsel, C. F. Roos, R. Blatt, M. Abgrall, G. Santarelli, G. D. Rovera, and Ph. Laurent. Absolute frequency measurement of the $^{40}\text{Ca}^+$ $4s^2S_{1/2} - 3d^2D_{5/2}$ clock transition. *Phys. Rev. Lett.*, 102(2):023002, January 2009.

- [63] H. G. Dehmelt. Proposed $10^{14} d\nu < \nu$ laser fluorescence spectroscopy on Tl^+ mono-ion oscillator II (spontaneous quantum jumps). *Bull. Am. Phys. Soc.*, 20(637), 1975.
- [64] Pieter Kok, W. J. Munro, Kae Nemoto, T. C. Ralph, Jonathan P. Dowling, and G. J. Milburn. Linear optical quantum computing with photonic qubits. *Rev. Mod. Phys.*, 79:135–174, Jan 2007.
- [65] C.K. Law and H.J. Kimble. Deterministic generation of a bit-stream of single-photon pulses. *J. Mod. Opt.*, 44:2067–2074(8), 1997.
- [66] Q. A. Turchette, C. J. Hood, W. Lange, H. Mabuchi, and H. J. Kimble. Measurement of conditional phase shifts for quantum logic. *Phys. Rev. Lett.*, 75(25):4710–4713, December 1995.
- [67] A. Boca, R. Miller, K. M. Birnbaum, A. D. Boozer, J. McKeever, and H. J. Kimble. Observation of the vacuum Rabi spectrum for one trapped atom. *Phys. Rev. Lett.*, 93(23):233603, December 2004.
- [68] Kevin Michael Birnbaum. *Cavity QED with multilevel atoms*. PhD thesis, California Institute of Technology, 2005.
- [69] T. G. Tiecke, Jeffrey Douglas Thompson, Nathalie Pulmones de Leon, L. R. Liu, V. Vuletić, and Mikhail D. Lukin. Nanophotonic quantum phase switch with a single atom. *Nature*, 508(7495):241–244, 2014.
- [70] Andreas Reiserer, Norbert Kalb, Gerhard Rempe, and Stephan Ritter. A quantum gate between a flying optical photon and a single trapped atom. *Nature*, 508(7495):237–240, 2014.
- [71] Peter Horak, Gerald Hechenblaikner, Klaus M. Gheri, Herwig Stecher, and Helmut Ritsch. Cavity-induced atom cooling in the strong coupling regime. *Phys. Rev. Lett.*, 79(25):4974–4977, December 1997.
- [72] Christian Felix Roos. *Controlling the quantum state of trapped ions*. PhD thesis, Leopold-Franzens-Universität Innsbruck, February 2000.
- [73] A. B. Mundt. *Cavity QED with Single Trapped Ions*. PhD thesis, Leopold-Franzens-Universität Innsbruck, 2003.
- [74] A. Kreuter, C. Becher, G. P. T. Lancaster, A. B. Mundt, C. Russo, H. Häffner, C. Roos, J. Eschner, F. Schmidt-Kaler, and R. Blatt. Spontaneous emission lifetime of a single trapped Ca^+ ion in a high finesse cavity. *Phys. Rev. Lett.*, 92:203002, 2004.

- [75] Axel Kreuter. *Spontaneous Emission of a Single Trapped Ca^+ -Ion*. PhD thesis, Leopold-Franzens-Universität Innsbruck, September 2004.
- [76] A. Stute. *A light-matter quantum interface: ion-photon entanglement and state mapping*. PhD thesis, Leopold-Franzens-Universität Innsbruck, 2012.
- [77] M. Keller, B. Lange, K. Hayasaka, W. Lange, and H. Walther. Deterministic coupling of single ions to an optical cavity. *Appl. Phys. B*, 76(2):125–128, 2003.
- [78] G. R. Guthöhrlein, M. Keller, K. Hayasaka, W. Lange, and H. Walther. A single ion as a nanoscopic probe of an optical field. *Nature*, 414:49–51, 2001.
- [79] Matthias Steiner, Hendrik M. Meyer, Christian Deutsch, Jakob Reichel, and Michael Köhl. Single ion coupled to an optical fiber cavity. *Phys. Rev. Lett.*, 110(4):043003, January 2013.
- [80] B. Brandstätter, A. McClung, K. Schüppert, B. Casabone, K. Friebe, A. Stute, P. O. Schmidt, C. Deutsch, J. Reichel, R. Blatt, and T. E. Northup. Integrated fiber-mirror ion trap for strong ion-cavity coupling. *Rev. Sci. Instrum.*, 84(12):–, 2013.
- [81] Christopher C. Gerry and J. H. Eberly. Dynamics of a raman coupled model interacting with two quantized cavity fields. *Phys. Rev. A*, 42(11):6805–6815, December 1990.
- [82] Moorad Alexanian and Subir K. Bose. Unitary transformation and the dynamics of a three-level atom interacting with two quantized field modes. *Phys. Rev. A*, 52(3):2218–2224, September 1995.
- [83] Ying Wu. Effective raman theory for a three-level atom in the λ configuration. *Phys. Rev. A*, 54(2):1586–1592, August 1996.
- [84] M. Keller, B. Lange, K. Hayasaka, W. Lange, and H. Walther. Continuous generation of single photons with controlled waveform in an ion-trap cavity system. *Nature*, 431:1075–1078, 2004.
- [85] E. T. Jaynes and F. W. Cummings. Comparison of quantum and semiclassical radiation theories with application to the beam maser. *Proc. IEEE*, 51:89, 1963.
- [86] C. Cohen Tannoudji, C. Dupont-Roc, and J. Grynberg. *Atom photon interactions: Basic processes and applications*. 1992.
- [87] Axel Kuhn, Markus Hennrich, and Gerhard Rempe. Deterministic single-photon source for distributed quantum networking. *Phys. Rev. Lett.*, 89(6):067901, July 2002.

- [88] D. Habicher. Abbildung, Adressierung und Zustandsdetektion zweier Ionen in einem optischen Resonator. Master's thesis, Leopold-Franzens-Universität Innsbruck, 2012.
- [89] M. Brownnutt, M. Kumph, P. Rabl, and R. Blatt. Ion-trap measurements of electric-field noise near surfaces. *arXiv preprint arXiv:1409.6572*, 2014.
- [90] Florian Zähringer. *Quantum walks and relativistic quantum simulations with trapped ions*. PhD thesis, Leopold-Franzens-Universität Innsbruck, 2012.
- [91] Helena Gonçalves de Barros. *Raman spectroscopy and single-photon source in an ion-cavity system*. PhD thesis, Leopold-Franzens-Universität Innsbruck, January 2010.
- [92] Long-Sheng Ma, Peter Jungner, Jun Ye, and John L. Hall. Delivering the same optical frequency at two places: accurate cancellation of phase noise introduced by an optical fiber or other time-varying path. *Opt. Lett.*, 19(21):1777–1779, November 1994.
- [93] Thomas Monz, Philipp Schindler, Julio T. Barreiro, Michael Chwalla, Daniel Nigg, William A. Coish, Maximilian Harlander, Wolfgang Hänsel, Markus Hennrich, and Rainer Blatt. 14-qubit entanglement: creation and coherence. *Phys. Rev. Lett.*, 106(13):130506, March 2011.
- [94] Thomas Monz. *Quantum information processing beyond ten-ion qubits*. PhD thesis, Leopold-Franzens-Universität Innsbruck, August 2011.
- [95] Philipp Schindler, Daniel Nigg, Thomas Monz, Julio T Barreiro, Esteban Martinez, Shannon X Wang, Stephan Quint, Matthias F Brandl, Volckmar Nebendahl, Christian F Roos, et al. A quantum information processor with trapped ions. *New J. Phys.*, 15(12):123012, 2013.
- [96] Mark Kasevich and Steven Chu. Laser cooling below a photon recoil with three-level atoms. *Physical review letters*, 69(12):1741, 1992.
- [97] G. Alzetta, A. Gozzini, L. Moi, and G. Orriols. An experimental method for the observation of r.f. transitions and laser beat resonances in oriented na vapour. *Il Nuovo Cimento B (1971-1996)*, 36(1):5–20, 1976. 10.1007/BF02749417.
- [98] J. Eschner, G. Morigi, F. Schmidt-Kaler, R. Blatt, et al. Laser cooling of trapped ions. *JOSA B*, 20(5):1003–1015, 2003.
- [99] A. H. Myerson, D. J. Szwer, S. C. Webster, D. T. C. Allcock, M. J. Curtis, G. Imreh, J. A. Sherman, D. N. Stacey, A. M. Steane, and D. M. Lucas. High-fidelity readout of trapped-ion qubits. *Phys. Rev. Lett.*, 100(20):200502, May 2008.

- [100] W. M. Itano, J. C. Bergquist, J. J. Bollinger, J. M. Gilligan, D. J. Heinzen, F. L. Moore, M. G. Raizen, and D. J. Wineland. Quantum projection noise: Population fluctuations in two-level systems. *Phys. Rev. A*, 47(5):3554–3570, May 1993.
- [101] T. Andrew Manning. *Quantum information processing with trapped ion chains*. PhD thesis, Joint Quantum Institute, University of Maryland Department of Physics and National Institute of Standards and Technology, 2014.
- [102] Cornelius Hempel. *Digital quantum simulation, Schrödinger cat state spectroscopy and setting up a linear ion trap*. PhD thesis, Leopold-Franzens-Universität Innsbruck, 2014.
- [103] D. J. Wineland, C. Monroe, W. M. Itano, D. Leibfried, B. E. King, and D. M. Meekhof. Experimental issues in coherent quantum-state manipulation of trapped atomic ions. *J. Res. Natl. Inst. Stand. Technol.*, 103:259–328, 1998.
- [104] J. Benhelm. *Precision Spectroscopy and Quantum Information Processing with Trapped Calcium Ions*. PhD thesis, Leopold-Franzens-Universität Innsbruck, 2004.
- [105] Sophia E. Economou, Netanel Lindner, and Terry Rudolph. Optically generated 2-dimensional photonic cluster state from coupled quantum dots. *Phys. Rev. Lett.*, 105(9):093601, August 2010.
- [106] Almut Beige, Daniel Braun, Ben Tregenna, and Peter L. Knight. Quantum computing using dissipation to remain in a decoherence-free subspace. *Phys. Rev. Lett.*, 85(8):1762–1765, August 2000.
- [107] Michael Johanning, Andres F. Varon, and Christof Wunderlich. Quantum simulations with cold trapped ions. *Journal of Physics B: Atomic, Molecular and Optical Physics*, 42(15):154009, 2009.
- [108] René Reimann, Wolfgang Alt, Tobias Kampschulte, Tobias Macha, Lothar Ratschbacher, Natalie Thau, Seokchan Yoon, and Dieter Meschede. Cavity-modified super- and sub-radiant rayleigh scattering of two atoms. *arXiv preprint arXiv:1408.5874*, 2014.
- [109] Andreas Reiserer, Christian Nölleke, Stephan Ritter, and Gerhard Rempe. Ground-state cooling of a single atom at the center of an optical cavity. *Phys. Rev. Lett.*, 110(22):223003, May 2013.
- [110] A Kubanek, M Koch, C Sames, A Ourjoumtsev, T Wilk, PWH Pinkse, and G Rempe. Feedback control of a single atom in an optical cavity. *Applied Physics B*, 102(3):433–442, 2011.
- [111] Wolfgang Paul. Electromagnetic traps for charged and neutral particles. *Rev. Mod. Phys.*, 62(3):531–540, July 1990.

- [112] Liang Jiang, Jacob M. Taylor, Anders S. Sørensen, and Mikhail D. Lukin. Distributed quantum computation based on small quantum registers. *Phys. Rev. A*, 76(6):062323, December 2007.
- [113] Nicolas Schlosser, Georges Reymond, Igor Protsenko, and Philippe Grangier. Sub-poissonian loading of single atoms in a microscopic dipole trap. *Nature*, 411(6841):1024–1027, 2001.
- [114] Axel Griesmaier, Jörg Werner, Sven Hensler, Jürgen Stuhler, and Tilman Pfau. Bose-einstein condensation of chromium. *Phys. Rev. Lett.*, 94:160401, Apr 2005.
- [115] P. Maunz, S. Olmschenk, D. Hayes, D. N. Matsukevich, L.-M. Duan, and C. Monroe. Heralded quantum gate between remote quantum memories. *Phys. Rev. Lett.*, 102:250502, June 2009.
- [116] T. Pellizzari, S. A. Gardiner, J. I. Cirac, and P. Zoller. Decoherence, continuous observation, and quantum computing: A cavity QED model. *Phys. Rev. Lett.*, 75(21):3788–3791, November 1995.
- [117] Shi-Biao Zheng and Guang-Can Guo. Efficient scheme for two-atom entanglement and quantum information processing in cavity QED. *Phys. Rev. Lett.*, 85(11):2392–2395, September 2000.
- [118] K. Härkönen, F. Plastina, and S. Maniscalco. Dicke model and environment-induced entanglement in ion-cavity QED. *Phys. Rev. A*, 80(3):033841, September 2009.
- [119] M. J. Kastoryano, F. Reiter, and A. S. Sørensen. Dissipative preparation of entanglement in optical cavities. *Phys. Rev. Lett.*, 106(9):090502, February 2011.
- [120] J. Busch, S. De, S. S. Ivanov, B. T. Torosov, T. P. Spiller, and A. Beige. Cooling atom-cavity systems into entangled states. *Phys. Rev. A*, 84(2):022316, August 2011.
- [121] CA Sackett, D. Kielpinski, BE King, C. Langer, V. Meyer, CJ Myatt, M. Rowe, QA Turchette, WM Itano, DJ Wineland, et al. Experimental entanglement of four particles. *Nature*, 404(6775):256–259, 2000.
- [122] L. Slodička, G. Hétet, N. Röck, P. Schindler, M. Hennrich, and R. Blatt. Atom-atom entanglement by single-photon detection. *Phys. Rev. Lett.*, 110(8):083603, February 2013.
- [123] Sze M Tan. A computational toolbox for quantum and atomic optics. *J. Opt. B: Quantum Semiclass. Opt.*, 1(4):424–432, 1999.
- [124] Michel Gross and Serge Haroche. Superradiance: an essay on the theory of collective spontaneous emission. *Phys. Rep.*, 93(5):301–396, 1982.

- [125] Barry M. Garraway. The Dicke model in quantum optics: Dicke model revisited. *Phil. Trans. R. Soc. A*, 369(1939):1137–1155, 2011.
- [126] Paul A. M. Dirac. The quantum theory of the emission and absorption of radiation. *Proceedings of the Royal Society of London. Series A, Containing Papers of a Mathematical and Physical Character*, pages 243–265, 1927.
- [127] R. G. Brewer, R. G. DeVoe, and R. Kallenbach. Planar ion microtraps. *Physical Review A*, 46(11):R6781, 1992.
- [128] Michael Tavis and Frederick W. Cummings. Exact solution for an n -molecule–radiation-field Hamiltonian. *Phys. Rev.*, 170(2):379–384, June 1968.
- [129] L.-M. Duan and C. Monroe. Colloquium: Quantum networks with trapped ions. *Rev. Mod. Phys.*, 82(2):1209–1224, April 2010.
- [130] L.-M. Duan, M. D. Lukin, J. I. Cirac, and P. Zoller. Long-distance quantum communication with atomic ensembles and linear optics. *Nature*, 414:413–418, 2001.
- [131] Rafael A. de Oliveira, Milrian S. Mendes, Weliton S. Martins, Pablo L. Saldanha, José W. R. Tabosa, and Daniel Felinto. Single-photon superradiance in cold atoms. *Phys. Rev. A*, 90(2):023848, August 2014.
- [132] Isaac L. Chuang and M. A. Nielsen. Prescription for experimental determination of the dynamics of a quantum black box. *J. Mod. Opt.*, 44(11-12):2455–2467, 1997.
- [133] Miroslav Ježek, Jaromír Fiurášek, and Zdeněk Hradil. Quantum inference of states and processes. *Physical Review A*, 68(1):012305, 2003.
- [134] Marko Cetina, Alexei Bylinskii, Leon Karpa, Dorian Gangloff, Kristin M Beck, Yufei Ge, Matthias Scholz, Andrew T Grier, Isaac Chuang, and Vladan Vuletić. One-dimensional array of ion chains coupled to an optical cavity. *New J. Phys.*, 15(5):053001, 2013.
- [135] S. Filipp, A. F. van Loo, M. Baur, L. Steffen, and A. Wallraff. Preparation of subradiant states using local qubit control in circuit qed. *Phys. Rev. A*, 84(6):061805, December 2011.
- [136] Yuanwei Zhang, Lixian Yu, J-Q Liang, Gang Chen, Suotang Jia, and Franco Nori. Quantum phases in circuit qed with a superconducting qubit array. *Scientific reports*, 4, 2014.
- [137] Robert Raussendorf and Hans J. Briegel. A one-way quantum computer. *Phys. Rev. Lett.*, 86:5188–5191, May 2001.